FREE-SPACE CHARACTERIZATION OF CONDUCTOR-BACKED ABSORBING MATERIALS USING AN APERTURE SCREEN

By

Korede Oladimeji

A DISSERTATION

Submitted to
Michigan State University
in partial fulfillment of the requirements
for the degree of

Electrical and Computer Engineering – Doctor of Philosophy

2022

ABSTRACT

Absorbing materials are often adhered to conducting surfaces for the purpose of controlling the electromagnetic field scattered by objects. Many of these materials have both electric and magnetic properties, and these properties may degrade with time, thereby decreasing the effectiveness of the coatings. Because of this, it is important to accurately assess the health of the coatings by interrogating them with an electromagnetic wave and analyzing the interaction of the wave with the coating materials. Ideally, the permeability and permittivity of the coatings would be measured and compared to baseline values. Since these measurements must be done in the field, the materials cannot be removed from the underlying conducting surfaces.

One convenient way to measure the permittivity and permeability of coatings is to illuminate a coated surface using an antenna placed at a certain standoff distance from the coated object. Standoff techniques do not involve physical contact with the coatings and thus reduce the possibility of damaging the coating during the measurement process. Because both complex permeability and complex permittivity are desired, two sufficiently different measurements of the complex reflected field are required. Previous studies have shown that varying the polarization or incidence angle of the interrogating field does not provide enough variation on the reflected field for robust measurements of the material parameters. These studies have also shown that applying a material layer in front of the coating does not alter the information about the coating available from measurements of the reflected field, and is thus ineffective.

In the technique proposed here, one measurement is made by illuminating the coated surface with a plane wave and a second measurement is made by illuminating the coated surface with a conducting screen containing an aperture placed immediately on top. This approach has proven effective with a waveguide contact probe, and the purpose here is to assess its viability as a free-space technique. The specific case of a narrow rectangular aperture is emphasized due to its simplicity of analysis compared to other aperture shapes.

The constitutive parameters are extracted by comparing the measured reflected field in the presence of the aperture to the reflected field obtained from a numerical model that has been developed. The model is based on plane wave excitation of an infinite layered medium with the reflected field found by numerically solving a magnetic field integral equation. The numerical solution is validated by using a radiation problem with a line source placed in the aperture. Error analysis is used to compare the efficacy of the proposed aperture method to that of the two-thickness method (which, although effective, cannot be applied in the field). Calibration of the approach is also considered and measured results are described.

For Anna, Ella and the little one that's on the way.

ACKNOWLEDGMENTS

I would like to express my most sincere gratitude to Dr Rothwell for his support. I am thankful that he chose to continue on as my advisor through periods that were challenging in getting my work complete. I would also like to thank my committee members: Dr Frasch, Dr Chahal and Dr Shanker. They provided invaluable advice and showed great patience that I am truly grateful for. Also, thanks to Dr Pierre for planting the seed in my heart as an undergraduate student that led me to pursue a graduate degree.

My family provided constant encouragement and believed even in moments when I had doubt. Thank you Mom for your constant checking in. Thank you Temi, Bowo and Iyin for all the help proof-reading a document that was only slightly meaningful to you. Thanks for the uplifting phone calls as well.

Last but most certainly not least, thank you Anna for your perseverance through this process. I'm grateful for your understanding over the span of time when we had to focus on various aspects of this work. I couldn't not have done this without you. And thanks for always making us smile Ella.

TABLE OF CONTENTS

CHAPTER 1

Introduction

1.1 Motivation and Background

1.1.1 Material Characterization

The accurate determination of the constitutive parameters (ϵ and μ) of materials is of particularly great importance in various fields ranging from bioengineering to agriculture and medicine [1] [2] [3]. Material characterization involves the employment of appropriate measurement and extraction techniques to obtain the permittivity (ϵ) and permeability (μ) of materials of interest. Knowledge of the values of these parameters and changes in their properties provide valuable insight that is useful in informing design choices and monitoring process quality. This plays a major role in applications ranging from communication to microelectronics, manufacturing, and food processing, just to name a few. For instance, the degradation in performance of an antenna radome over time may be monitored based on changes in the permittivity of the radome material.

The problem considered here is that of the characterization of material coatings on the surface of aircraft. The very nature of this problem makes it necessary that whatever measurement approach is taken be a reflection-only approach. This is because transmission measurements are precluded since the materials in question are conductor-backed. Also, techniques that require access to different material thicknesses or displacements of the material relative to the conductor backing are impractical since the coatings are affixed to the aircraft surface and cannot be excised. What is desired is an *in situ* conductor-backed material characterization approach.

In this work, a free-space aperture characterization method is proposed. The proposed method is non-destructive, non-contact and does not require the availability of transmission measurements. Before delving into the details, some general background and current state of the art in material characterization techniques are briefly discussed.

1.1.2 Material Characterization Techniques

Material characterization is founded on the measurement of the response of a material in the presence of an applied electromagnetic field. The constitutive parameters of a sample material can be extracted upon considering two implications of the interaction between an electromagnetic field and the sample: (1) a robust and repeatable means of exposure may be realizable, and (2) an accurate and tractable mathematical model describing this mechanism can be developed where possible. Furthermore, there must be access to two distinct complex measurements since two parameters (ϵ and μ) are to be extracted. This is analogous to the solution of an equation with two variables: two independent equations are required in order to solve for them.

All materials characterization techniques employ a measurement compared against a mathematical model with the constitutive parameters obtained by obtaining agreement between measurements taken in the lab and the theoretical model. Important considerations are the complexity of the model and the feasibility of the material exposure method. Broadly speaking, the simpler the model and the more flexible the exposure method the better. As such, what is desired is a technique that combines a well-understood theoretical model with a suitable method for exposing the material sample to an interrogating electromagnetic field. Additionally, a strong response is desired as it may difficult to successfully extract the parameters otherwise.

Material characterization techniques can be broadly classified into the following approaches: (1) Guided-wave technqiues, (2) Resonant Cavity techniques, and (3) Free-space techniques. Some factors to be cognizant of when choosing which technique is appropriate for a particular application include: frequency range of interest, temperature, desired level of accuracy, MUT (Material-Under-Test) size restrictions and MUT form (solid, liquid or gas). Also of importance is whether a destructive or non-destructive measurement is required and whether contact can be made with the MUT. The choice of which technique to employ usually involves trade-offs between these.

1.1.2.1 Guided-Wave Techniques

Guided-wave techniques can be further classified into open waveguide, filled waveguide and waveguide probe techniques. In the case of open waveguide and filled waveguide techniques, sample excision and preparation is necessary to ensure that the MUT is ready to be "held." As such, neither of these methods are well suited for the problem being considered since they are not non-destructive.

Waveguide probe techniques, on the other hand, are accommodating to *in-situ* interrogation of the surface of materials [4] [5]. There is a need in the case of these techniques, however, for the MUT to be planar as the waveguide aperture must make proper contact with the surface of the material being interrogated. Hence, they are also not applicable to the problem here.

Filled guide techniques include coaxial, stripline and rectangular waveguide techniques [6] [7]. Coaxial waveguide techniques are applicable in scenarios where the materials can be fashioned into a coaxial shape. The constitutive parameters can be obtained by measuring S-parameter data from a network analyzer connected to the coaxial waveguide. The material properties can then be extracted from processed S-parameter data.

Rectangular waveguide techniques are best suited to applications where the MUT is solid and can be readily machined/fashioned into a rectangular shape to fit into a waveguide fixture. S-parameter measurements through the waveguide are obtained and the constitutive parameters are extracted by processing the S-parameter data with known algorithms [8] [9].

Rectangular waveguide techniques are not suitable for the problem being considered. This is because they require the excision of the MUT and an imposition of sample size restrictions. Additionally, reflection measurements and transmission measurements (which are unavailable for a conductor-backed material) are needed for implementing the widely used Nicolson-Ross-Weir algorithm. Work has been done to extend the waveguide technique to the characterization of conductor-backed materials using a two-iris method [10]. But the need to fashion the MUT sample into sizes that can be fitted within a waveguide appropriately

still remains.

Other guided-wave implementations include dual-ridged waveguides[11], stepped flange waveguides [12], and the triaxial applicator system [13]. These different implementations have advantages over the other approaches that arise such as their applicability to magnetic materials. However, in certain cases the corresponding mathematical models may become intractably complex.

1.1.2.2 Resonant Cavity Techniques

Resonant cavity methods usually boast great accuracy and support for high temperature measurements [14] [15]. However, they are very narrow-banded and require special sample preparation that may be difficult and costly [16]. They are usually applied in determining the permittivity and loss tangent of low-loss materials. The dielectric properties are determined by first taking a measurement of the resonant frequency and Q of an empty cavity. The same measurements are carried out with the material present and the constitutive parameters can be computed from the resulting shift in frequency, volume and Q-factor.

Resonant cavity techniques are by definition not non-destructive, are only applicable at discrete frequencies and also require special sample preparation. Therefore, they are not suitable for the conductor-backed measurement desired.

1.1.2.3 Free-space Techniques

Free-space techniques are applicable over a wide frequency range with practical MUT sample size constraints imposed at lower frequencies. They are also applicable to a wide range of materials and useful in cases where measurements at high temperatures are desirable [17]. A figure illustrating a free-space measurement system is shown in Figure 1.1. Reflection and/or transmission measurements are obtained from a measurement system with the MUT illuminated by a transmit antenna and received by another antenna. A focused beam system can be utilized to reduce the effects of diffraction and time gating can be employed to minimize the impact of multiple reflections.

In contrast to guided-wave and resonant cavity methods previously discussed, free-space

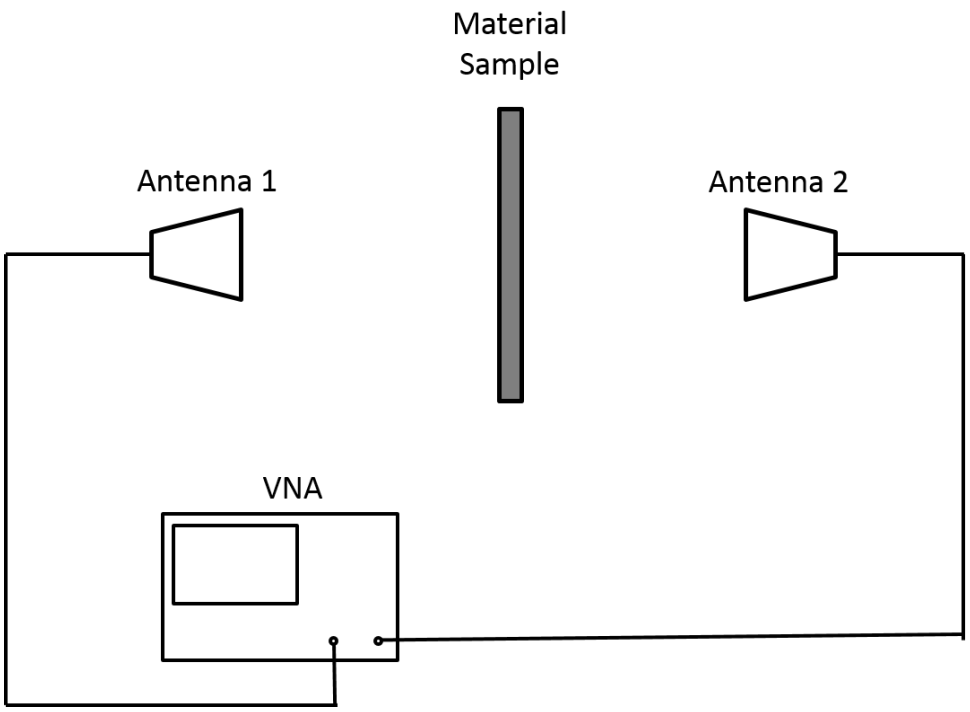

Figure 1.1: Free-Space Setup illustration.

techniques by definition can be implemented to satisfy the non-contact and non-destructive conditions desired for this application. Furthermore, the presence of a conductor backing narrows down the available options to reflection-only free-space methods since there is a lack of access to transmission measurements. As will be discussed in the next section, there are constraints and challenges that make the available reflection-only free-space methods inapplicable or troublesome to implement. Hence the need for the proposed technique.

1.2 Free-space Aperture Technique

This technique has the the advantage of being non-contact, robust and flexible. Before delving further into the details we first consider free-space techniques where only reflection measurements are available and/or obtainable.

These restrictions necessitate the development of a novel free-space approach which can be implemented *in-situ* in a non-destructive, non-contact manner. Additionally, the approach must have a mathematical model that is computationally tractable and realizable. A survey of the literature revealed the following reflection-only methods:the Two-Thickness

Method [18], the Air/Conductor Backed Method [19], the Layer-Shift Method [20], the Two-Polarization Method, and the Frequency Varying Method [21].

The two-thickness methods, as its name suggests, involves the carrying out/execution of two separate measurements with a conductor-backed MUT. The two measurements are taken with two samples of the same MUT having different thicknesses [19].

The air/conductor backed method similarly involves the performance of two measurements: the first with the MUT by itself without a conductor backing and the other with an identical sample of the MUT with a condcutor backing.

The layer-shift method involves one measurement of the MUT in a conductor-backed configuration with the conductor placed right behind and in contact with the sample, and a second measurement with conductor backing displaced a certain distance away from the surface of the sample.

These reflection-only techniques outlined are not well suited for the problem being considered for various reasons including this need for contact, inapplicability due to the curved nature of the aircraft surface, and lack of access to implement any displacement of the MUT. Also, the two-polarization method is highly sensitive to errors in the knowledge of aspect angle.

To recap, the technique proposed in this dissertation is a free-space technique that can be implemented in situations where transmission measurements are precluded given that the sample being considered is conductor backed and adhered to the conductor. The permittivity and permeability are determined by interrogating the target under test in two different distinct scenarios. One scenario involves the illumination of the material and measurement in the specular direction. The second scenario involves the illumination of the target with a metallic aperture adjacent to it and measurement of the reflection in a non-specular direction.

After two measurements are taken under the aforementioned scenarios, a root search method is employed to minimize the difference between the measurements and theoretical results so that the permittivity and permeability can be extracted.

1.3 Summary

The proposed material characterization technique is a reflection-only, in situ, nondestructive and non-contact approach. The upcoming chapter provides the theoretical framework for the free-space aperture technique.

The choice of this approach is motivated by the unique circumstance under which measurements are being taken for the problem being considered here. The approach satisfies the desire for a tractable mathematical model in conjunction with an appropriate physical method for holding the MUT and capturing the interaction with an electromagnetic field.

The upcoming chapters detail the proposed free-space aperture technique. Chapter 2 delves into the foundations of the formulation of the mathematical model. In Chapter 3, the numerical solution to the mathematical model is framed in terms of integral equations with the details of the solution provided. The extraction approach is detailed in Chapter 4 along with details on the implementation for the extraction of ϵ and μ. Chapter 5 describes the implementation of the optimization that is employed for determining the slot dimensions that lead to the optimal extraction parameters. The measurements carried out to validate the approach are discussed in Chapter 6. In Chapter 7, concluding remarks and future work are highlighted.

BIBLIOGRAPHY

[1] A. R. Von Hippel. *Dielectric Materials and Applications: Papers by Twenty-two Contributors*. Technology Press books in science and engineering. M.I.T. Press, 1954.

[2] H. E. Bussey. Measurement of rf properties of materials a survey. *Proceedings of the IEEE*, 55(6):1046–1053, 1967.

[3] L. F. Chen, C. K. Ong, C. P. Neo, V. V. Varadan, and V. K. Varadan. *Microwave Electronics: Measurement and Materials Characterization*. Wiley, 2004.

[4] M Hyde, J. W. Stewart, M. Havrilla, W. P. Baker, E. J. Rothwell, and D. Nyquist. Nondestructive electromagnetic material characterization using a dual waveguide probe: A full wave solution. *Radio Science*, 44, 2009.

[5] G. D. Dester, E. J. Rothwell, and M. J. Havrilla. An extrapolation method for improving waveguide probe material characterization accuracy. *IEEE Microwave and Wireless Components Letters*, 20(5):298–300, 2010.

[6] H. Yue, K. L. Virga, and J. L. Prince. Dielectric constant and loss tangent measurement using a stripline fixture. *IEEE transactions on components, packaging, and manufacturing technology. Part B, Advanced packaging*, 21(4):441–446, November 1998.

[7] W. Barry. A broad-band, automated, stripline technique for the simultaneous measurement of complex permittivity and permeability. *IEEE Transactions on Microwave Theory and Techniques*, 34(1):80–84, 1986.

[8] A. M. Nicolson and G. F. Ross. Measurement of the intrinsic properties of materials by time-domain techniques. *IEEE Transactions on Instrumentation and Measurement*, 19(4):377–382, 1970.

[9] W. B. Weir. Automatic measurement of complex dielectric constant and permeability at microwave frequencies. *Proceedings of the IEEE*, 62(1):33–36, 1974.

[10] G. D. Dester. *Electromagnetic Material Characterization of a Conductor-backed Material Using the Two Layer, Two Thickness, and Two Iris Waveguide Probe Methods: Error Analysis, Simulation, and Experimental Results*. Michigan State University. Department of Electrical Engineering, 2008.

[11] M. W. Hyde and M. J. Havrilla. Simple, broadband material characterization using dual-ridged waveguide to rectangular waveguide transitions. *IEEE Transactions on Electromagnetic Compatibility*, 56(1):239–242, 2014.

[12] J. P. Massman, M. J. Havrilla, K. W. Whites, and M. W. Hyde. A stepped flange waveguide technique for determining tapered r-card sheet impedance. In *2010 Asia-Pacific Microwave Conference*, pages 1769–1772, 2010.

[13] S. Karuppuswami, E. J. Rothwell, P. Chahal, and M. J. Havrilla. A triaxial applicator for the measurement of the electromagnetic properties of materials. *Sensors*, 18(2),

2018.

[14] J. Sheen. Microwave measurements of dielectric properties using a closed cylindrical cavity dielectric resonator. *IEEE Transactions on Dielectrics and Electrical Insulation*, 14(5):1139–1144, 2007.

[15] Keysight Application Note. *Split Post Dielectric Resonators for Dielectric Measurements*. Keysight Technologies, 2017.

[16] M. S. Venkatesh and V. Raghavan. An overview of dielectric properties measuring techniques. *Canadian Biosystems Engineering / Le Genie des biosystems au Canada*, 47:15–30, 01 2005.

[17] B. Clarke. *Measurement of the dielectric properties of materials at RF and microwave frequencies*, pages 409–458. 01 2007.

[18] J. Baker-Jarvis, E. J. Vanzura, and W. A. Kissick. Improved technique for determining complex permittivity with the transmission/reflection method. *IEEE Transactions on Microwave Theory and Techniques*, 38(8):1096–1103, 1990.

[19] R. Fenner, E. J. Rothwell, and L. Frasch. A comprehensive analysis of free-space and guided-wave techniques for extracting the permeability and permittivity of materials using reflection-only measurements. *Radio Science*, 47, 01 2012.

[20] A. A. Kalachev, I. V. Kukolev, S. M. Matitsin, L. N. Novogrudskiy, K. N. Rozanov, A. Sarychev, and A. V. Seleznev. The methods of investigation of complex dielectric permittivity of layer polymers containing conductive inclusions. *MRS Proceedings*, 214, 01 2011.

[21] S. Wang, M. Niu, and D. Xu. A frequency-varying method for simultaneous measurement of complex permittivity and permeability with an open-ended coaxial probe. *IEEE Transactions on Microwave Theory and Techniques*, 46(12):2145–2147, 1998.

CHAPTER 2

Theoretical Model

2.1 Introduction

This chapter details the theoretical work that was carried out to describe the proposed aperture technique. As mentioned in the previous chapter, a mathematical model is needed to describe the interaction between the interrogating electromagnetic field and the MUT. As a starting point, reflection from a coated conductor surface is considered. As will be shown, this is a problem for which closed form expressions relating the wave impedance to the permittivity and permeability can be derived. Following this, a theoretical model is developed for analysis of a slotted conductor above a conductor-backed slab.

2.2 Plane-wave reflection from a conductor-backed slab

Before the theory for the aperture problem is formulated, the field reflected by a plane wave incident on a conductor-backed material layer without an aperture screen is considered. Figure 2.1 shows an illustration of the general problem. A plane was is incident at an angle θ_0 on a conductor-backed material with thickness t having constitutive parameters ϵ and μ. The field can be polarized either in a parallel or perpendicular sense to the plane of incidence. Given this scenario, global reflection coefficients can be expressed as follows depending on the polarization [1]

The Fresnel (interfacial) reflection coefficients above are

$$\Gamma_{\perp} = \frac{Z_{\perp} - Z_{0\perp}}{Z_{\perp} + Z_{0\perp}} \tag{2.1}$$

and

$$\Gamma_{\parallel} = \frac{Z_{\parallel} - Z_{0\parallel}}{Z_{\parallel} + Z_{0\parallel}}, \tag{2.2}$$

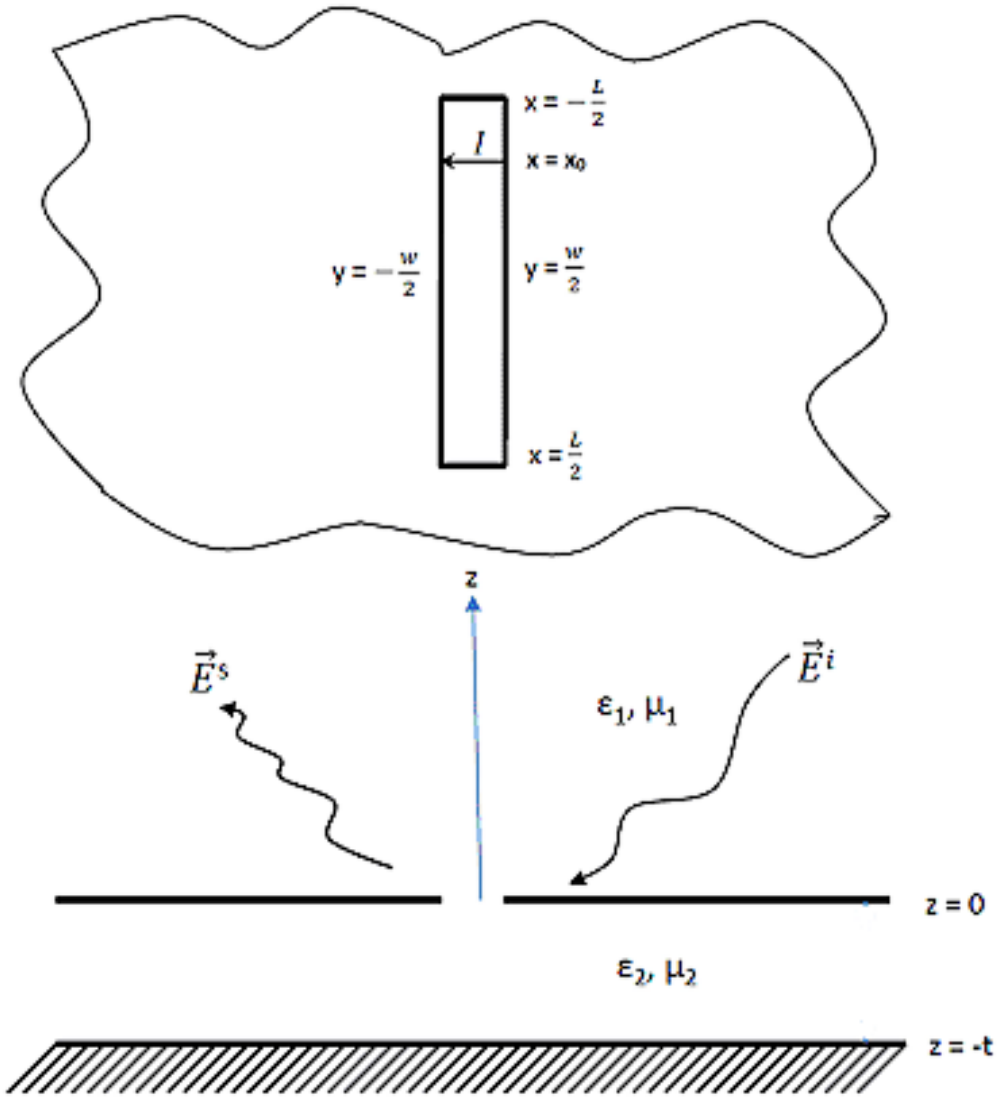

Figure 2.1: Conductor-backed material layer with slotted conductor directly on top.

where the various impedances are given by the expressions

$$Z_{\perp} = \frac{k\eta}{k_z}, \tag{2.3}$$

$$Z_{0\perp} = \frac{\eta_0}{\cos\theta_0}, \tag{2.4}$$

$$Z_{\parallel} = \frac{k_z\eta}{k}, \tag{2.5}$$

$$Z_{0\parallel} = \eta_0 \cos\theta_0 \tag{2.6}$$

and $k_z^2 = k^2 - k_0^2 \sin^2\theta_0$, $k^2 = \omega^2\epsilon\mu$, $k_0^2 = \omega^2\mu_0\epsilon_0$, $\eta^2 = \mu/\epsilon$, $\eta_0^2 = \mu_0/\epsilon_0$. The term P is the propagation factor for the wave traversing the material layer, and is given by $P = e^{-jk_z t}$.

It should be noted that the product of the permittivity and permeability appears in the wavenumber k, while the ratio of these quantities appears in the intrinsic impedance η. This behavior will be exploited later in the inversion algorithm.

2.3 MFIE analysis of a slotted conductor above a conductor backed slab

A theoretical model for the field scattered by a conductor-backed material with a slotted conductor placed above it is considered next. As mentioned earlier, in this case a closed form expression cannot be obtained. An integral equation is formulated for the field in the aperture and then the scattered field can be computed with the aperture field used as an equivalent source.

Consider a slot in a ground plane over a conductor-backed material region as shown in Figure 2.1. The material region (Region 2) has a permittivity ϵ_2, permeability μ_2 and thickness t while the half space above it (Region 1) has parameters ϵ_1 and μ_1.

The slot has a length L and a width w and is excited by a line current located at the point $x = x_o$ in the aperture or by an incident plane wave. The plane wave incidence case is of interest for the purpose of material characterization. The line current case is useful for validation since solutions obtained for the radiated field can be compared with results in the literature, as will be shown in the next section.

A magnetic field integral equation can be obtained by applying the boundary conditions on the electric and magnetic field across the slotted conductor. As illustrated in the figure, the slot is assumed to be "thin" with the assumption that $k_o w \ll 1$ and $w \ll L$. Given this assumption, the electric field within the slot may be approximated as $\vec{E}_s = \hat{y}E_s$. Let E_y^A be the aperture field immediately above the slot (i.e. in the free space region) and E_y^{PP} be the aperture field immediately below the slot (i.e. in the region bounded by the parallel conducting plates). In general, a magnetic current can be expressed as

$$\vec{K}_m = -\hat{n} \times \vec{E}. \tag{2.7}$$

From (2.7) magnetic currents can be expressed for the two regions as

$$\vec{K}_m^A = -\hat{z} \times \left(\hat{y}E_y^A\right) = \hat{x}E_y^A, \tag{2.8}$$

$$\vec{K}_m^{PP} = \hat{z} \times \left(\hat{y}E_y^{PP}\right) = -\hat{x}E_y^{PP}, \tag{2.9}$$

with $\vec{K}_m^A$ being the magnetic current in the half space immediately above the slotted conductor and $\vec{K}_m^{PP}$ that immediately below the slotted conductor in the material region.

Using the Hertz potential representation of the fields, the electric and magnetic fields can be written as $\vec{E} = -j\omega\mu\nabla\times\vec{\Pi}_m$ and $\vec{H} = k^2\vec{\Pi}_m + \nabla(\nabla\cdot\vec{\Pi}_m)$, respectively [2]. Furthermore, the corresponding wave equation for the Hertz potential is, as derived in the next section,

$$\left(\nabla^2 + k^2\right)\vec{\Pi}_m = -\frac{\vec{J}_m}{j\omega\mu}. \tag{2.10}$$

The solution for $\vec{\Pi}_m$ produced by the magnetic current $\vec{K}_m$ on the aperture surface is

$$\vec{\Pi}_m(\vec{r}) = \int_{S_A} \overleftrightarrow{G}(\vec{r}|\vec{r}\,') \cdot \frac{\vec{K}_m(\vec{r}\,')}{j\omega\mu} ds', \tag{2.11}$$

where $\overleftrightarrow{G}(\vec{r}|\vec{r}\,')$ is the dyadic Green's function for either the free-space or parallel plate regions.

The details of the Hertz potential formulation will be briefly considered in the following section.

2.3.1 Vector Potentials

If it is assumed that no electric charges are present ($\rho_e = 0$, where ρ_e is the electric volume charge density) then the divergence of the electric field is zero. This implies that the electric field is the curl of some vector quantity since the divergence of a curl is zero. Therefore, the electric displacement can be expressed as

$$\vec{D} = \nabla \times \vec{F} \tag{2.12}$$

where $\vec{F}$ is the electric vector potential. Substituting $\vec{D}$ from (2.12) into Ampere's law,

$$\nabla \times \vec{H} = j\omega\vec{D} \tag{2.13}$$

leads to

$$\nabla \times \vec{H} = j\omega\nabla \times \vec{F}, \tag{2.14}$$

which after rearranging becomes

$$\nabla \times \left(\vec{H} - j\omega\vec{F}\right) = 0. \tag{2.15}$$

Since the curl of the gradient of some quantity is zero, the quantity in parenthesis in (2.15) can be rewritten as

$$j\omega\vec{F} - \vec{H} = -\nabla\phi_m. \tag{2.16}$$

Next (2.12) can be substituted back into Faraday's law (assuming homogeneity),

$$\nabla \times \vec{D} = -j\omega\epsilon\vec{B} - \epsilon\vec{J}_m, \tag{2.17}$$

to give

$$\nabla \times \nabla \times \vec{F} = -j\omega\epsilon\vec{B} - \epsilon\vec{J}_m. \tag{2.18}$$

Furthermore, (2.16) can be rearranged so that

$$\vec{H} = j\omega\vec{F} + \nabla\phi_m. \tag{2.19}$$

Recalling that $\vec{B} = \mu\vec{H}$ gives

$$\nabla \times \nabla \times \vec{F} = -j\omega\epsilon\mu\left(j\omega\vec{F} + \nabla\phi_m\right) - \epsilon\vec{J}_m. \tag{2.20}$$

Utilizing (2.19) in the Magnetic Gauss' law,

$$\mu\nabla \cdot \vec{H} = \rho_m, \tag{2.21}$$

it can be seen that

$$\mu\nabla \cdot \left(\nabla\phi_m + j\omega\vec{F}\right) = \rho_m, \tag{2.22}$$

which can be rearranged to give

$$\nabla^2\phi_m + j\omega\nabla\cdot\vec{F} = \frac{1}{\mu}\rho_m. \tag{2.23}$$

Equation (2.20) can be expanded and simplified using the vector identity $\nabla\times\nabla\times\vec{F} = \nabla\nabla\cdot\vec{F} - \nabla^2\vec{F}$ yielding

$$\nabla\nabla\cdot\vec{F} - \nabla^2\vec{F} = -\epsilon\vec{J}_m + -j\omega\epsilon\mu\left(j\omega\vec{F} + \nabla\phi_m\right), \tag{2.24}$$

which upon expansion and rearrangement gives

$$-\nabla^2\vec{F} - k^2\vec{F} + \nabla\left(\nabla\cdot\vec{F} + j\omega\epsilon\mu\phi_m\right) = -\epsilon\vec{J}_m \tag{2.25}$$

where k, the wavenumber, is given by the relation $k^2 = \omega^2\epsilon\mu$. Employing the Lorentz gauge condition, the quantity in parenthesis in (2.25) is set to zero so that

$$\nabla\cdot\vec{F} = -j\omega\epsilon\mu\phi_m. \tag{2.26}$$

Therefore,

$$\phi_m = -\frac{\nabla\cdot\vec{F}}{j\omega\epsilon\mu}, \tag{2.27}$$

and (2.25) becomes

$$\nabla^2\vec{F} + k^2\vec{F} = \epsilon\vec{J}_m \tag{2.28}$$

which is a wave equation for the potential $\vec{F}$. Similarly, the wave equation for the scalar

potential can be obtained by substituting (2.26) into (2.23) resulting in the expression

$$\nabla^2\phi_m + j\omega\left(-j\omega\epsilon\mu\phi_m\right) = \frac{\rho_m}{\mu} \tag{2.29}$$

which can be rewritten as

$$\nabla^2\phi_m + k^2\phi_m = \frac{\rho_m}{\mu}. \tag{2.30}$$

From (2.12), the electric field can be expressed in terms of $\vec{F}$ as

$$\vec{E} = \frac{1}{\epsilon}\nabla \times \vec{F}. \tag{2.31}$$

The magnetic field can be similarly found by substituting (2.27) in (2.19) so that

$$\vec{H} = j\omega\vec{F} + \nabla\left(\frac{-\nabla\cdot\vec{F}}{j\omega\epsilon\mu}\right), \tag{2.32}$$

or

$$\vec{H} = j\omega\left(\vec{F} + \frac{\nabla\nabla\cdot\vec{F}}{k^2}\right). \tag{2.33}$$

Alternatively, $\vec{F}$ can be expressed in terms of the Hertzian vector potential $\vec{\Pi}_m$ as

$$\vec{F} = j\omega\mu\epsilon\vec{\Pi}_m. \tag{2.34}$$

Substituting (2.34) in (2.28) , the inhomogeneous Helmholtz equation for the Hertzian vector potential is found to be

$$\nabla^2\vec{\Pi}_m + k^2\vec{\Pi}_m = \frac{\vec{J}_m}{j\omega\mu}. \tag{2.35}$$

A solution to (2.35) can be obtained by convolving the Green's function with the source term on the right side of the equation.

Going back to considering the scattering problem, in the half-space region above the slotted conductor, the space-domain dyadic Green's function is given by [3]

$$\overleftrightarrow{G} = \overleftrightarrow{I}\, G. \tag{2.36}$$

In this region, the Hertz potential is therefore

$$\vec{\Pi}_m(\vec{r}) = \hat{x} \int\limits_{S_A} G(\vec{r}|\vec{r}\,') \frac{K_{mx}(\vec{r}\,')}{j\omega\mu_1} ds' \tag{2.37}$$

where G is the free-space Green's function [3],

$$G(\vec{r}, \vec{r}') = \frac{1}{(2\pi)^2} \int\limits_{-\infty}^{\infty} \int\limits_{-\infty}^{\infty} \frac{e^{-p|z-z'|}}{2p} e^{j\vec{k}\cdot(\vec{\rho}-\vec{\rho}\,')} dk_x dk_y. \tag{2.38}$$

In the region bounded by the parallel conducting plates,

$$\overleftrightarrow{G} = \overleftrightarrow{G}^{PP} = \hat{x} G_{xx}^{PP} \hat{x} + \hat{y} G_{yy}^{PP} \hat{y} + \hat{z} G_{zz}^{PP} \hat{z}, \tag{2.39}$$

where $\overleftrightarrow{G}^{PP}$ represents the parallel plate Green's function [4]. Geometrical considerations lead to the conclusion that $G_{xx}^{PP} = G_{yy}^{PP}$ since the underlying material is infinite in extent in the x and y directions. Because the slot is assumed to be narrow, $\vec{K}_m$ is assumed to be only x-directed, then

$$\vec{\Pi}_m(\vec{r}) = \hat{x} \int\limits_{S_A} G_{xx}^{PP}(\vec{r}|\vec{r}\,') \frac{K_{mx}(\vec{r}\,')}{j\omega\mu_2} ds' \tag{2.40}$$

and the magnetic field is given as

$$\vec{H} = k^2 \vec{\Pi}_m + \nabla(\nabla \cdot \vec{\Pi}_m). \tag{2.41}$$

The slot magnetic field is primarily x-directed, and

$$H_x = \left(k^2 + \frac{\partial^2}{\partial x^2}\right)\Pi_{mx}, \tag{2.42}$$

with the Hertzian potentials being

$$\Pi^A_{mx}(\vec{r}) = \int\limits_{S_A} G(\vec{r}\,|\vec{r}\,')\frac{K^A_{mx}(\vec{r}\,')}{j\omega\mu_1}ds', z > 0 \tag{2.43}$$

and

$$\Pi^{PP}_{mx}(\vec{r}) = \int\limits_{S_A} G^{PP}_{xx}(\vec{r}\,|\vec{r}\,')\frac{K^{PP}_{mx}(\vec{r}\,')}{j\omega\mu_2}ds', z > 0 \tag{2.44}$$

in the free-space and material regions respectively. Referring back to the expressions for the currents in equations (2.8) and (2.9), from (2.42) the magnetic fields can be expressed as

$$H^A_x = \left(k_1^2 + \frac{\partial^2}{\partial x^2}\right)\int\limits_{S_A} G(\vec{r}\,|\vec{r}\,')\frac{2E^A_y(\vec{r}\,')}{j\omega\mu_1}ds', z > 0 \tag{2.45}$$

and

$$H^{PP}_x = \left(k_2^2 + \frac{\partial^2}{\partial x^2}\right)\int\limits_{S_A} G^{PP}_{xx}(\vec{r}\,|\vec{r}\,')\frac{-E^{PP}_y(\vec{r}\,)}{j\omega\mu_2}ds', z < 0. \tag{2.46}$$

Invoking the boundary conditions at the interface, the tangential magnetic field is discon-

tinuous by a jump in the current so

$$\hat{z} \times (\vec{H}_1 - \vec{H}_2) = \vec{K}. \tag{2.47}$$

Substituting the values of the magnetic fields at the interface and the value of the surface current,

$$\hat{z} \times (\hat{x}H_x^A + \hat{x}H_z^i - \hat{x}H_x^{PP}) = -\hat{y}Ig(x - x_o) \tag{2.48}$$

and

$$H_x^A - H_z^{PP} = -H_x^i - Ig(x - x_o), \tag{2.49}$$

where $g(x)$ is a current distribution chosen subject to the condition

$$\int_{-\frac{L}{2}}^{\frac{L}{2}} g(x - x_0)dx = 1. \tag{2.50}$$

Also, given that the tangential electric field is continuous

$$E_y^A = E_y^{PP} = E_y. \tag{2.51}$$

Substituting (2.49) and (2.51) in (2.45) and (2.46) gives

$$\begin{aligned}\left(k_1^2 + \frac{\partial^2}{\partial x^2}\right) \int\limits_{S_A} G(\vec{r}\,|\vec{r}\,')\frac{2E_y(\vec{r}\,')}{j\omega\mu_o}ds' + \left(k_2^2 + \frac{\partial^2}{\partial x^2}\right) \int\limits_{S_A} G_{xx}^{PP}(\vec{r}\,|\vec{r}\,')\frac{E_y(\vec{r}\,')}{j\omega\mu}ds' \\ = -H_x^i - Ig(x - x_o), z > 0, \forall (x, y) \in S_A.\end{aligned} \tag{2.52}$$

This is an MFIE for the aperture field E_y.

2.3.2 Field Expansion in Terms of Slot Voltages

An alternate expression of (2.52) can be written in terms of the voltage across the slot. Remembering that the slot is narrow, the voltage across it exhibits only x-dependence and the electric field and voltage are related by

$$E_y(x,y) = V(x)f(y) \tag{2.53}$$

where

$$V(x) = -\int_{\frac{w}{2}}^{-\frac{w}{2}} E_y dy. \tag{2.54}$$

Consequently, (2.52) can be rewritten as

$$\begin{aligned}\left(k_1^2 + \frac{\partial^2}{\partial x^2}\right) \int_{x'=-\frac{L}{2}}^{\frac{L}{2}} \int_{y'=-\frac{w}{2}}^{\frac{w}{2}} \frac{G(x,y|x',y')}{j\omega\mu_1} 2V(x')f(y')dy'dx' + \\ \left(k_2^2 + \frac{\partial^2}{\partial x^2}\right) \int_{x'=-\frac{L}{2}}^{\frac{L}{2}} \int_{y'=-\frac{w}{2}}^{\frac{w}{2}} \frac{G_{xx}^{PP}(x,y|x',y')}{j\omega\mu_2} V(x')f(y')dy'dx' \\ = -H_x^i(x,y) - Ig(x-x_o).\end{aligned} \tag{2.55}$$

The electric field, Ey, can be substituted from (2.53) and (2.54) becomes

$$V(x) = V(x)\int_{-\frac{w}{2}}^{\frac{w}{2}} f(y)dy \tag{2.56}$$

which implies that the above integral of $f(y)$ is unity i.e.

$$\int_{-\frac{w}{2}}^{\frac{w}{2}} f(y)dy = 1. \tag{2.57}$$

In order to solve (2.55), a description of the magnetic current distribution is required. The function

$$f(y) = \frac{A}{\sqrt{1 - \left(\frac{y}{w/2}\right)^2}} \tag{2.58}$$

is chosen so as to satisfy the quasi-static edge singularities. Substuting (2.58) into (2.57),

$$2A \int_{0}^{\frac{w}{2}} \frac{dy}{\sqrt{1 - \left(\frac{y}{w/2}\right)^2}} = 1. \tag{2.59}$$

Setting $u = \frac{y}{w/2}$, (2.59) becomes

$$2A\frac{w}{2} \int_{0}^{1} \frac{du}{\sqrt{1 - u^2}} = 1 \tag{2.60}$$

and upon integration of (2.60) and some algebraic manipulation, it is found that

$$A = \frac{2}{\pi w}. \tag{2.61}$$

The value obtained for A in (2.61) be substituted into (2.59) and finally

$$f(y) = \frac{2}{\pi w\sqrt{1 - \left(\frac{y}{w/2}\right)^2}}. \tag{2.62}$$

The equation in (2.55) is multiplied by a weighting function $W(y)$ and integrated over y,

$$\begin{aligned}
&\left(k_1^2+\frac{\partial^2}{\partial x^2}\right)\int_{x'=-\frac{L}{2}}^{\frac{L}{2}}\int_{y'=-\frac{w}{2}}^{\frac{w}{2}}\int_{y=-\frac{w}{2}}^{\frac{w}{2}}\frac{G(x,y|x',y')}{j\omega\mu_1}2V(x')f(y')W(y)dy'dx'dy+\\
&\left(k_2^2+\frac{\partial^2}{\partial x^2}\right)\int_{x'=-\frac{L}{2}}^{\frac{L}{2}}\int_{y'=-\frac{w}{2}}^{\frac{w}{2}}\int_{y=-\frac{w}{2}}^{\frac{w}{2}}\frac{G_{xx}^{PP}(x,y|x',y')}{j\omega\mu_2}V(x')f(y')W(y)dy'dx'dy\\
&\qquad=-H_x^i(x,y)-Ig(x-x_o).
\end{aligned}\tag{2.63}$$

After matching the field at the center of the slot (by choosing $\omega(y)=\delta(y)$), the MFIE can be written as

$$\begin{aligned}
&\left(k_1^2+\frac{\partial^2}{\partial x^2}\right)\int_{-\frac{L}{2}}^{\frac{L}{2}}G_1(x,x')V(x')dx'+\left(k_2^2+\frac{\partial^2}{\partial x^2}\right)\int_{-\frac{L}{2}}^{\frac{L}{2}}G_2(x,x')V(x')dx'\\
&\qquad=-H(x)-I\delta(x-x_0),\quad -\frac{L}{2}\le x\le\frac{L}{2}
\end{aligned}\tag{2.64}$$

where

$$G_1(x,x')=\int_{-\frac{w}{2}}^{\frac{w}{2}}\frac{2G(x,y=0|x',y')}{j\omega\mu_1}f(y')dy',\tag{2.65}$$

$$G_2(x,x')=\int_{-\frac{w}{2}}^{\frac{w}{2}}\frac{G_{xx}^{PP}(x,y=0|x',y')}{j\omega\mu_2}f(y')dy',\tag{2.66}$$

and

$$H(x) = H_x^i(x, 0). \tag{2.67}$$

2.3.3 Alternative Form for Low-loss Materials

An alternate approach which is found to be more amenable to application with low-loss media is also employed to solve the problem.

Adding and subtracting the term $k_2^2 \int_{-\frac{L}{2}}^{\frac{L}{2}} G_1(x, x')V(x')dx'$, (2.64) can be rewritten as

$$\begin{aligned}
&\left(k_2^2 + \frac{\partial^2}{\partial x^2}\right) \int_{-\frac{L}{2}}^{\frac{L}{2}} \left[G_1\left(x, x'\right) + G_2\left(x, x'\right)\right] V(x')dx' \\
&= \left(k_2^2 - k_1^2\right) \int_{-\frac{L}{2}}^{\frac{L}{2}} G_1(x, x')V(x')dx' - H(x) - I\delta(x - x_0), \\
&\qquad -\frac{L}{2} \leq x \leq \frac{L}{2}
\end{aligned} \tag{2.68}$$

which takes the form

$$\left(k^2 + \frac{\partial^2}{\partial x^2}\right) F(x) = G(x), \tag{2.69}$$

which has a solution [1]

$$F(x) = \frac{1}{k} \int_{x_1}^{x} G(u) \sin k(x - u)du + C_1 \sin kx + C_2 \cos kx \tag{2.70}$$

where C_1 and C_2 are arbitrary constants and x_1 is arbitrary. Choosing $x_1 = \frac{-L}{2}$ leads to

a Hallen-type MFIE as follows

$$\begin{aligned}
&\int_{-\frac{L}{2}}^{\frac{L}{2}} \left[G_1(x,x') + G_2(x,x')\right] V(x')dx' \\
&-\left(\frac{k_2^2 - k_1^2}{k_2^2}\right) \int_{-\frac{L}{2}}^{x} \left[\int_{-\frac{L}{2}}^{\frac{L}{2}} G_1(u,x')V(x')dx'\right] \sin k_2(x-u)du \\
&= \frac{1}{k_2} \int_{-\frac{L}{2}}^{x} H(u) \sin k_2(x-u)du - C_1 \sin k_2 x - C_2 \cos k_2 x, \\
&-\frac{L}{2} \leq x \leq \frac{L}{2}.
\end{aligned} \tag{2.71}$$

Equations (2.64) and (2.71) fully describe the problem and numerical solutions will be presented in the next chapter.

2.4 Summary

The MFIE for the slot voltage has been derived in this chapter. In the next chapter the details of the solution of the MFIE using the Method of Moments are outlined both in the original case and for the Hallen alternative.

BIBLIOGRAPHY

[1] E. J. Rothwell and M. J. Cloud. *Electromagnetics*. CRC Press, 2018.

[2] E. A. Essex. Hertz vector potentials of electromagnetic theory. *American Journal of Physics*, 45(11):1099–1101, 1977.

[3] R. E. Collin. *Green's Functions*, pages 55–172. 1991.

[4] C. Tai and P. Rozenfeld. Different representations of dyadic green's functions for a rectangular cavity. *IEEE Transactions on Microwave Theory and Techniques*, 24(9):597–601, 1976.

CHAPTER 3

Numerical Solution to Integral Equations

3.1 Introduction

Now that the MFIE has been derived, what follows is: (a) the derivation of the numerical solution to the problem, and (b) validation of the solution obtained. The main concerns in the implementation of a problem solution are convenience in expressing the results and the management of computational expense. Additionally, close attention has to paid to numerical accuracy in the implementation. The approach utilized in the solution of the MFIE developed in the previous chapter is discussed in the sections that follow.

Two solution approaches are considered. The first approach is applicable to the problem in general but difficulties are encountered when it is employed with low-loss materials. This approach is therefore utilized when the MUT is lossy. A second approach, which is better suited to dealing with low-loss materials, is also developed and is employed when the slot is in free space or over a low-loss MUT above a conducting screen.

Finally, validation of solutions obtained are carried out to ensure accuracy before proceeding to the optimization of the slot geometry. Numerical accuracy is discussed briefly as this is important in obtaining an optimal slot design.

3.2 General MFIE Formulation (Version 1 MFIE)

An initial formulation is developed for the problem and presented in this section. The MFIE obtained in the previous chapter is considered and the two parts of it are examined separately.

Recall the MFIE

$$\left(\frac{\partial^2}{\partial x^2}+k_1^2\right)\int_{-\frac{L}{2}}^{\frac{L}{2}} G_1(x,x')V(x')dx' + \left(\frac{\partial^2}{\partial x^2}+k_2^2\right)\int_{-\frac{L}{2}}^{\frac{L}{2}} G_2(x,x')V(x')dx' \tag{3.1}$$
$$= -H_x^i(x,0) - I\delta(x-x_o),$$
$$-\frac{L}{2} \le x \le \frac{L}{2}.$$

The free-space Green's function is utilized in the region above the slot (free-space) whereas in the material region a parallel plate Green's function is employed, i.e.

$$G_1(x,x') = \int_{-\frac{w}{2}}^{\frac{w}{2}} \frac{2G\left(x,y=0|x',y'\right)}{j\omega\mu_1} f(y')dy', \tag{3.2}$$

$$G_2(x,x') = \int_{-\frac{w}{2}}^{\frac{w}{2}} \frac{G_{xx}^{PP}\left(x,y=0|x',y'\right)}{j\omega\mu_2} f(y')dy'. \tag{3.3}$$

The free-space Green's function is given by

$$G(x,y|x',y') = \frac{1}{(2\pi)^2}\iint_{-\infty}^{\infty} \frac{1}{2p_1} e^{j\vec{k}\cdot(\vec{\rho}-\vec{\rho}\,')} dk_x dk_y \tag{3.4}$$

where

$$\vec{k} = \hat{x}k_x + \hat{y}k_y, \tag{3.5}$$

$$p_1^2 = k_x^2 + k_y^2 - k_1^2, \tag{3.6}$$

and

$$\vec{\rho} = \hat{x}x + \hat{y}y = \hat{x}x. \tag{3.7}$$

The Green's function in the parallel plate region is

$$G_{xx}^{PP}(x, y|x', y') = \frac{1}{(2\pi)^2} \iint_{-\infty}^{\infty} \frac{1}{p_2} \left[1 + \frac{e^{-p_2 t}}{\sinh(p_2 t)}\right] e^{j\vec{k}\cdot(\vec{\rho}-\vec{\rho}\,')} dk_x dk_y \tag{3.8}$$

where

$$p_2^2 = k_x^2 + k_y^2 - k_2^2. \tag{3.9}$$

Complete derivations for these Green's functions are shown in Appendix 7.1.

Using the appropriate Green's functions from (3.4) and (3.8), G_1 and G_2 in (3.1) are expressed as

$$G_1(x, x') = \int_{-\frac{w}{2}}^{\frac{w}{2}} \frac{2}{j\omega\mu_1} \left(\frac{1}{(2\pi)^2} \iint_{-\infty}^{\infty} \frac{1}{2p_1} e^{j\vec{k}\cdot(\vec{\rho}-\vec{\rho}\,')} dk_x dk_y \right) f(y') dy' \tag{3.10}$$

and

$$G_2(x, x') = \int_{-\frac{w}{2}}^{\frac{w}{2}} \frac{1}{j\omega\mu_2} \left(\frac{1}{(2\pi)^2} \iint_{-\infty}^{\infty} \frac{1}{p_2} \left[1 + \frac{e^{-p_2 t}}{\sinh(p_2 t)}\right] e^{j\vec{k}\cdot(\vec{\rho}-\vec{\rho}\,')} dk_x dk_y \right) \times f(y') dy' \tag{3.11}$$

respectively. The portion from (3.11) in square brackets is rewritten by taking advantage of

the definition of the sinh function so that

$$1+\frac{e^{-p_2 t}}{\sinh(p_2 t)}=1+2\frac{e^{-p_2 t}}{e^{p_2 t}-e^{-p_2 t}} \tag{3.12}$$

leading to

$$1+\frac{e^{-p_2 t}}{\sinh(p_2 t)}=1+\frac{2}{e^{2p_2 t}-1}. \tag{3.13}$$

This alternative version will be used in expanding (3.11) later.

The expressions in (3.10) and (3.11) are rearranged so that they can be expressed as convenient integrals over dk_x and dk_y. Substituting $\vec{k}$ and $\vec{\rho}$ from (3.5) and (3.7) respectively into (3.10) gives

$$G_1(x,x')=\frac{1}{(2\pi)^2}\frac{2}{2j\omega\mu_1}\iint_{-\infty}^{\infty}\frac{1}{p_1}\left[\int_{-\frac{w}{2}}^{\frac{w}{2}} e^{jk_x x}e^{-jk_x x'}e^{-jk_y y'}f(y')dy'\right]dk_x dk_y. \tag{3.14}$$

Defining the following integral

$$Q(k_y)=\int_{-\frac{w}{2}}^{\frac{w}{2}} e^{-jk_y u}f(u)du, \tag{3.15}$$

allows (3.14) to be written as

$$G_1(x,x')=\frac{1}{(2\pi)^2}\frac{1}{j\omega\mu_1}\iint_{-\infty}^{\infty}\frac{e^{jk_x(x-x')}}{p_1}Q\left(k_y\right)dk_x dk_y. \tag{3.16}$$

Recalling that f is a distribution representing a magnetic current and is chosen to satisfy

the quasi-static edge singularities as done in (2.62), f can be substituted in Q resulting in

$$Q(k_y) = \frac{4}{\pi w} \int_0^{\frac{w}{2}} \frac{\cos(k_y u)}{\sqrt{1 - \left(\frac{u}{w/2}\right)^2}} du, \tag{3.17}$$

which after employing the substitution $x = u/(w/2)$ becomes

$$Q(k_y) = \frac{4}{\pi w} \frac{w}{2} \int_0^1 \frac{\cos\left(k_y \frac{w}{2} x\right)}{\sqrt{1 - x^2}} dx. \tag{3.18}$$

The integral in (3.18) can be evaluated using (3.753.2) of [1]

$$\int_0^1 \frac{\cos(ax)}{\sqrt{1 - x^2}} dx = \frac{\pi}{2} J_0(a), \tag{3.19}$$

so that

$$Q(k_y) = J_0\left(k_y \frac{w}{2}\right) \tag{3.20}$$

where J_0 is the Bessel function of the first kind and order zero. Therefore,

$$G_1(x, x') = \frac{1}{(2\pi)^2} \frac{1}{j\omega\mu_1} \iint_{-\infty}^{\infty} \frac{e^{jk_x(x-x')}}{p_1} J_0\left(k_y \frac{w}{2}\right) dk_x dk_y. \tag{3.21}$$

Substituting from (3.13) and similarly taking advantage of (3.20), (3.11) can be rewritten as

$$G_2(x, x') = \frac{1}{(2\pi)^2} \frac{1}{j\omega\mu_2} \iint_{-\infty}^{\infty} \frac{e^{jk_x(x-x')}}{p_2} \left[1 + \frac{2}{e^{2p_2 t} - 1}\right] J_0\left(k_y \frac{w}{2}\right) dk_x dk_y. \tag{3.22}$$

This makes it possible to express the functions G_1 and G_2 concisely as

$$G_{1,2}(x,x') = \iint_{-\infty}^{\infty} W_{1,2}(k_x,k_y)e^{jk_x(x-x')}dk_xdk_y \tag{3.23}$$

where

$$W_1 = \frac{1}{(2\pi)^2}\frac{1}{j\omega\mu_1 p_1}J_0\left(k_y\frac{w}{2}\right) \tag{3.24}$$

and

$$W_2 = \frac{1}{(2\pi)^2}\frac{1}{j\omega\mu_2 p_2}\left[1+\frac{2}{e^{2p_2t}-1}\right]J_0\left(k_y\frac{w}{2}\right). \tag{3.25}$$

After carrying out the derivatives with respect to x, the MFIE in (3.1) can be rewritten in the form

$$\begin{aligned}
&\iint_{-\infty}^{\infty} W_1(k_x,k_y)(k_1^2-k_x^2)\int_{-L/2}^{L/2} V(x')e^{jk_x(x-x')}dx'dk_xdk_y \;+\\
&\iint_{-\infty}^{\infty} W_2(k_x,k_y)(k_2^2-k_x^2)\int_{-L/2}^{L/2} V(x')e^{jk_x(x-x')}dx'dk_xdk_y\\
&\qquad = -H(x) - I\delta(x-x_0),\\
&\qquad -L/2 \le x \le L/2,
\end{aligned} \tag{3.26}$$

3.2.1 Method of Moments (MoM) Solution

The Galerkin method [2] is employed for solving the integral equation in (3.26) by choosing the same expansion and testing functions. The functions are chosen so that the integrals obtained can eventually be computed in closed form. The voltage is expanded in terms of piecewise sinusoidal functions. The voltage across the slot is expanded as a set of of piecewise

sinusoidal functions

$$V(x) = \sum_{n=-N}^{N} a_n f_n(x) \tag{3.27}$$

with the basis function given by

$$f_n(x) = f_0(x - n\Delta) \tag{3.28}$$

where

$$\Delta = \frac{L}{2N+2} \tag{3.29}$$

and

$$f_0(x) = \sin k_0(\Delta - |x|) = \begin{cases} \sin k_0 (\Delta + x) & -\Delta \le x \le 0 \\ \sin k_0 (\Delta - x) & 0 \le x \le \Delta \end{cases}. \tag{3.30}$$

The voltage expression from (3.27) is substituted into (3.26) to give

$$\begin{aligned} &\sum_{n=-N}^{N} a_n \iint_{-\infty}^{\infty} W_1(kx, ky)(k_1^2 - k_x^2) \int_{-L/2}^{L/2} f_n(x') e^{jk_x(x-x')} dx' dk_x dk_y \; + \\ &\sum_{n=-N}^{N} a_n \iint_{-\infty}^{\infty} W_2(kx, ky)(k_2^2 - k_x^2) \int_{-L/2}^{L/2} f_n(x') e^{jk_x(x-x')} dx' dk_x dk_y \\ &\qquad = -H(x) + I\delta(x - x_0), \\ &\qquad -L/2 \le x \le L/2. \end{aligned} \tag{3.31}$$

The expression in (3.31) is multiplied by $f_m(x)$ and integrated over dx which gives

$$\begin{aligned}\sum_{n=-N}^{N} a_n \iint_{-\infty}^{\infty} \left[\left(k_1^2 - k_x^2\right) W_1(k_x, k_y) + \left(k_2^2 - k_x^2\right) W_2(k_x, k_y)\right] \times \\ \int_{-\frac{L}{2}}^{\frac{L}{2}} f_n(x') e^{-jk_x x'} dx' \int_{-\frac{L}{2}}^{\frac{L}{2}} f_m(x) e^{jk_x x} dx dk_x dk_y \\ = b_m, \quad m = -N, -N+1, ..., N.\end{aligned} \tag{3.32}$$

where

$$b_m = -\int_{-\frac{L}{2}}^{\frac{L}{2}} f_m(x) H(x) dx - I \int_{-\frac{L}{2}}^{\frac{L}{2}} f_m(x) \delta(x - x_0) dx. \tag{3.33}$$

It will be now be shown that the result in (3.32) can be conveniently expressed as a system of linear equations. First, a new quantity T_n defined as

$$T_n = \int_{-\frac{L}{2}}^{\frac{L}{2}} f_n(x) e^{jk_x x} dx \tag{3.34}$$

is considered. Recalling the definition of $f_n(x)$ in (3.30), (3.34) can be expanded as

$$\begin{aligned}T_n = \int_{(n-1)\Delta}^{n\Delta} \sin k_0(x - [n-1]\Delta) e^{jk_x x} dx + \\ \int_{n\Delta}^{(n+1)\Delta} \sin k_0\left(-x + [n+1]\Delta\right) e^{jk_x x} dx.\end{aligned} \tag{3.35}$$

Substituting $u = (x - [n-1]\Delta)$ and $u = (-x + [n+1]\Delta)$ in the first and second portions

of the right side of (3.35), respectively, gives

$$T_n = \int_0^{\Delta} e^{jk_x u} e^{jk_x(n-1)\Delta} \sin k_0 u du + \int_0^{\Delta} e^{-jk_x u} e^{jk_x(n+1)\Delta} \sin k_0 u du. \tag{3.36}$$

Evaluating the integrals in (3.36) yields

$$\begin{aligned} T_n = e^{jk_x(n-1)\Delta} \frac{e^{jk_x u}}{k_0^2 - k_x^2} \left[jk_x \sin k_0 u - k_0 \cos k_0 u \right] \Big|_0^{\Delta} + \\ e^{jk_x u(n+1)\Delta} \frac{e^{-jk_x u}}{k_0^2 - k_x^2} \left[-jk_x \sin k_0 u - k_0 \cos k_0 u \right] \Big|_0^{\Delta}. \end{aligned} \tag{3.37}$$

Upon evaluation, (3.37) becomes

$$\begin{aligned} T_n = \frac{1}{k_0^2 - k_x^2} \Big\{ e^{jk_x n\Delta} \left[jk_x \sin k_0\Delta - k_0 \cos k_0\Delta \right] + e^{jk_x(n-1)\Delta} k_0 \\ + e^{jk_x n\Delta} \left[-jk_x \sin k_0\Delta - k_0 \cos k_0\Delta \right] + e^{jk_x(n+1)\Delta} k_0 \Big\}. \end{aligned} \tag{3.38}$$

Collecting terms and simplifying further,

$$T_n = \frac{1}{k_0^2 - k_x^2} e^{jk_x n\Delta} \Big(-2k_0 \cos k_0\Delta + 2k_0 \cos k_x\Delta \Big). \tag{3.39}$$

Therefore,

$$T_n = \int_{-\frac{L}{2}}^{\frac{L}{2}} f_n(x) e^{jk_x x} dx = 2 \frac{k_0}{k_0^2 - k_x^2} e^{jk_x n\Delta} \left(\cos k_x\Delta - \cos k_0\Delta \right). \tag{3.40}$$

By inspection, it is seen that

$$T_n^* = \int_{-\frac{L}{2}}^{\frac{L}{2}} f_n(x')e^{-jk_x x'}dx' = 2\frac{k_0}{k_0^2 - k_x^2}e^{-jk_x n\Delta}(\cos k_x\Delta - \cos k_0\Delta). \tag{3.41}$$

Substituting (3.40) and (3.41) into (3.32) gives

$$\begin{aligned}\sum_{n=-N}^{N} a_n \iint_{-\infty}^{\infty} &\left[\left(k_1^2 - k_x^2\right)W_1(k_x,k_y) + \left(k_2^2 - k_x^2\right)W_2(k_x,k_y)\right]\times \\ &\frac{4k_0^2 e^{-jk_x(m-n)\Delta}}{\left(k_0^2 - k_x^2\right)^2}\left(\cos k_x\Delta - \cos k_0\Delta\right)^2 dk_x dk_y \\ &= -\int_{-\frac{L}{2}}^{\frac{L}{2}} f_m(x)H(x)dx - I\int_{-\frac{L}{2}}^{\frac{L}{2}} f_m(x)\delta(x-x_0)dx, \\ &m = -N, -N+1, ..., N.\end{aligned} \tag{3.42}$$

Utilizing Euler's relation and taking advantage of the fact that the integrands are even, (3.42) can be written as

$$\begin{aligned}&\sum_{n=-N}^{N} a_n \iint_{0}^{\infty} W_1(k_x,k_y)S_{mn}(k_1,k_x)dk_x dk_y + \\ &\sum_{n=-N}^{N} a_n \iint_{0}^{\infty} W_2(k_x,k_y)S_{mn}(k_2,k_x)dk_x dk_y \\ &= b_m, \quad m = -N, -N+1, ..., N\end{aligned} \tag{3.43}$$

where

$$S_{mn}(k_i, k_x) = 16(k_i^2 - k_x^2)\frac{k_0^2}{(k_0^2 - k_x^2)^2}\left(\cos k_x\Delta - \cos k_0\Delta\right)^2 \cos k_x(m-n)\Delta, \quad i = 1, 2. \tag{3.44}$$

Finally, considering (3.43), the MFIE can be expressed as a matrix equation in the form

$$\sum_{n=-N}^{N} \left[A_{mn} + B_{mn}\right] a_n = b_m. \tag{3.45}$$

where

$$A_{mn} = \iint_0^\infty W_1(k_x, k_y) S_{mn}(k_1, k_x) dk_x dk_y, \tag{3.46}$$

$$B_{mn} = \iint_0^\infty W_2(k_x, k_y) S_{mn}(k_2, k_x) dk_x dk_y, \tag{3.47}$$

and

$$b_m = -\int_{-\frac{L}{2}}^{\frac{L}{2}} f_m(x) H(x) dx - I \int_{-\frac{L}{2}}^{\frac{L}{2}} f_m(x)\delta(x - x_0) dx. \tag{3.48}$$

3.2.2 Evaluation of Matrix Elements

This section details the calculation of the entries in the matrix equation in (3.45).

3.2.2.1 Evaluation of A_{mn}

Examining A_{mn} alone in more detail,

$$A_{mn} = \frac{4}{\pi^2}\frac{1}{j\omega\mu_1}\int_0^\infty F(k_1,k_x)S_{mn}(k_1,k_x)dk_x \tag{3.49}$$

where

$$F(k,k_x) = \int_0^\infty \frac{J_0(k_y\frac{w}{2})}{\sqrt{k_y^2+\beta^2}}dk_y, \quad \beta^2 = k_x^2 - k^2. \tag{3.50}$$

Using the relation (6.552.1) in [1]

$$\int_0^\infty J_0(xy)\frac{dx}{\sqrt{x^2+\beta^2}} = I_0\left(\frac{\beta y}{2}\right)K_0\left(\frac{\beta y}{2}\right), \tag{3.51}$$

(3.50) becomes

$$F(k,k_x) = I_0\left(\frac{w}{4}\sqrt{k_x^2-k^2}\right)K_0\left(\frac{w}{4}\sqrt{k_x^2-k^2}\right) \tag{3.52}$$

where I_0 and K_0 are the modified Bessel functions of the first and second kind respectively, and order zero. The integral to infinity over dk_x in (3.49) can be split into two pieces about a value K as follows:

$$\begin{aligned} A_{mn} &= \frac{4}{\pi^2}\frac{1}{j\omega\mu_1}\int_0^K F(k_1,k_x)S_{mn}(k_1,k_x)dk_x + \\ &\quad \frac{4}{\pi^2}\frac{1}{j\omega\mu_1}\int_K^\infty F(k_1,k_x)S_{mn}(k_1,k_x)dk_x \\ &= A_{mn}^1 + A_{mn}^2 \end{aligned} \tag{3.53}$$

This is useful because a value of K can be chosen such that A^1_{mn} can be computed directly in closed form. K is chosen such that $K > k_0$. The singularity at $k_x = k_0$ which occurs in A^1_{mn} is removable.

In order to compute A^2_{mn}, S_{mn} is considered in more detail. For the purpose of further simplification, the trigonometric portion of the expression in (3.44) is considered by itself as

$$\rho = (\cos k_x\Delta - \cos k_0\Delta)^2 \cos k_x(m-n)\Delta. \tag{3.54}$$

Expanding (3.54) leads to

$$\begin{aligned}\rho = \cos^2 k_x\Delta \cos k_x(m-n)\Delta - \cos k_0\Delta \cos k_x\Delta \cos k_x(m-n)\Delta \\ + \cos^2 k_0\Delta \cos k_x(m-n)\Delta\end{aligned} \tag{3.55}$$

Using the cosine square identity, (3.55) becomes

$$\begin{aligned}\rho = \left(\frac{1}{2} + \frac{1}{2}\cos 2k_x\Delta\right) \cos k_x(m-n)\Delta - 2\cos k_0\Delta \cos k_x\Delta \cos(m-n)\Delta \\ + \cos^2 k_0\Delta \cos k_x(m-n)\Delta.\end{aligned} \tag{3.56}$$

Rearranging (3.56) gives

$$\begin{aligned}\rho = \left(\frac{1}{2} + \cos^2 k_0\Delta\right) \cos k_x(m-n)\Delta + \frac{1}{2}\cos 2k_x\Delta \cos k_x(m-n)\Delta - \\ 2\cos k_0\Delta \cos k_x\Delta \cos k_x(m-n)\Delta.\end{aligned} \tag{3.57}$$

Finally, using the trigonometric identity

$$\cos A \cos B = \frac{1}{2}\left[\cos(A-B) + \cos(A+B)\right], \tag{3.58}$$

the expression in (3.57) can be rewritten as

$$\begin{aligned}\rho = &\left(\frac{1}{2} + \cos^2 k_0\Delta\right)\cos k_x(m-n)\Delta \\ &+ \frac{1}{4}\Big[\cos k_x(m-n-2)\Delta + \cos k_x(m-n+2)\Delta\Big] \\ &- \cos k_0\Delta\Big[\cos k_x(m-n-1)\Delta + \cos k_x(m-m+1)\Delta\Big].\end{aligned} \tag{3.59}$$

An integral

$$\Xi_l(k) = \int_K^\infty \frac{k_0^2(k^2-k_x^2)}{\left(k_0^2-k_x^2\right)^2} F(k,k_x)\cos k_x l\Delta dk_x \tag{3.60}$$

can be defined so that upon inserting ρ, and consequently the trigonometric portion of S_{mn} into (3.53), A_{mn}^2 becomes

$$\begin{aligned}A_{mn}^2 = &\frac{4}{\pi^2}\frac{1}{j\omega\mu_1}\left\{\left(\frac{1}{2} + \cos^2 k_0\Delta\right)\Xi_{m-n} + \right. \\ &\left.\frac{1}{4}\left(\Xi_{m-n-2} - \Xi_{m-n+2}\right) - \cos k_0\Delta\left(\Xi_{m-n-1} + \Xi_{m-n+1}\right)\right\}.\end{aligned} \tag{3.61}$$

It should be pointed out again that although there is a singularity at $k_x = k_0$, it is not encountered since $K > k_0$

For $l > 0$, the QDAWF routine is employed for evaluating the integral given the form

$$\int_a^\infty f(x)\cos(\omega x)dx. \tag{3.62}$$

QDAWF uses an adaptive scheme to integrate such Fourier integrals over a semi-infinite interval [3]. It carries out the integration over a number of subintervals and invokes an extrapolation procedure to estimate the integral [4]. However, for the case where $l = 0$, $\Xi_l(k)$ converges slowly since the cosine product is no longer present. An alternative expression of the integral that converges faster can be obtained by some mathematical manipulation.

Substituting in $l = 0$, (3.60) becomes

$$\Xi_0(k) = \int_K^{\infty} \frac{k_0^2(k^2 - k_x^2)}{\left(k_0^2 - k_x^2\right)^2} F(k, k_x) dk_x. \tag{3.63}$$

Furthermore, considering the case with a free-space overlay, $k = k_0$, and (3.63) can be rewritten as

$$\Xi_0(k_0) = \int_K^{\infty} \frac{k_0^2}{k_0^2 - k_x^2} F(k_0, k_x) dk_x. \tag{3.64}$$

The entire integrand above can be expressed as a function $f(k_x)$, so that (3.64) becomes

$$\Xi_0(k_0) = \int_K^{\infty} f(k_x) dk_x. \tag{3.65}$$

As k_x approaches infinity, the integrand above goes to zero since this is necessary for convergence. The approximation (9.7.5) in [5]

$$I_0(z)K_0(z) \sim \frac{1}{2z}\{1 + \frac{1}{8z^2} + ...\} \tag{3.66}$$

can be employed so that as k_x approaches infinity,

$$f(k_x) = \frac{k_0^2}{k_0^2 - k_x^2} I_0\left(\frac{w}{4}\sqrt{k_x^2 - k_0^2}\right) K_0\left(\frac{w}{4}\sqrt{k_x^2 - k_0^2}\right) \sim f^A(k_x) = \frac{k_0^2}{k_0^2 - k_x^2} \frac{1}{2\frac{w}{4}\sqrt{k_x^2 - k_0^2}}. \tag{3.67}$$

The large-argument asymptotic form of the integrand in (3.64) can thus be expressed as

$$f^A(k_x) = -\frac{k_0^2}{k_x^2 - k_0^2}\frac{1}{2\frac{w}{4}\sqrt{k_x^2 - k_0^2}} = -\frac{2}{w}k_0^2\frac{1}{\left(k_x^2 - k_0^2\right)^{3/2}}. \tag{3.68}$$

This implies that for large k_x, $f(k_x) \sim O(k_x^{-3})$.

The expression for Ξ_0 in (3.65) can be reconsidered and written in the form

$$\Xi_0(k_0) = \int_K^\infty \left[f(k_x) - f^A(k_x)\right] dk_x + \int_K^\infty f^A(k_x)dk_x. \tag{3.69}$$

This is advantageous because the integral of the difference in square brackets converges faster than the original integral of $f(k_x)$ since the integrand decays more rapidly with k_x. Additionally, the integral of $f^A(k_x)$ can be computed in closed form as follows

$$\int_K^\infty f^A(k_x)dk_x = -\frac{2}{w}k_0^2\int_K^\infty \frac{dk_x}{\left(k_x^2 - k_0^2\right)^{3/2}} \tag{3.70}$$

This integral is equal to

$$\int_K^\infty f^A(k_x)dk_x = -\frac{2}{w}k_0^2\left[-\frac{k_x}{k_0^2\sqrt{k_x^2 - k_0^2}}\right]\Bigg|_K^\infty = \frac{2}{w}\left[1 - \frac{K}{K^2 - k_0^2}\right]. \tag{3.71}$$

Finally, substituting $f(k_x)$ and $f^A(k_x)$ from (3.67) and (3.71) respectively into (3.69) gives

$$\begin{aligned} I(k) = \int_K^\infty \Bigg\{ &\left(\frac{-k_0^2}{\left(k_x^2 - k_0^2\right)}\right) I_0\left(\frac{w}{4}\sqrt{k_x^2 - k_0^2}\right) K_0\left(\frac{w}{4}\sqrt{k_x^2 - k_0^2}\right) + \\ &\frac{2}{w}k_0^2\frac{1}{\left(k_x^2 - k_0^2\right)^{3/2}}\Bigg\} dk_x + \frac{2}{w}\left[1 - \frac{K}{K^2 - k_0^2}\right]. \end{aligned} \tag{3.72}$$

3.2.2.2 Evaluation of B_{mn}

After substituting W_2 from (3.25) into (3.47), B_{mn} is given by

$$B_{mn} = \frac{1}{(2\pi)^2}\frac{1}{j\omega\mu_2}\iint_0^\infty \frac{J_0(k_y\frac{w}{2})}{p_2}\left[1+\frac{2}{e^{2p_2t}-1}\right]S_{mn}(k_2,k_x)dk_xdk_y, \tag{3.73}$$

which can be rewritten as

$$\begin{aligned} B_{mn} = &\frac{1}{4\pi^2}\frac{1}{j\omega\mu_2}\int_0^\infty F(k_2,k_x)S_{mn}(k_2,k_x)dk_x \\ &+\frac{1}{4\pi^2}\frac{1}{j\omega\mu_2}\int_0^\infty \bar{F}(k_2,k_x)S_{mn}(k_2,k_x)dk_x. \end{aligned} \tag{3.74}$$

Here $F(k,k_x)$ is given by (3.52) and

$$\bar{F}(k_2,k_x) = \int_0^\infty \frac{J_0(k_y\frac{w}{2})}{p_2}\frac{e^{-2p_2t}}{1-e^{-2p_2t}}dk_y \tag{3.75}$$

with

$$p_2 = \sqrt{k_x^2+k_y^2-k_2^2}, \qquad \Re\{p_2\} > 0. \tag{3.76}$$

The expression for B_{mn} can thus be considered in two parts,

$$B_{mn} = B_{mn}^1 + B_{mn}^2, \tag{3.77}$$

as done previously for A_{mn} in (3.53) with

$$B_{mn}^1 = \frac{1}{4\pi^2}\frac{1}{j\omega\mu_2}\iint_0^\infty \frac{J_0\left(k_y\frac{w}{2}\right)}{p_2}S_{mn}(k_2,k_x)dk_xdk_y \tag{3.78}$$

and

$$B_{mn}^2 = \frac{1}{4\pi^2}\frac{1}{j\omega\mu_2}\iint_0^\infty \frac{J_0\left(k_y\frac{w}{2}\right)}{p_2}\left[\frac{2e^{-2p_2t}}{1-e^{-2p_2t}}\right]S_{mn}(k_2,k_x)dk_xdk_y. \tag{3.79}$$

The portion of (3.79) in square brackets can be renamed Υ so that

$$\Upsilon = 2\frac{e^{-2p_2t}}{1-e^{-2p_2t}}. \tag{3.80}$$

Rearranging,

$$\Upsilon = 2e^{-2p_2t}\left[\frac{1}{1-e^{-2p_2t}}\right]. \tag{3.81}$$

The portion in brackets above can be written as a geometric series [6]

$$\Upsilon = 2e^{-2p_2t}\sum_{l=0}^{\infty} e^{-2lp_2t} \tag{3.82}$$

which can be rewritten as

$$\Upsilon = 2\sum_{l=1}^{\infty} e^{-2lp_2t}. \tag{3.83}$$

Substituting Υ in (3.79) leads to

$$B_{mn}^2 = \frac{1}{4\pi^2}\frac{1}{j\omega\mu_2}\sum_{l=1}^{\infty}\int_{k_x=0}^{\infty}\left\{\int_{k_y=0}^{\infty} 2\frac{J_0(k_y\frac{w}{2})}{p_2}e^{-2lp_2t}dk_y\right\}S_{mn}(k_2,k_x)dk_x. \tag{3.84}$$

Using

$$\int_0^\infty e^{-\alpha\sqrt{x^2+\beta^2}} J_\nu(\gamma x)\frac{dx}{\sqrt{\beta^2+x^2}} = I_{\frac{1}{2}\nu}\left(\frac{\beta}{2}\left[\sqrt{\alpha^2-\gamma^2}-\alpha\right]\right) \times K_{\frac{1}{2}\nu}\left(\frac{\beta}{2}\left[\sqrt{\alpha^2-\gamma^2}-\alpha\right]\right) \tag{3.85}$$

$$[\text{Re }\alpha > 0, \text{Re }\beta > 0, \gamma > 0, \text{Re }\nu > -1]$$

from (6.637.1) in [1], (3.84) can be rewritten as

$$B_{mn}^2 = \frac{1}{4\pi^2}\frac{1}{j\omega\mu_2}\sum_{l=1}^{\infty} 2 \int_{k_x=0}^{\infty} I_0\left(\frac{\sqrt{k_x^2-k_2^2}}{2}[\delta_l - 2lt]\right) \times K_0\left(\frac{\sqrt{k_x^2-k_2^2}}{2}[\delta_l - 2lt]\right) S_{mn}(k_2, k_x)dk_x \tag{3.86}$$

where

$$\delta_l = \sqrt{4l^2t^2 + \frac{w^2}{4}}. \tag{3.87}$$

Finally, a more concise way of expressing (3.86) is given by

$$B_{mn}^2 = \frac{1}{4\pi^2}\frac{1}{j\omega\mu_2}\sum_{l=1}^{\infty} 2 \int_{k_x=0}^{\infty} F_l(k_2, k_x) S_{mn}(k_2, k_x)dk_x. \tag{3.88}$$

where

$$F_l(k, k_x) = I_0\left(\frac{\sqrt{k_x^2-k^2}}{2}[\delta_l - 2lt]\right) K_0\left(\frac{\sqrt{k_x^2-k^2}}{2}[\delta_l - 2lt]\right). \tag{3.89}$$

Thus, B_{mn} can be expressed as

$$B_{mn} = \frac{1}{4\pi^2}\frac{1}{j\omega\mu_2}\sum_{l=0}^{\infty}\epsilon_l \int_{k_x=0}^{\infty} F_l(k_2,k_x)S_{mn}(k_2,k_x)dk_x, \tag{3.90}$$

where $\epsilon_l = 1$ for $l = 0$ and $\epsilon_l = 2$ for $l > 0$. It should be noted that in the case where k_2 is complex S_{mn} has no singularity. On the other hand, when k_2 is real, B_{mn} is computed in the same manner as A_{mn}.

3.2.3 Evaluation of right-hand side elements

The computation of the right-hand side in equation (3.45) is examined in more detail in the sections that follow.

3.2.3.1 Plane-wave Excitation

Considering the case of plane-wave illumination, b_m from (3.45) can be computed in closed form. It is assumed that the plane wave incident on the slot is y-polarized with a propagation vector in the $x-z$ plane. This assumption is made since the incident field couples well into the slot direction in this case. For a y-polarized plane wave incident on the surface of the slot, as shown in Figure 3.1, the incident wave vector and incident electric field can be expressed as

$$\vec{k}^i = -k_0\hat{x}\sin\theta_0 - k_0\hat{z}\cos\theta_0 \tag{3.91}$$

and

$$\vec{E}^i = E_0\hat{y}e^{jk_0x\sin\theta_0}e^{jk_0z\cos\theta_0} \tag{3.92}$$

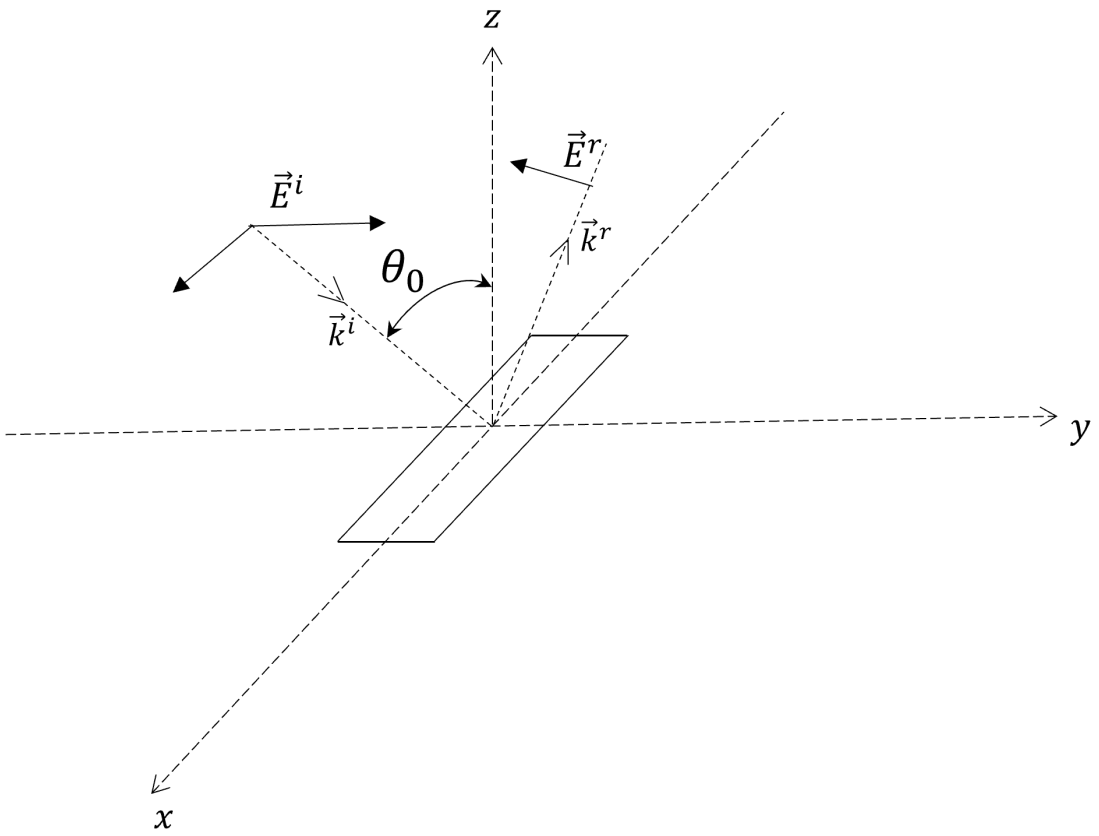

Figure 3.1: Figure showing y-polarized plane-wave excitation.

respectively where θ_0 is the incident angle. Thus the incident magnetic field which is given by

$$\vec{H}^i = \frac{\vec{k}^i \times \vec{E}^i}{\eta_0} \tag{3.93}$$

is

$$\begin{aligned} \vec{H}^i = -\hat{z}\frac{E_0}{\eta_0} e^{jk_0 x \sin\theta_0} e^{jk_0 z \cos\theta_0} \sin\theta_0 + \\ \hat{x}\frac{E_0}{\eta_0} e^{jk_0 x \sin\theta_0} e^{jk_0 z \cos\theta_0} \cos\theta_0. \end{aligned} \tag{3.94}$$

Similarly, given that $\vec{k}^r$ is

$$\vec{k}^r = -k_0\hat{x}\sin\theta_0 + k_0\hat{z}\cos\theta_0, \tag{3.95}$$

the reflected electric field is

$$\vec{E}^r = -E_0\hat{y}e^{jk_0x\sin\theta_0}e^{-jk_0z\cos\theta_0} \tag{3.96}$$

and the reflected magnetic field is

$$\vec{H}^r = \frac{\vec{k}^r \times \vec{E}^r}{\eta_0}. \tag{3.97}$$

Substituting (3.96) into (3.97) leads to

$$\begin{aligned}\vec{H}^r = {} & \hat{z}\frac{E_0}{\eta_0}e^{jk_0x\sin\theta_0}e^{-jk_0z\cos\theta_0}\sin\theta_0 \\ & +\hat{x}\frac{E_0}{\eta_0}e^{jk_0x\sin\theta_0}e^{-jk_0z\cos\theta_0}\cos\theta_0.\end{aligned} \tag{3.98}$$

The total excitation field which is a superposition of the incident and reflected fields is

$$\begin{aligned}\vec{H}^i + \vec{H}^r = {} & -\hat{z}2j\frac{E_0}{\eta_0}e^{jk_0x\sin\theta_0}\sin\theta_0\sin\left(k_0z\cos\theta_0\right) \\ & +\hat{x}2\frac{E_0}{\eta_0}e^{jk_0x\sin\theta_0}\cos\theta_0\cos\left(k_0z\cos\theta_0\right).\end{aligned} \tag{3.99}$$

The total field in the plane of the aperture (z = 0) becomes

$$\vec{H}^i + \vec{H}^r = 2\hat{x}\frac{E_0}{\eta_0}e^{jk_0x\sin\theta_0}\cos\theta_0. \tag{3.100}$$

In the case of normal incidence ($\theta_0 = 0$),

$$\vec{H}^i + \vec{H}^r = 2\hat{x}\frac{E_0}{\eta_0}. \tag{3.101}$$

Since $L = \Delta(2m+2)$ from (3.29), (3.48) can be rewritten so that

$$b_m = -\int_{(m-1)\Delta}^{(m+1)\Delta} H(x) f_0(x - m\Delta) dx. \tag{3.102}$$

Here, H is given by (3.100) and f_0 by (3.30). Substituting gives

$$\begin{aligned} b_m = &-\int_{(m-1)\Delta}^{m\Delta} 2\frac{E_0}{\eta_0}\cos\theta_0 e^{jk_0 x\sin\theta_0}\sin k_0(\Delta + x - m\Delta)dx \\ &-\int_{m\Delta}^{(m+1)\Delta} 2\frac{E_0}{\eta_0}\cos\theta_0 e^{jk_0 x\sin\theta_0}\sin k_0(\Delta - x + m\Delta)dx. \end{aligned} \tag{3.103}$$

If u is chosen as $u = x - (m-1)\Delta$ and $u = (m+1)\Delta - x$ for the first and second integrals in (3.103), respectively, then

$$\begin{aligned} b_m = &-2\frac{E_0}{\eta_0}\cos\theta_0 \int_0^{\Delta} e^{jk_0 u\sin\theta_0} e^{jk_0(m-1)\Delta\sin\theta_0}\sin k_0 u du \\ &-2\frac{E_0}{\eta_0}\cos\theta_0 \int_0^{\Delta} e^{-jk_0 u\sin\theta_0} e^{jk_0(m+1)\Delta\sin\theta_0}\sin k_0 u du \end{aligned} . \tag{3.104}$$

An alternative expression

$$\begin{aligned} b_m = &-2\frac{E_0}{\eta_0}\cos\theta_0 e^{jk_0 m\Delta\sin\theta_0}\times \\ &\int_0^{\Delta}\left[e^{jk_0 u\sin\theta_0} e^{-jk_0\Delta\sin\theta_0} + e^{-jk_0 u\sin\theta_0} e^{jk_0\Delta\sin\theta_0}\right]\sin k_0 u \end{aligned} \tag{3.105}$$

is obtained by pulling out the terms that have no dependence on the integration variable.

This can then be rewritten as

$$b_m = -2\frac{E_0}{\eta_0}\cos\theta_0 e^{jk_0 m\Delta\sin\theta_0}\times \int_0^{\Delta}\left[e^{jk_0(u-\Delta)\sin\theta_0} + e^{-jk_0(u-\Delta)\sin\theta_0}\right]\sin k_0 u du \tag{3.106}$$

which, after invoking Euler's relation, gives

$$b_m = -2\frac{E_0}{\eta_0}\cos\theta_0 e^{jk_0 m\Delta\sin\theta_0}\left(2\int_0^{\Delta}\cos\left[k_0(u-\Delta)\sin\theta_0\right]\sin k_0 u du\right). \tag{3.107}$$

After integration, (3.107) becomes

$$b_m = -4\frac{E_0}{\eta_0}\cos\theta_0 e^{jk_0 m\Delta\sin\theta_0}\times \left[\frac{\cos\left[k_0(u-\Delta)\sin\theta_0 - k_0 u\right]}{2\left[k_0\sin\theta_0 - k_0\right]} - \frac{\cos\left[k_0(u-\Delta)\sin\theta_0 + k_0 u\right]}{2\left[k_0\sin\theta_0 + k_0\right]}\right]\Bigg|_0^{\Delta} \tag{3.108}$$

which reduces to

$$b_m = -2\frac{E_0}{\eta_0 k_0}\cos\theta_0 e^{jk_0 m\Delta\sin\theta_0}\times \left[\frac{\cos[k_0\Delta]}{\sin\theta_0 - 1} - \frac{\cos[k_0\Delta]}{\sin\theta_0 + 1} - \frac{\cos[k_0\Delta\sin\theta_0]}{\sin\theta_0 - 1} + \frac{\cos[k_0\Delta\sin\theta_0]}{\sin\theta_0 + 1}\right] \tag{3.109}$$

after evaluation. Pulling like terms together (3.109) can be rewritten as

$$b_m = -2\frac{E_0}{\eta_0 k_0}\cos\theta_0 e^{jk_0 m\Delta\sin\theta_0}\times \left[\frac{2}{\sin^2\theta_0 - 1}\cos[k_0\Delta] - \frac{2}{\sin^2\theta_0 - 1}\cos[k_0\Delta\sin\theta_0]\right] \tag{3.110}$$

and finally

$$b_m = -4\frac{E_0}{\eta_0 k_0}\frac{1}{\cos\theta_0}e^{jk_0 m\Delta\sin\theta_0}[\cos(k_0\Delta\sin\theta_0) - \cos(k_0\Delta)]. \tag{3.111}$$

For the case of normal incidence ($\theta_0 = 0$)

$$b_m = -4\frac{E_0}{\eta_0 k_0}[1 - \cos(k_0\Delta)] \tag{3.112}$$

3.2.3.2 Line-current Excitation

It is necessary to examine the case of excitation with a line current as the resulting antenna problem is important for validation of the numerical solution. This will be shown in more detail later in the chapter. Considering the case of a line excitation within the slot, b_m can be expressed as

$$b_m = -\frac{1}{k_2}\int_{-\frac{L}{2}}^{x_m} H(u)\sin k_2(x_m - u)du \tag{3.113}$$

with $H(x)$ defined as

$$H(x) = H^i(x,0) + Ii(x,0). \tag{3.114}$$

Since $H^i(x,0) = 0$ and $i(x,0) = \delta(x - x_0)$,

$$b_m = -\frac{I}{k_0}\int_{-\frac{L}{2}}^{x_m} \delta(u - x_0)\sin k_x(x_m - u)du. \tag{3.115}$$

Evaluating (3.115) which leads to

$$b_m = \begin{cases} 0 & x_m < x_0 \\ -\frac{I}{k_2}\sin(k_2 x_m - x_0) & x_m > x_0 \end{cases}. \tag{3.116}$$

For a center-fed slot, $x_0 = 0$ and therefore

$$b_m = \begin{cases} 0 & x_m < 0 \\ -\frac{I}{k_2}\sin(k_2 x_m) & x_m > 0 \end{cases}. \tag{3.117}$$

3.2.4 Scattered Field Calculation

3.2.4.1 Using Sommerfeld Integral Green's function

The scattered field can be calculated using the Sommerfeld Integral Green's function. The electric field can be described as [7]

$$\vec{E} = -j\omega\mu\nabla \times \vec{\Pi}_m \tag{3.118}$$

where

$$\vec{\Pi}_m(\vec{r}) = \int\limits_{S_A} G(\vec{r}|\vec{r}\,') \frac{\vec{K}_m(\vec{r}\,')}{j\omega\mu} ds' \tag{3.119}$$

is the magnetic Hertzian potential. Here $\vec{K}_m$, the magnetic current across the slot, is

$$\vec{K}_m(\vec{r}) = \hat{x}2E_y(x,y) = \hat{x}2V(x)f(y) \tag{3.120}$$

and

$$G(\vec{r},\vec{r}\,') = \frac{1}{(2\pi)^2} \iint\limits_{-\infty}^{\infty} \frac{e^{-pz}}{2p} e^{j\vec{k}\cdot(\vec{\rho}-\vec{\rho}\,')} dk_x dk_y \tag{3.121}$$

where

$$\vec{k} = \hat{x}k_x + \hat{y}k_y \tag{3.122}$$

and

$$p^2 = k_x^2 + k_y^2 - k_0^2. \tag{3.123}$$

The y and z components of $\vec{E}$ are

$$E_y = -j\omega\mu\frac{\partial \Pi_{my}}{\partial z} \tag{3.124}$$

and

$$E_z = j\omega\mu\frac{\partial \Pi_{my}}{\partial y} \tag{3.125}$$

respectively. Therefore,

$$E_y = \int\limits_{S_A} 2V(x')f(y')\frac{1}{(2\pi)^2}\iint\limits_{-\infty}^{\infty}\frac{e^{-pz}}{2}e^{j\vec{k}\cdot(\vec{\rho}-\vec{\rho}\,')}dk_x dk_y dx' dy' \tag{3.126}$$

which can be rewritten as

$$\begin{aligned} E_y = \frac{1}{(2\pi)^2}\iint\limits_{-\infty}^{\infty}&\left[\int\limits_{y'=-\frac{w}{2}}^{\frac{w}{2}} f(y')e^{-jk_y y'}dy'\right] \\ \times&\left[\int\limits_{x'=-\frac{L}{2}}^{\frac{L}{2}} V(x')e^{-jk_x x'}dx'\right]e^{jk_x x}e^{k_y y}e^{-pz}dk_x dk_y. \end{aligned} \tag{3.127}$$

Considering the integral over x' in (3.127) separately, a new quantity

$$I = \int_{-\frac{L}{2}}^{\frac{L}{2}} V(x')e^{-jk_x x'}dx' \tag{3.128}$$

can be defined. As done earlier in (3.27) – (3.30), V can be represented by a linear combination of piecewise sinusoids so that (3.128) becomes

$$\begin{aligned} I = &\sum_{n=-N}^{N} a_n e^{-jk_x(n-1)\Delta} \int_0^{\Delta} \sin k_0 u e^{-jk_x u}du + \\ &\sum_{n=-N}^{N} a_n e^{-jk_x(n+1)\Delta} \int_0^{\Delta} \sin k_0 u e^{+jk_x u}du. \end{aligned} \tag{3.129}$$

After evaluating the integrals in (3.129),

$$\begin{aligned} I = &\sum_{n=-N}^{N} a_n \frac{e^{-jk_x n\Delta}}{k_0^2 - k_x^2} \times \\ &\Big[-jk_x \sin k_0\Delta - k_0 \cos k_0\Delta + k_0 e^{jk_x\Delta} \\ &+ jk_x \sin k_0\Delta - k_0 \cos k_0\Delta] + k_0 e^{-jk_x\Delta}\Big]. \end{aligned} \tag{3.130}$$

The integral over y' in (3.127), which has been encountered earlier in (3.15) is simply

$$\int_{-\frac{w}{2}}^{\frac{w}{2}} f(y')e^{-jk_y y'}dk_y = J_0\left(k_y \frac{w}{2}\right). \tag{3.131}$$

Substituting (3.130) and (3.131) into (3.127) yields

$$E_y = \frac{2k_0}{(2\pi)^2} \sum_{n=-N}^{\infty} a_n \iint_{-\infty}^{\infty} \frac{e^{-jk_x n\Delta}}{k_0^2 - k_x^2} \left[\cos k_x\Delta - \cos k_0\Delta\right] \times J_0\left(k_y \frac{w}{2}\right) e^{jk_x x} e^{jk_y y} e^{-pz} dk_x dk_y \tag{3.132}$$

which can be alternatively expressed in the form

$$E_y = \frac{2k_0}{\pi^2} \sum_{n=-N}^{N} a_n \int_{k_x=0}^{\infty} F(k_x) S_n(k_x) dk_x \tag{3.133}$$

where

$$F(k_x) = \int_{k_y=0}^{\infty} J_0\left(k_y \frac{w}{2}\right) \cos k_y y e^{z\sqrt{k_x^2 + k_y^2 - k_0^2}} dk_y \tag{3.134}$$

and

$$S_n(k_x) = \frac{\cos k_x\Delta - \cos k_0\Delta}{k_0^2 - k_x^2} \cos k_x(x - n\Delta). \tag{3.135}$$

Considering at first a case where $k_x < k_0$ with $\gamma^2 = k_0^2 - k_x^2 > 0$,

$$F(k_x) = \int_0^{\gamma} J_0\left(k_y \frac{w}{2}\right) \cos k_y y e^{-jz\sqrt{\gamma^2 - k_y^2}} dk_y + \int_{\gamma}^{\infty} J_0\left(k_y \frac{w}{2}\right) \cos k_y y e^{-z\sqrt{k_y^2 - \gamma^2}} dk_y. \tag{3.136}$$

The split in the integral is implemented to ensure the square root of a positive number is considered over each integration region. On the other hand, if $k_x > k_0$, again letting

$\gamma^2 = k_x^2 - k_0^2$

$$F(k_x) = \int_0^{\infty} J_0\left(k_y \frac{w}{2}\right) \cos k_y y e^{-z\sqrt{k_y^2+\gamma^2}}\, dk_y \tag{3.137}$$

Invoking Euler's relation, (3.136) can be expanded to give

$$\begin{aligned} F(k_x) = &\int_0^{\gamma} J_0\left(k_y \frac{w}{2}\right) \cos k_y y \cos\left(-jz\sqrt{\gamma^2 - k_y^2}\right) dk_y \\ &-j\int_0^{\gamma} J_0\left(k_y \frac{w}{2}\right) \cos k_y y \sin\left(-jz\sqrt{\gamma^2 - k_y^2}\right) dk_y \\ &+\int_{\gamma}^{\infty} J_0\left(k_y \frac{w}{2}\right) \cos k_y y e^{-z\sqrt{k_y^2-\gamma^2}}\, dk_y. \end{aligned} \tag{3.138}$$

An expression for E_y can finally be obtained by substituting (3.137) and (3.138) into (3.133) so that

$$
\begin{aligned}
E_y = \frac{2k_0}{\pi^2} \sum_{n=-N}^{N} a_n \times \\
\Bigg\{ \int_{k_x=0}^{k_0} \left[\int_{k_y=0}^{\sqrt{k_0^2-k_x^2}} J_0\left(k_y \frac{w}{2}\right) \cos\left(k_y y\right) \cos\left(z\sqrt{k_0^2-k_x^2-k_y^2}\right) dk_y \right] S_n(k_x) dk_x \\
- j \int_{k_x=0}^{k_0} \left[\int_{k_y=0}^{\sqrt{k_0-k_x^2}} J_0\left(k_y \frac{w}{2}\right) \cos\left(k_y y\right) \sin\left(z\sqrt{k_0^2-k_x^2-k_y^2}\right) dk_y \right] S_n(k_x) dk_x \\
+ \int_{k_x=0}^{k_0} \left[\int_{k_y=\sqrt{k_0^2-k_x^2}}^{\infty} J_0\left(k_y \frac{w}{2}\right) \cos\left(k_y y\right) e^{-\left(z\sqrt{k_y^2+k_x^2-k_0^2}\right)} dk_y \right] S_n(k_x) dk_x \\
+ \int_{k_x=k_0}^{\infty} \left[\int_{k_y=0}^{\infty} J_0\left(k_y \frac{w}{2}\right) \cos\left(k_y y\right) e^{-\left(z\sqrt{k_y^2+k_x^2-k_0^2}\right)} dk_y \right] S_n(k_x) dk_x \Bigg\}
\end{aligned}
\tag{3.139}
$$

An alternative approach to defining the scattered field is covered next.

3.2.4.2 Using Free Space Green's function

Using the free space Green's function, the scattered field can be defined as

$$
\vec{E}(\vec{r}) = \frac{1}{2\pi} \int_{S_A} \left(\hat{n}' \times \vec{E}\right) \times \nabla' \psi dS' \tag{3.140}
$$

where

$$
\nabla\psi = \frac{1+jkR}{R^2} e^{-jkR} \hat{R}, \tag{3.141}
$$

with R being the distance between a field point being considered and the center of the slot. As is done conventionally, the source points are denoted by prime coordinates while the field points are denoted without the prime. The y-directed $\vec{E}$ field can be expressed as

$$E_y(x,y) = V(x)f(y) \tag{3.142}$$

where

$$V(x) = -\int_{\frac{w}{2}}^{-\frac{w}{2}} E_y(x,y)dy. \tag{3.143}$$

Substituting (3.142) in (3.140) leads to

$$\vec{E}(\vec{r}) = \frac{1}{2\pi} \int_{x'=-\frac{L}{2}}^{\frac{L}{2}} \int_{y'=-\frac{w}{2}}^{\frac{w}{2}} \left[\hat{z} \times \hat{y}V(x')f(y')\right] \times \hat{R}\frac{1+jkR}{R^2}e^{(jkR)}dx'dy' \tag{3.144}$$

The distance between the field point

$$\vec{r} = x\hat{x} + y\hat{y} + z\hat{z} \tag{3.145}$$

and the source point

$$\vec{r'} = x'\hat{x} + y'\hat{y} \tag{3.146}$$

is given by

$$\vec{R} = (x - x')\hat{x} + (y - y')\hat{y} + z\hat{z}. \tag{3.147}$$

Assuming that $R >> W$ (the width of the slot),

$$\vec{R} \approx (x - x')\hat{x} + y\hat{y} + z\hat{z} \tag{3.148}$$

and the distance

$$R \approx \sqrt{(x - x')^2 + y^2 + z^2}. \tag{3.149}$$

Substituting $\vec{R}$ from (3.148) in (3.144)

$$\vec{E}(\vec{r}) = \frac{1}{2\pi} \int_{x'=-\frac{L}{2}}^{\frac{L}{2}} \int_{y'=-\frac{W}{2}}^{\frac{W}{2}} \left[-\hat{x} \times (y\hat{y} + z\hat{z})\right] V(x') f(y') \frac{1 + jkR}{R^3} e^{(jkR)} dx' dy' \tag{3.150}$$

which leads to

$$\vec{E}(\vec{r}) = \frac{1}{2\pi} (z\hat{y} - y\hat{z}) \int_{\frac{L}{2}}^{\frac{L}{2}} V(x') \frac{1 + jkR}{R^3} e^{-jkR} dx' \tag{3.151}$$

Again, as done previously in (3.27) – (3.30), V can be represented by a linear combination of piecewise sinusoids so that (3.151) becomes

$$Ey = \frac{z}{2\pi} \sum_{n=-N}^{N} a_n \int_{-\frac{L}{2}}^{\frac{L}{2}} f_0(x' - n\Delta) \frac{1 + jkR}{R^3} e^{-jkR} dx'. \tag{3.152}$$

Using $R = \sqrt{(x-x')^2 + y^2 + z^2}$ and inserting f_0 from (3.30)

$$\begin{aligned} E_y = \frac{z}{2\pi} \sum_{n=-N}^{N} a_n \int_{(n-1)\Delta}^{n\Delta} \sin k_0 \left(x' - (n-1)\Delta\right) \frac{1+jkR}{R^3} e^{(-jk_0R)} dx' \\ + \frac{z}{2\pi} \sum_{n=-N}^{N} a_n \int_{n\Delta}^{(n+1)\Delta} \sin k_0 \left((n-1)\Delta - x'\right) \frac{1+jkR}{R^3} e^{(-jk_0R)} dx' \end{aligned} \tag{3.153}$$

Letting $u = -x' + (n+1)\Delta$ (which implies that $x' = -u + (n+1)\Delta$) and substituting x' in (3.153) leads to

$$\begin{aligned} E_y = \frac{z}{2\pi} \sum_{n=-N}^{N} a_n \int_{0}^{\Delta} \sin k_0 u \frac{1+jk_0R_n}{R_n^3} e^{(-jkR_n)} du \\ + \frac{z}{2\pi} \sum_{n=-N}^{N} a_n \int_{0}^{\Delta} \sin k_0 \frac{1+jk_0\bar{R_n}}{\bar{R_n^3}} e^{\left(-jk_0\bar{R_n}\right)} du \end{aligned} \tag{3.154}$$

where $\bar{R_n} = \sqrt{(x+u-[n+1]\Delta)^2 + y^2 + z^2}$ and $R_n = \sqrt{(x-u-[n-1]\Delta)^2 + y^2 + z^2}$. Rearranging (3.154) gives

$$E_y = \frac{z}{2\pi} \sum_{n=-N}^{N} a_n \int_{0}^{\Delta} \sin k_0 u \left[\frac{1+jk_0R_n}{R_n^3} e^{-jk_0R_n} + \frac{1+jk_0\bar{R_n}}{\bar{R_n}^3} e^{-jk_0\bar{R_n}} \right] du. \tag{3.155}$$

It should be noted that an alternative way of expressing (3.155) is possible by taking advantage of the fact that

$$\left(1 + jk_0R_n\right) e^{-jk_0R_n} = \left(1 + jk_0R_n\right) \left(\cos k_0R_n - j \sin k_0R_n\right) \tag{3.156}$$

leading to

$$\begin{aligned}(1+jk_0R_n)\,e^{-jk_0R_n} &= [\cos k_0R_n + k_0R_n \sin k_0R_n] \\ &+ j\,[k_0R_n\cos k_0R_n - \sin k_0R_n]\,.\end{aligned} \tag{3.157}$$

3.3 Hallen-Type MFIE Formulation (Version 2 MFIE)

Recalling that the Hallen-type MFIE obtained in the previous chapter in Section 2.3.3 from equations (2.68) through (2.71) for $V(x)$ is

$$\begin{aligned}&\int_{-\frac{L}{2}}^{\frac{L}{2}} \Big[G_1(x,x') + G_2(x,x')\Big]\, V(x')dx' \\ &-\left(\frac{k_2^2-k_1^2}{k_2^2}\right)\int_{-\frac{L}{2}}^{x}\left[\int_{-\frac{L}{2}}^{\frac{L}{2}} G_1(u,x')V(x')dx'\right]\sin k_2(x-u)du \\ &= -\frac{1}{k_2}\int_{-\frac{L}{2}}^{x} H(u)\sin k_2(x-u)du - C_1\sin k_2x - C_2\cos k_2x, \\ &\qquad -\frac{L}{2}\le x\le\frac{L}{2},\end{aligned} \tag{3.158}$$

the details of expanding G_1 and G_2 for the second approach employed are outlined. The expression for G_1 from (3.21) is rewritten using the definition of p_1 from (3.6) so that

$$G_1(x,x') = \frac{1}{(2\pi)^2}\frac{2}{j\omega\mu_1}\int_{k_x=-\infty}^{\infty} e^{jk_x(x-x')}\left[\int_{k_y=0}^{\infty}\frac{J_0(k_y\frac{w}{2})}{\sqrt{k_y^2+(k_x^2-k_1^2)}}dk_y\right]dk_x \tag{3.159}$$

as this provides the advantage that the integral contained in square brackets can be expressed in closed form. The aforementioned integral can be defined separately as

$$\Omega(k_x) = \int_{k_y=0}^{\infty} \frac{J_0(k_y \frac{w}{2})}{\sqrt{k_y^2 + (k_x^2 - k_1^2)}} dk_y. \tag{3.160}$$

For real values of k_1, the approach used to compute the integral depends on whether $k_1 < k_x$ or $k_1 > k_x$. For the case where $k_1 < k_x$, using (6.552.1) from [1]

$$\int_0^{\infty} \frac{J_0(xy)}{\sqrt{x^2 + a^2}} dx = I_0\left(\frac{ay}{2}\right) K_0\left(\frac{ay}{2}\right), \quad a > 0 \tag{3.161}$$

leads to

$$\Omega(k_x) = I_0\left(\frac{w}{4}\sqrt{k_x^2 - k_1^2}\right) K_0\left(\frac{w}{4}\sqrt{k_x^2 - k_1^2}\right). \tag{3.162}$$

In order to evaluate the integral when $k_1 > k_x$, $\Omega(k_x)$ is rewritten in the form

$$\Omega(k_x) = \int_0^{\beta} \frac{J_0(k_y \frac{w}{2})}{j\sqrt{\beta^2 - k_y^2}} dk_y + \int_{\beta}^{\infty} \frac{J_0(k_y \frac{w}{2})}{\sqrt{k_y^2 - \beta^2}} dk_y \tag{3.163}$$

where

$$\beta^2 = k_1^2 - k_x^2 > 0. \tag{3.164}$$

Letting $u = \frac{k_y}{\beta}$, (3.163) can be expressed as

$$\Omega(k_x) = \int_0^{1} \frac{J_0(\beta \frac{w}{2} u)}{j\beta\sqrt{1 - u^2}} \beta du + \int_1^{\infty} \frac{J_0(\beta \frac{w}{2} u)}{\beta\sqrt{u^2 - 1}} \beta du. \tag{3.165}$$

The closed form integrals,

$$\int_0^1 \frac{J_0(xy)}{\sqrt{1-x^2}}dx = \frac{\pi}{2}\left[J_0\left(\frac{y}{2}\right)\right]^2 \tag{3.166}$$

and

$$\int_1^\infty \frac{J_0(x,y)}{\sqrt{x^2-1}}dx = -\frac{\pi}{2}J_0\left(\frac{y}{2}\right)Y_0\left(\frac{y}{2}\right), \tag{3.167}$$

from (6.552.4) and (6.552.6) in [1] are used to evaluate the integral in (3.165) so that $\Omega(k_x)$ becomes

$$I(k_x) = -j\frac{\pi}{2}\left[J_0\left(\frac{\beta w}{4}\right)\right]^2 - \frac{\pi}{2}\left[J_0\left(\frac{\beta w}{4}\right)Y_0\left(\frac{\beta w}{4}\right)\right] \tag{3.168}$$

$$= -j\frac{\pi}{2}J_0\left(\frac{\beta w}{4}\right)\left[J_0\left(\frac{\beta w}{4}\right) - jY_0\left(\frac{\beta w}{4}\right)\right] \tag{3.169}$$

$$= -j\frac{\pi}{2}J_0\left(\frac{w}{4}\sqrt{k_1^2-k_x^2}\right)H_0^{(2)}\left(\frac{w}{4}\sqrt{k_1^2-k_x^2}\right), \tag{3.170}$$

since $H_0^{(2)}(z) = J_0(z) - jY_0(z)$. Using (9.6.3) from [1] and remembering that Bessel functions of even order are even functions of their argument,

$$I_0(jz) = J_0(z) \tag{3.171}$$

and

$$K_0(jz) = -j\frac{\pi}{2}H_0^{(2)}(jz), \tag{3.172}$$

Therefore, (3.162) is valid for all k_x. Taking (3.162) and (3.170) and substituting them in for $\Omega(k_x)$, (3.159) can be expressed as

$$G_1(x-x') = \frac{1}{(2\pi)^2}\frac{4}{j\omega\mu_1}\int_{k_x=0}^{\infty} \cos[k_x(x-x')]\Omega(k_x)dk_x \tag{3.173}$$

where

$$\Omega(k_x) = \begin{cases} -j\frac{\pi}{2}J_0\left(\frac{w}{4}\sqrt{k_1^2-k_x^2}\right)H_0^{(2)}\left(\frac{w}{4}\sqrt{k_1^2-k_x^2}\right), & k_x < k_1 \\ I_0\left(\frac{w}{4}\sqrt{k_x^2-k_1^2}\right)K_0\left(\frac{w}{4}\sqrt{k_x^2-k_1^2}\right), & k_x > k_1 \end{cases}. \tag{3.174}$$

Similarly, G_2 can be considered in more detail so that it can be expressed in a form more convenient for computation. Examining (3.22), G_2 can be divided into two portions as

$$G_2(x,x') = G_2^A(x,x') + G_2^B(x,x') \tag{3.175}$$

where

$$G_2^A(x,x') = \frac{1}{(2\pi)^2}\frac{1}{j\omega\mu_2}\iint_{-\infty}^{\infty}\frac{e^{jk_x(x-x')}}{p_2}J_0\left(k_y\frac{w}{2}\right)dk_xdk_y \tag{3.176}$$

and

$$G_2^B(x,x') = \frac{1}{(2\pi)^2}\frac{1}{j\omega\mu_2}\iint_{-\infty}^{\infty}\frac{e^{jk_x(x-x')}}{p_2}\left[\frac{e^{-p_2t}}{\sinh(p_2t)}\right]J_0\left(k_y\frac{w}{2}\right)dk_xdk_y. \tag{3.177}$$

Following a procedure similar to that just outlined for G_1 leads to

$$G_2^A(x-x') = \frac{1}{(2\pi)^2}\frac{4}{j\omega\mu_2}\int_{k_x=0}^{\infty}\cos[k_x(x-x')]\bar{\Omega}(k_x)dk_x \tag{3.178}$$

where

$$\bar{\Omega}(k_x) = I_0\left(\frac{w}{4}\sqrt{k_x^2 - k_2^2}\right) K_0\left(\frac{w}{4}\sqrt{k_x^2 - k_2^2}\right). \tag{3.179}$$

Considering G_2^B further,

$$\begin{aligned} G_2^B(x - x') = \frac{1}{(2\pi)^2}\frac{1}{j\omega\mu_2} \int_{k_x=-\infty}^{\infty} e^{jk_x(x-x')} \times \\ \int_{k_y=-\infty}^{\infty} \frac{J_0(k_y\frac{w}{2})}{p_2}\left[\frac{e^{-p_2 t}}{\sinh(p_2 t)}\right] dk_y dk_x, \end{aligned} \tag{3.180}$$

where as before

$$p_2^2 = k_x^2 + k_y^2 - k_2^2. \tag{3.181}$$

As done in (3.13), the ratio within square brackets can be rewritten using the definition of the sinh function so that

$$\frac{e^{-p_2 t}}{\sinh(p_2 t)} = 2\frac{e^{-2p_2 t}}{1 - 2e^{-2p_2 t}} \tag{3.182}$$

which considering the sum to infinity of a geometric series with common ratio r for $-1 < r < 1$,

$$\sum_{k=0}^{\infty} r^k = \frac{1}{1-r}, \tag{3.183}$$

can be represented in the form of the geometric series

$$2e^{-2p_2 t}\sum_{q=0}^{\infty} e^{-2qp_2 t} = 2\sum_{q=1}^{\infty} e^{-2qp_2 t}. \tag{3.184}$$

Substituting from (3.184) into (3.180) and taking advantage of the even nature of the integrand over k_y leads to

$$G_2^B(x-x') = \frac{1}{(2\pi)^2}\frac{2}{j\omega\mu_2}\sum_{q=1}^{\infty}\int_{k_x=-\infty}^{\infty} e^{jk_x(x-x')}\times \left[\int_{k_y=0}^{\infty}\frac{J_0\left(k_y\frac{w}{2}\right)}{\sqrt{p_2}}e^{-2qp_2t}dk_y\right]dk_x \tag{3.185}$$

Consider the integral

$$I_q(k_x) = \int_0^{\infty}\frac{J_0(k_y\frac{w}{2})}{\sqrt{k_y^2+\beta^2}}e^{-2q\left(\sqrt{k_y^2+\beta^2}\right)t}dk_y \tag{3.186}$$

where

$$\beta^2 = k_x^2 - k_2^2. \tag{3.187}$$

Using (6.637.1) from [1]

$$\int_0^{\infty} e^{-\alpha\sqrt{x^2+\beta^2}}J_0(\gamma x)\frac{dx}{\sqrt{\beta^2+x^2}} = I_0\left(\frac{\beta}{2}\sqrt{\alpha^2+\gamma^2}-\gamma\right)K_0\left(\frac{\beta}{2}\sqrt{\alpha^2+\gamma^2}-\gamma\right), \quad Re\{\alpha\}>0, Re\{\beta\}>0, \gamma>0, \tag{3.188}$$

gives

$$I_q(k_x) = I_0\left(\frac{\sqrt{k_x^2-k_2^2}}{2}\left[\delta q - 2qt\right]\right)K_0\left(\frac{\sqrt{k_x^2-k_2^2}}{2}\left[\delta q + 2qt\right]\right) \tag{3.189}$$

where

$$\delta_q = \sqrt{4q^2t^2 + \frac{w^2}{4}}. \tag{3.190}$$

Going back to (3.185), G_2^B can finally be written as

$$G_2^B(x - x') = \frac{1}{(2\pi)^2} \frac{8}{j\omega\mu_2} \sum_{q=1}^{\infty} \int_{k_x=0}^{\infty} \cos\left[k_x(x - x')\right] I_q(k_x) dk_x. \tag{3.191}$$

3.3.1 MoM Solution

For the MoM solution, pulse functions are employed for the expansion and point matching is implemented. The slot voltage can be expressed as a linear combination of pulse functions so that the voltage is expanded in the form

$$V(x) = \sum_{n=1}^{N} a_n P_n(x) \tag{3.192}$$

where

$$P_n(x) = \begin{cases} 1 & x_n - \frac{\Delta}{2} \leq x \leq x_n + \frac{\Delta}{2} \\ 0 & \text{elsewhere} \end{cases} \tag{3.193}$$

and

$$x_n = -\frac{L}{2} + \left(n - \frac{1}{2}\right)\Delta. \tag{3.194}$$

After substituting the expanded voltage in (3.158) and point-matching at $x = x_m$, the following system of linear equations is obtained

$$\begin{aligned}
&\sum_{n=1}^{N} a_n \int_{x_n-\frac{\Delta}{2}}^{x_n+\frac{\Delta}{2}} \Big[G_1(x_m, x') + G_2(x_m, x')\Big]\, dx' \\
&- \sum_{n=1}^{N} a_n \left(\frac{k_2^2 - k_1^2}{k_2^2}\right) \int_{-\frac{L}{2}}^{x_m} \left[\int_{x_n-\frac{\Delta}{2}}^{x_n+\frac{\Delta}{2}} G_1(u, x')dx'\right] \sin k_2(x_m - u)du \\
&= -\frac{1}{k_2} \int_{-\frac{L}{2}}^{x} H(u) \sin k_2(x-u)du - C_1 \sin k_2 x_m - C_2 \cos k_2 x_m,
\end{aligned} \tag{3.195}$$

$$m = 1, 2, ..., N.$$

The expression in (3.195) can be written as a system of N equations in $N + 2$ unknowns thus

$$\sum_{n=1}^{N} a_n \left(A_{mn} + B_{mn}\right) + C_1 \sin k_2 x_m + C_2 \cos k_2 x_m = b_m \tag{3.196}$$

where

$$A_{mn} = \int_{x_n-\frac{\Delta}{2}}^{x_n+\frac{\Delta}{2}} \Big[G_1(x_m, x') + G_2(x_m, x')\Big]\, dx', \tag{3.197}$$

$$B_{mn} = -\left(\frac{k_2^2 - k_1^2}{k_2^2}\right) \int_{-\frac{L}{2}}^{x_m} \left[\int_{x_n-\frac{\Delta}{2}}^{x_n+\frac{\Delta}{2}} G_1(u, x')dx'\right] \sin k_2(x_m - u)du \tag{3.198}$$

and

$$b_m = -\frac{1}{k_2} \int_{-\frac{L}{2}}^{x} H(u) \sin k_2(x-u) du. \tag{3.199}$$

The two additional equations required to provide a system of $N+2$ equations in $N+2$ unknowns are obtained by implementing the boundary condition on $V(x)$, i.e. $V\left(-\frac{L}{2}\right) = V\left(\frac{L}{2}\right) = 0$.

It is important to note that if $k_1 = k_2$, B_{mn} vanishes and dealing with (3.195) is greatly simplified. On the other hand, if $k_1 \neq k_2$ B_{mn} is difficult to compute. However, here it is used specifically for the free space case where k_1 and k_2 are equal.

3.3.2 Calculation of matrix elements

3.3.2.1 Calculation of A_{mn}

The computation of A_{mn} is considered when the slot is immersed in free space i.e. the backing material is air. For the free-space case, $k_1 = k_2 = k_0$ and A_{mn} from (3.197) can be written in the form

$$A_{mn} = A^1_{mn} + A^2_{mn} + A^3_{mn} \tag{3.200}$$

Splitting G_2 into two portions as done in (3.175), A_{mn} is written as

$$A_{mn} = \int_{x_n - \frac{\Delta}{2}}^{x_n + \frac{\Delta}{2}} \left[G_1(x_m, x') + G_2^A(x_m, x') + G_2^B(x_m, x') \right] dx' \tag{3.201}$$

$$= A^1_{mn} + A^2_{mn} + A^3_{mn}. \tag{3.202}$$

Upon substituting G_1, G_2^A and G_2^B from (3.173), (3.176) and (3.177) respectively, the terms in A_{mn} are

$$A^1_{mn} = \int_{x_n-\frac{\Delta}{2}}^{x_n+\frac{\Delta}{2}} \frac{1}{(2\pi)^2}\frac{4}{j\omega\mu_1}\int_{k_x=0}^{\infty} \cos\left[k_x(x_m-x')\right]\Omega(k_x)dk_x dx', \tag{3.203}$$

$$A^2_{mn} = \int_{x_n-\frac{\Delta}{2}}^{x_n+\frac{\Delta}{2}} \frac{1}{(2\pi)^2}\frac{4}{j\omega\mu_2}\int_{k_x=0}^{\infty} \cos\left[k_x(x_m-x')\right]\bar{\Omega}(k_x)dk_x dx', \tag{3.204}$$

and

$$A^3_{mn} = \int_{x_n-\frac{\Delta}{2}}^{x_n+\frac{\Delta}{2}} \frac{1}{(2\pi)^2}\frac{8}{j\omega\mu_2}\sum_{q=0}^{\infty}\int_{k_x=0}^{\infty} \cos\left[k_x(x_m-x')\right] I_q(k_x)dk_x dx' \tag{3.205}$$

where

$$\Omega(k_x) = \begin{cases} -j\frac{\pi}{2}J_0\left(\frac{w}{4}\sqrt{k_1^2-k_x^2}\right)H_0^{(2)}\left(\frac{w}{4}\sqrt{k_1^2-k_x^2}\right) & k_x < k_1 \\ I_0\left(\frac{w}{4}\sqrt{k_x^2-k_1^2}\right)K_0\left(\frac{w}{4}\sqrt{k_x^2-k_1^2}\right) & k_x > k_1, \end{cases} \tag{3.206}$$

$$\bar{\Omega}(k_x) = I_0\left(\frac{w}{4}\sqrt{k_x^2-k_2^2}\right)K_0\left(\frac{w}{4}\sqrt{k_x^2-k_2^2}\right) \tag{3.207}$$

and

$$I_q(k_x) = I_0\left(\frac{\sqrt{k_x^2-k_2^2}}{2}\left[\delta_q - 2qt\right]\right)K_0\left(\frac{\sqrt{k_x^2-k_2^2}}{2}\left[\delta_q + 2qt\right]\right), \tag{3.208}$$

with

$$\delta_q = \sqrt{4q^2t^2 + \frac{w^2}{4}}. \tag{3.209}$$

Inspecting (3.203), (3.204) and (3.205), it can be seen that if $k_1 = k_2$ then $A^1_{mn} = A^2_{mn}$. For the slot in free-space, $A_{mn} = 2A^1_{mn}$. Considering A^1_{mn} alone, if the integral in (3.203) is assumed to be uniformly convergent then the integrals can be rearranged with the expression becoming

$$A^1_{mn} = \frac{1}{(2\pi)^2}\frac{4}{j\omega\mu_1}\int_{k_x=0}^{\infty} \Omega(k_x)\left[\int_{x_n-\frac{\Delta}{2}}^{x_n+\frac{\Delta}{2}} \cos k_x(x' - x_m)dx'\right] dk_x. \tag{3.210}$$

After computing the integral in the square brackets in (3.210),

$$A^1_{mn} = \frac{1}{2\pi^2}\frac{4}{j\omega\mu_1}\int_{k_x=0}^{\infty} \Omega(k_x)\frac{\sin\frac{k_x\Delta}{2}}{k_x}\cos\left[k_x(m-n)\Delta\right] dk_x. \tag{3.211}$$

Let $l = m - n$. Substituting $\Omega(k_x)$ from (3.206) into (3.211),

$$\begin{aligned} A^1_{mn} =& \frac{1}{2\pi^2}\frac{4}{j\omega\mu_1}\left(-j\frac{\pi}{2}\right)\int_0^{k_1}\frac{\sin\frac{k_x\Delta}{2}}{k_x}\cos k_x l\Delta J_0^2\left(\frac{w}{4}\sqrt{k_1^2-k_x^2}\right)dk_x + \\ & \frac{1}{2\pi^2}\frac{4}{j\omega\mu_1}\left(\frac{-\pi}{2}\right)\int_0^{k_1}\frac{\sin\frac{k_x\Delta}{2}}{k_x}\cos k_x l\Delta J_0\left(\frac{w}{4}\sqrt{k_1^2-k_x^2}\right)\times \\ & \qquad Y_0\left(\frac{w}{4}\sqrt{k_1^2-k_x^2}\right)dk_x + \\ & \frac{1}{2\pi^2}\frac{4}{j\omega\mu_1}\int_{k_1}^{\infty}\frac{\sin\frac{k_x\Delta}{2}}{k_x}\cos k_x l\Delta I_0\left(\frac{w}{4}\sqrt{k_x^2-k_1^2}\right)K_0\left(\frac{w}{4}\sqrt{k_x^2-k_1^2}\right)dk_x. \end{aligned} \tag{3.212}$$

As done in equations (3.69) through (3.72), the third integral in (3.212) can be expressed in the form $\int_K^\infty \left[f(k_x) - f^A(k_x)\right] dk_x + \int_K^\infty f^A(k_x) dk_x$ where $f^A(k_x)dk_x$ is the large-argument asymptotic form of the integrand. Again, this is done because the difference in the integral of the difference in square brackets converges more rapidly than the original integral. The third integrand from (3.212) can be rewritten so that

$$\begin{aligned} &\frac{\sin\frac{k_x\Delta}{2}}{k_x}\cos k_x l\Delta I_0\left(\frac{w}{4}\sqrt{k_x^2-k_1^2}\right)K_0\left(\frac{w}{4}\sqrt{k_x^2-k_1^2}\right) \\ &\quad = \frac{1}{2k_x}\left[\sin k_x\left(l+\frac{1}{2}\right)\Delta - \sin k_x\left(l-\frac{1}{2}\right)\Delta\right]\times \\ &\qquad I_0\left(\frac{w}{4}\sqrt{k_x^2-k_1^2}\right)K_0\left(\frac{w}{4}\sqrt{k_x^2-k_1^2}\right) \end{aligned} \tag{3.213}$$

which can be approximated as

$$\begin{aligned} &\frac{\sin\frac{k_x\Delta}{2}}{k_x}\cos k_x l\Delta I_0\left(\frac{w}{4}\sqrt{k_x^2-k_1^2}\right)K_0\left(\frac{w}{4}\sqrt{k_x^2-k_1^2}\right) \\ &\approx \frac{1}{2k_z}\left[\sin k_x\left(l+\frac{1}{2}\right)\Delta - \sin k_x\left(l-\frac{1}{2}\right)\Delta\right]\frac{2}{w}\frac{1}{\sqrt{k_x^2-k_1^2}} \end{aligned} \tag{3.214}$$

as k_x approaches infinity. Simplifying (3.214) further leads to

$$\begin{aligned} &\frac{\sin\frac{k_x\Delta}{2}}{k_x}\cos k_x l\Delta I_0\left(\frac{w}{4}\sqrt{k_x^2-k_1^2}\right)K_0\left(\frac{w}{4}\sqrt{k_x^2-k_1^2}\right) \\ &\approx \frac{1}{w}\frac{\sin k_x\left(l+\frac{1}{2}\right)\Delta - \sin k_x\left(l-\frac{1}{2}\right)\Delta}{k_x^2}. \end{aligned} \tag{3.215}$$

Thus, the third integral in (3.211) can be computed by taking advantage of (3.215) and using the relation

$$\int_1^\infty \frac{\sin(ax)}{x^2}dx = \sin(a) - a\,\mathrm{Ci}(a) \tag{3.216}$$

where

$$\mathrm{Ci}(x) = -\int_{x}^{\infty} \frac{\cos t}{t} dt \tag{3.217}$$

is the cosine integral. The expression in (3.216) is obtained since it is known from (3.721.1) in [1] that

$$\int_{1}^{\infty} \frac{\cos(ax)}{x} dx = -\mathrm{Ci}(a) \tag{3.218}$$

and by employing integration by parts. Therefore, A^1_{mn} becomes

$$\begin{aligned}
A^1_{mn} =& \frac{1}{2\pi^2} \frac{4}{j\omega\mu_1} \left(-j\frac{\pi}{2}\right) \int_0^{k_1} \frac{\sin\frac{k_x\Delta}{2}}{k_x} \cos k_x l\Delta J_0^2 \left(\frac{w}{4}\sqrt{k_1^2 - k_x^2}\right) dk_x \\
&+ \frac{1}{2\pi^2} \frac{4}{j\omega\mu_1} \left(\frac{-\pi}{2}\right) \int_0^{k_1} \frac{\sin\frac{k_x\Delta}{2}}{k_x} \cos k_x l\Delta J_0 \left(\frac{w}{4}\sqrt{k_1^2 - k_x^2}\right) \times \\
&\qquad Y_0 \left(\frac{w}{4}\sqrt{k_1^2 - k_x^2}\right) dk_x \\
&+ \frac{1}{2\pi^2} \frac{4}{j\omega\mu_1} \int_{k_1}^{\infty} \left[\frac{\sin\frac{k_x\Delta}{2}}{k_x} \cos k_x l\Delta \left(I_0 \left(\frac{w}{4}\sqrt{k_x^2 - k_1^2}\right) \times \right.\right. \\
&\qquad \left.\left. K_0 \left(\frac{w}{4}\sqrt{k_x^2 - k_1^2}\right) - \frac{2}{wk_x} \right) dk_x \right] \\
&+ \frac{1}{2\pi^2} \frac{4}{j\omega\mu_1} \frac{1}{k_1 w} \left(2\cos\left[k_1 l\Delta\right] \sin\left[k_1 \frac{\Delta}{2}\right] \right. \\
&\qquad \left. - k_1 \left(l + \frac{1}{2}\right) \Delta\, \mathrm{Ci}\left[k_1 \left(l + \frac{1}{2}\Delta\right)\right] \right) \\
&+ \frac{1}{2\pi^2} \frac{4}{j\omega\mu_1} \frac{1}{k_1 w} \left(k_1 \left(l - \frac{1}{2}\right) \Delta\, \mathrm{Ci}\left[k_1 \left(l - \frac{1}{2}\right) \Delta\right] \right).
\end{aligned} \tag{3.219}$$

A^2_{mn} is computed in a similar fashion as A^1_{mn}. Moving on to A^3_{mn} alone, following the

same procedure as in (3.210) A^3_{mn} can be rewritten as

$$A^3_{mn} = \frac{1}{2\pi^2}\frac{8}{j\omega\mu_2}\sum_{q=1}^{\infty}\int_{k_x=0}^{\infty} I_q(k_x)\frac{\sin\frac{k_x\Delta}{2}}{k_x}\cos k_x(m-n)\Delta dk_x. \tag{3.220}$$

Again, let $l = m - n$. Substituting from (3.208) into (3.220) leads to

$$\begin{aligned}
A^3_{mn} = {} & \frac{1}{2\pi^2}\frac{8}{j\omega\mu_2}\left(-j\frac{\pi}{2}\right)\sum_{q=1}^{\infty}\int_{k_x=0}^{k_2}\frac{\sin\frac{k_x\Delta}{2}}{k_x}\cos k_x l\Delta\times \\
& J_0\left(\frac{\sqrt{k_2^2-k_x^2}}{2}\left[\delta_q - 2qt\right]\right) J_0\left(\frac{\sqrt{k_2^2-k_x^2}}{2}\left[\delta_q + 2qt\right]\right) dk_x \\
& + \frac{1}{2\pi^2}\frac{8}{j\omega\mu_2}\left(\frac{-\pi}{2}\right)\sum_{q=1}^{\infty}\int_{k_x=0}^{k_2}\frac{\sin\frac{k_x\Delta}{2}}{k_x}\cos k_x l\Delta\times \\
& J_0\left(\frac{\sqrt{k_2^2-k_x^2}}{2}\left[\delta_q - 2qt\right]\right) Y_0\left(\frac{\sqrt{k_2^2-k_x^2}}{2}\left[\delta_q + 2qt\right]\right) dk_x \\
& + \frac{1}{2\pi^2}\frac{8}{j\omega\mu_2}\sum_{q=1}^{\infty}\int_{k_x=k_2}^{\infty}\frac{\sin\frac{k_x\Delta}{2}}{k_x}\cos k_x l\Delta\times \\
& I_0\left(\frac{\sqrt{k_x^2-k_2^2}}{2}\left[\delta_q - 2qt\right]\right) K_0\left(\frac{\sqrt{k_x^2-k_2^2}}{2}\left[\delta_q + 2qt\right]\right) dk_x.
\end{aligned} \tag{3.221}$$

3.3.2.2 Calculation of B_{mn}

Recall from (3.195) that

$$B_{mn} = \frac{k_2^2-k_1^2}{k_2^2}\int_{-\frac{L}{2}}^{x_m}\left[\int_{x_n-\frac{\Delta}{2}}^{x_n+\frac{\Delta}{2}} G_1\left(u,x'\right)dx'\right]\sin k_2\left(x_m-u\right)du. \tag{3.222}$$

Let a new function $\mathfrak{I}$ be set as

$$\mathfrak{I}(u) = \int_{x_n-\frac{\Delta}{2}}^{x_n+\frac{\Delta}{2}} G_1\left(u, x'\right) dx'. \tag{3.223}$$

Inserting the expression for G_1 from (3.173)

$$\mathfrak{I}(u) = \int_{x_n-\frac{\Delta}{2}}^{x_n+\frac{\Delta}{2}} \frac{-1}{(2\pi)^2} \frac{8}{2j\omega\mu_1} \int_{k_x=0}^{\infty} \cos\left[k_x\left(u-x'\right)\right] I(k_x) dk_x dx' \tag{3.224}$$

Rearranging,

$$\mathfrak{I}(u) = -\frac{1}{2\pi} \frac{2}{j\omega\mu_1} \int_{k_x=0}^{\infty} I(k_x) \left[\int_{x_n-\frac{\Delta}{2}}^{x_n+\frac{\Delta}{2}} \cos\left[k_x\left(x'-u\right)\right] dx' \right] dk_x \tag{3.225}$$

and letting $y = x' - u$

$$\mathfrak{I}(u) = -\frac{1}{2\pi^2} \frac{2}{j\omega\mu_1} \int_{k_x=0}^{\infty} I(k_x) \left[\int_{x_n-\frac{\Delta}{2}-u}^{x_n+\frac{\Delta}{2}-u} \cos k_x y dy \right] dk_x \tag{3.226}$$

gives

$$\mathfrak{I}(u) = -\frac{1}{2\pi^2} \frac{2}{j\omega\mu_1} \int_{k_x=0}^{\infty} I(k_x) \left[2\frac{\sin\left(k_x\frac{\Delta}{2}\right)}{k_x} \cos k_x\left(u-x_n\right) \right] dk_x \tag{3.227}$$

after evaluating the integral in brackets.

Rearranging (3.227) leads to

$$\mathcal{I}(u) = -\frac{1}{2\pi^2}\frac{4}{j\omega\mu_1}\int_{k_x=0}^{\infty} I(k_x)\frac{\sin\left(k_x\frac{\Delta}{2}\right)}{k_x}\cos\left(k_x(u-x_n)\right)dk_x. \tag{3.228}$$

Inserting (3.228) into (3.222) gives

$$\begin{aligned} B_{mn} = -\frac{k_2^2-k_1^2}{k_2^2}\int_{-\frac{L}{2}}^{x_m}\Bigg[-\frac{1}{2\pi^2}\frac{4}{j\omega\mu_1}\int_{k_x=0}^{\infty} I(k_x)\frac{\sin k_x\frac{\Delta}{2}}{k_x}\cos k_x(u-x_n)\Bigg] \\ \times \sin k_2(x_m-u)du. \end{aligned} \tag{3.229}$$

Let $\mathcal{V}$ be defined as

$$\mathcal{V}(k_x) = \int_{-\frac{L}{2}}^{x_m}\cos\left(k_x(x_n-u)\right)\sin\left(k_2(x_m-u)\right)du \tag{3.230}$$

which becomes

$$\begin{aligned} \mathcal{V}(k_x) = \frac{\cos\left[k_xx_n+k_2x_m-u(k_x+k_2)\right]}{2(k_x+k_2)}\Bigg|_{-\frac{L}{2}}^{x_m} \\ -\frac{\cos\left[k_xx_n-u-k_2(x_m-u)\right]}{2(k_x-k_2)}\Bigg|_{-\frac{L}{2}}^{x_m} \end{aligned} \tag{3.231}$$

after carrying out the integration. Since $x_n = -\frac{L}{2}+\left(n-\frac{1}{2}\Delta\right)$,

$$\begin{aligned} \mathcal{V}(k_x) = \frac{1}{2(k_x+k_2)}\Bigg\{\cos\left(k_xx_n+k_2x_m-k_xx_m-k_2x_m\right) \\ -\cos\left(k_xx_n+k_2x_m+k_x\left(\frac{L}{2}\right)+k_2\left(\frac{L}{2}\right)\right)\Bigg\} \\ +\frac{1}{2(k_x-k_2)}\Bigg\{\cos\left(k_xx_m-x_m\right)\big)-\cos\left(k_xx_m+\frac{L}{2}-k_2\left(x_m+\frac{L}{2}\right)\right)\Bigg\}. \end{aligned} \tag{3.232}$$

Rearranging results in

$$\mathcal{V}(k_x) = \frac{1}{2(k_x + k_2)} \times \left\{ \cos\left[k_x x_n + k_2 x_m - k_x x_m - k_2 x_m\right] - \cos\left[k_x x_n + k_2 x_m + k_x \frac{L}{2} + k_2 \frac{L}{2}\right] \right\} - \frac{1}{2(k_x - k_2)} \left\{ \cos[k_x(x_n - x_m)] - \cos\left[k_x\left(x_n + \frac{L}{2}\right) - k_2\left(x_m + \frac{L}{2}\right)\right] \right\}, \tag{3.233}$$

and simplifying leads to

$$\mathcal{V}(k_x) = \frac{1}{2(k_x + k_2)} \times \left\{ \cos\left[k_x x_n + k_2 x_m - k_x x_m - k_2 x_m\right] - \cos\left[k_x\left(x_n + \frac{L}{2} - k_2\left(x_m + \frac{L}{2}\right)\right)\right] \right\} - \frac{1}{2(k_x - k_2)} \left\{ \cos[k_x(x_n - x_m)] - \cos\left[k_x\left(x_n + \frac{L}{2}\right) + k_2\left(x_m + \frac{L}{2}\right)\right] \right\}. \tag{3.234}$$

Expanding (3.234) leads to

$$\begin{aligned} \mathcal{V}(k_x) = \frac{1}{2}\cos\left(k_x(m-n)\Delta\right)\left[\frac{1}{k_x + k_2} - \frac{1}{k_x - k_2}\right] \\ -\frac{1}{2}\left[\cos\left(k_x\left(n - \frac{1}{2}\right)\Delta\right)\cos\left(k_x\left(m - \frac{1}{2}\right)\Delta\right)\right. \\ \left. -\sin\left(k_x\left(n - \frac{1}{2}\right)\Delta\right)\sin\left(k_x\left(m - \frac{1}{2}\right)\Delta\right)\right]\frac{1}{k_x + k_2} \\ +\frac{1}{2}\left[\cos\left(k_x\left(n - \frac{1}{2}\right)\Delta\right)\cos\left(k_x\left(m - \frac{1}{2}\right)\Delta\right)\right. \\ \left. +\sin\left(k_x\left(n - \frac{1}{2}\right)\Delta\right)\sin\left(k_x\left(m - \frac{1}{2}\right)\Delta\right)\right]\frac{1}{k_x - k_2} \end{aligned} \tag{3.235}$$

Invoking the trigonometric identity,

$$\begin{aligned} \mathcal{V}(k_x) == \frac{1}{2}\cos\Big(k_x(m-n)\Delta\Big)\left[\frac{1}{k_x + k_2} - \frac{1}{k_x - k_2}\right] \\ -\frac{1}{2}\cos\Big(k_x(n - \tfrac{1}{2})\Delta\Big)\cos\Big(k_2(m - \tfrac{L}{2})\Delta\Big)\left[\frac{1}{k_x + k_2} - \frac{1}{k_x - k_2}\right] \\ +\frac{1}{2}\sin\Big(k_x(n - \tfrac{1}{2})\Delta\Big)\sin\Big(k_2(m - \tfrac{L}{2})\Delta\Big)\left[\frac{1}{k_x + k_2} + \frac{1}{k_x - k_2}\right] \end{aligned} \tag{3.236}$$

3.3.3 Calculation of Right Hand-Side Elements

3.3.3.1 Plane Wave Incidence (Scattering Problem)

Considering plane wave excitation as depicted in Figure 3.1, the total excitation field is given by

$$\begin{aligned}\vec{H}^i + \vec{H}^r = &-\hat{z}2j\frac{E_0}{\eta_0}e^{(jkx\sin\theta_0)}\sin\theta_0\sin\Big(k_0 z\cos\theta_0\Big)\\ &+\hat{x}2\frac{E_0}{\eta_0}e^{(jk_0x\sin\theta_0)}\cos\theta_0\cos\Big(k_0 z\cos\theta_0\Big)\end{aligned} \tag{3.237}$$

In the plane of the aperture where $z = 0$,

$$\vec{H}^i + \vec{H}^r = 2\hat{x}\frac{E_0}{\eta_0}\cos\theta_0 e^{(jk_0x\sin\theta_0)} \tag{3.238}$$

which in the case of normal incidence, is

$$\vec{H}^i + \vec{H}^r = 2\hat{x}\frac{E_0}{\eta_0}. \tag{3.239}$$

Recalling that

$$b_m = \frac{1}{k_2}\int_{-\frac{L}{2}}^{x_m} H(u)\sin k_2\left(k_2(x_m-u)\right)du \tag{3.240}$$

gives for normal incidence

$$b_m = \frac{1}{k_2}\int_{-\frac{L}{2}}^{x_m} 2\frac{E_0}{\eta_0}\cos\theta_0 e^{(jk_0u\sin\theta_0)}\sin k_2(x_m-u)du \tag{3.241}$$

after substituting $H(u)$. Setting a variable $w = x_m - u$, leads to

$$b_m = -2\frac{E_0}{\eta_0 k_2}\cos\theta_0 \int_{-\frac{L}{2}}^{x_m} e^{u[jk_0\sin\theta_0]}\sin k_2(x_m - u)du, \tag{3.242}$$

or

$$b_m = -2\frac{E_0\cos\theta_0}{\eta_0 k_2} \int_{0}^{\left(m-\frac{1}{2}\right)\Delta} e^{(x_m jk_0\sin\theta_0)}e^{(-wjk_0\sin\theta_0)}\sin k_2 w dw, \tag{3.243}$$

given that $x_n = -\frac{L}{2} + \left(n - \frac{1}{2}\right)\Delta$. Evaluating the integral in (3.243) leads to

$$\begin{aligned} b_m &= -2\frac{E_0\cos\theta_0}{\eta_0 k_2}e^{jk_0 x_m\sin\theta_0} \\ &\times \left\{ \frac{e^{-jk_0 u\sin\theta_0}}{k_2^2 - k_0^2\sin^2\theta_0}\left[-jk_0\sin\theta_0\sin k_2 u - k_2\cos k_2 u\right]\Big|_0^{\left(m-\frac{1}{2}\right)\Delta} \right\} \end{aligned} \tag{3.244}$$

which, after inserting the limits, gives

$$\begin{aligned} b_m &= -2\frac{E_0\cos\theta_0}{\eta_0 k_2}e^{jk_0 x_m\sin\theta_0} \\ &\times \left\{ \frac{e^{-jk_0 u\sin\theta_0}}{k_2^2 - k_0^2\sin^2\theta_0}\left[-jk_0\sin\theta_0\sin k_2(m-1)\Delta - k_2\cos k_2(m-1)\Delta\right] \right\}. \end{aligned} \tag{3.245}$$

3.3.3.2 Line-Current Excitation (Radiation Problem)

As mentioned earlier, the radiation problem is also considered because it is employed later for validation purposes. In doing this, a line source is placed at the center of the slot and the resulting field is calculated. Figure 3.2 illustrates the problem.

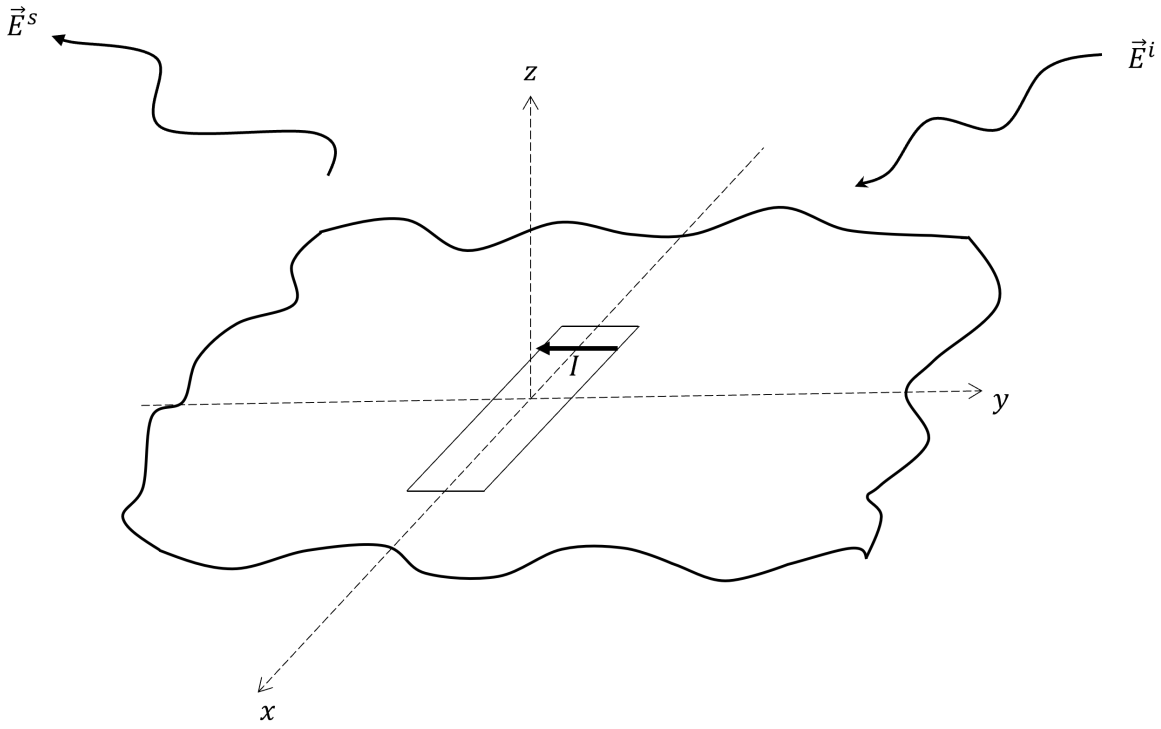

Figure 3.2: Figure showing line-current excitation in the plane of the slot.

Recall that

$$b_m = -\frac{1}{k_2} \int_{-\frac{L}{2}}^{x_m} H(u) \sin k_2(x_m - u) du \tag{3.246}$$

Since

$$H(x) = H^i(x, 0) + Ii(x, 0) \tag{3.247}$$

and

$$i(x, 0) = \delta(x - x_0) \tag{3.248}$$

(3.246) becomes

$$b_m = -\frac{I}{k_2} \int_{-\frac{L}{2}}^{x_m} \delta(u - x_0) \sin k_2(x_m - u) du \tag{3.249}$$

which implies that

$$b_m = \begin{cases} 0, & x_m < x_0 \\ -\frac{I}{k_2} \sin k_2(x_m - x_0), & x_m > x_0 \end{cases} . \tag{3.250}$$

3.3.4 Calculation of Scattered Field for Plane Wave Incidence

3.3.4.1 Using Free Space Green's Function

Consider Figure 3.2. The electric field can be expressed as [7]

$$\vec{E}(\vec{r}) = \frac{1}{2\pi} \int_{S_A} \left(\hat{n}' \times \vec{E} \right) \times \nabla' \psi ds' \tag{3.251}$$

where

$$\nabla' \psi = \frac{1 + jkR}{R^2} e^{-jkR} \hat{R} \tag{3.252}$$

with R being the distance between the source and field points and ψ some field quantity. Recalling from (3.142) that

$$E_y(x, y) = V(x) f(y), \tag{3.253}$$

results in

$$\vec{E}(\vec{r}) = \frac{1}{2\pi} \int_{x'=-\frac{L}{2}}^{\frac{L}{2}} \int_{y'=-\frac{w}{2}}^{\frac{w}{2}} \left[\hat{z} \times \hat{y} V(x') f(y') \right] \times \hat{R} \frac{1 + jkR}{R^2} e^{-jkR} dk x' dy'. \tag{3.254}$$

If it is assumed that the radial distance from the field point to the center of the slot is considerably larger than the width of the slot ($R \gg w$), then

$$\vec{r} = \hat{x}x + \hat{y}y + \hat{z}z, \tag{3.255}$$

and

$$\vec{r}' \approx \hat{x}x'. \tag{3.256}$$

This results in $\vec{R}$ being approximated as

$$\vec{R} = \vec{r} - \vec{r}\,' \approx (x - x')\hat{x} + y\hat{y} + z\hat{z} \tag{3.257}$$

so that

$$R \approx \sqrt{(x-x')^2 + y^2 + z^2}. \tag{3.258}$$

Substituting R into (3.254) gives

$$\vec{E}(\vec{r}) = \frac{1}{2\pi} \int_{x'=-\frac{L}{2}}^{\frac{L}{2}} \int_{y'=-\frac{w}{2}}^{\frac{w}{2}} \left[-\hat{x} \times (y\hat{y} + z\hat{z})\right] V(x') f(y') \frac{1+jkR}{R^3} e^{-jkR} dx' dy' \tag{3.259}$$

which becomes

$$\vec{E}(\vec{r}) = \frac{1}{2\pi} = (z\hat{y} - y\hat{z}) \int_{-\frac{L}{2}}^{\frac{L}{2}} V(x') \frac{1+jkR}{R^3} e^{-jkR} dx' \tag{3.260}$$

after considering that the integral over y' is unity. Choosing the voltage $V(x')$ as a linear combination of pulse functions as done earlier, the y-component of the E-field is

$$E_y = \frac{z}{2\pi} \sum_{n=1}^{N} a_n \int_{x_n - \frac{\Delta}{2}}^{x_n + \frac{\Delta}{2}} \frac{1+jkR}{R^3} e^{-jkR} dx'. \tag{3.261}$$

After replacing the exponential function using Euler's relation, E_y becomes

$$E_y = \frac{z}{2\pi} \sum_{n=1}^{N} a_n \int_{x_n - \frac{\Delta}{2}}^{x_n + \frac{\Delta}{2}} \frac{1}{R^3} \left[\cos kR - j \sin kR + jkR \cos kR + kR \sin kR\right] dx' \tag{3.262}$$

and separating real an imaginary parts,

$$E_y = \frac{z}{2\pi} \sum_{n=1}^{N} a_n \times \left[\int_{x_n - \frac{\Delta}{2}}^{x_n + \frac{\Delta}{2}} \frac{kR \sin kR + \cos kR}{R^3} dx' + j \int_{x_n - \frac{\Delta}{2}}^{x_n + \frac{\Delta}{2}} \frac{kR \cos kR - \sin kR}{R^3} dx' \right]. \tag{3.263}$$

3.4 Considerations for Numerical Accuracy

It is important to understand the accuracy of the solution for the scattered field. This makes it possible for error analysis to be carried out to determine the optimal slot design. There are several variables to be considered so far as the numerical accuracy of the results are concerned. First, the numerical integration involved in computing the MoM entries must be done with prescribed accuracy. Second, the number of partitions in the MoM solution must be set appropriately. Lastly, the number of terms used in the expansion of the Green's function must also be carefully chosen.

Investigations are carried out to assess the effects of the number of partitions and the number of terms in the Green's function expansion on the accuracy of the MoM solution. A slot with dimensions 20 mm by 1 mm cut into a metallic screen above a layer of the commercial MagRAM FGM-125 ($\epsilon_r = 7.32 - j0.0464$ and $\mu_r = 0.576 - j0.484$) in the normal incidence case is considered at 2.88 GHz. In both cases, the parameter numbers required for stabilization are examined. As used here, "stabilization" denotes when the difference between successive terms is less than the accuracy of the network analyzer used for measurements (an Agilent 8510C VNA) which is 0.04 dB and 2° for the magnitude and phase, respectively. Figures 3.3 through 3.6 show the results. From the figures, it can be seen that the scattered field satisfies the required criteria when the number of Green's functions terms and number of slot partitions used in computation are 25 and 41, respectively. The accuracy attained at this point for the scattered field is comparable to that of the measurement system used in

the laboratory. Both numbers are used in subsequent investigations into the error analysis described later. Similar results have been obtained with different slot dimensions. It is important to note that it is possible to change the parameters to suit computations with different slot dimensions.

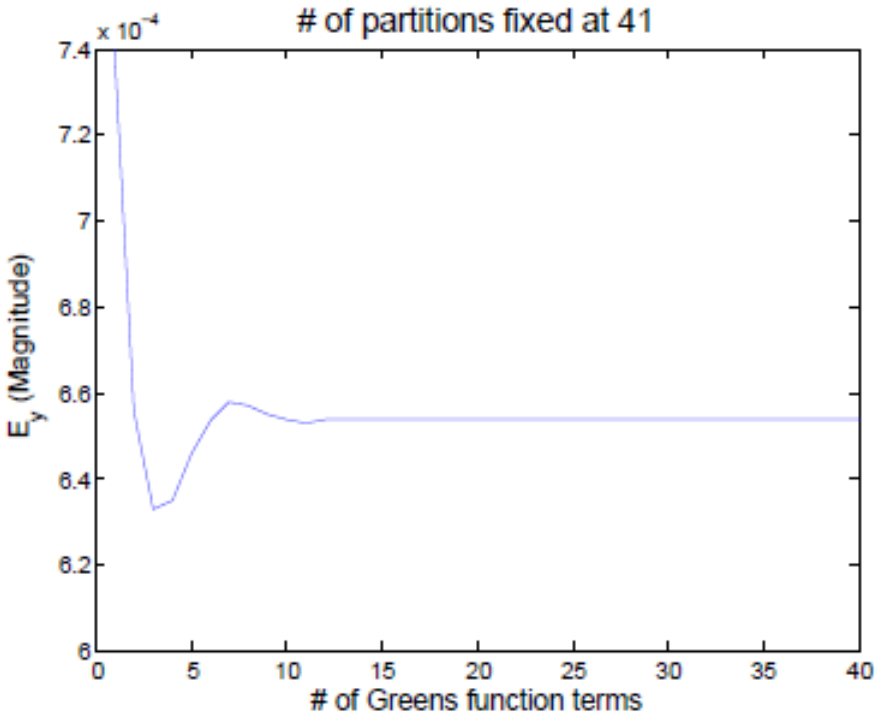

Figure 3.3: Magnitude of the scattered field computed for a slot above a conductor-backed layer of FGM-125 as a function of the number of terms used in the Greens function expansion. Number of partitions is $N = 41$.

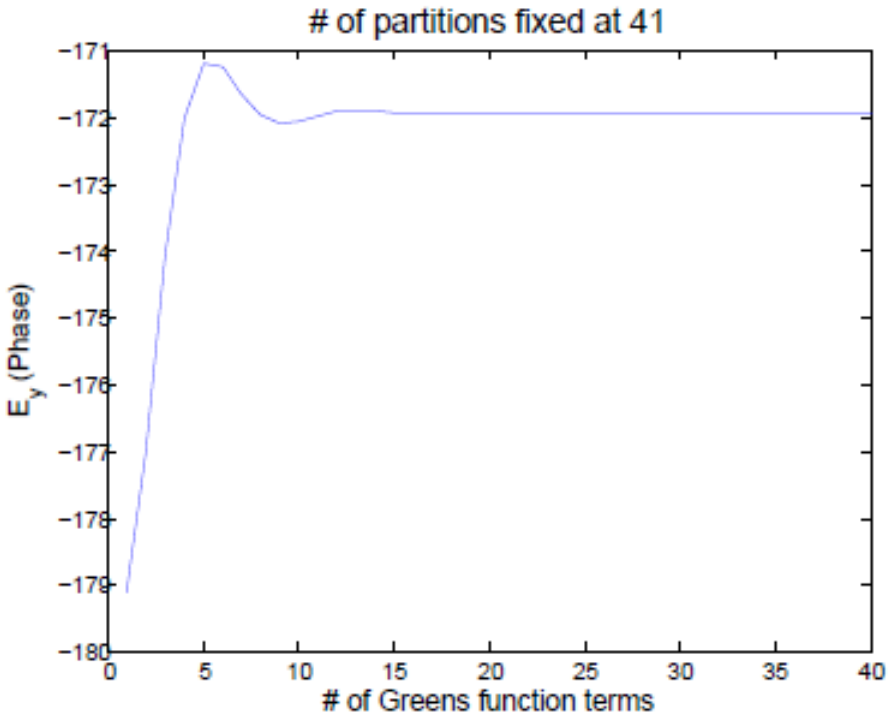

Figure 3.4: Phase of the scattered field computed for a slot above a conductor-backed layer of FGM-125 as a function of the number of terms used in the Greens function expansion. Number of partitions is $N = 41$.

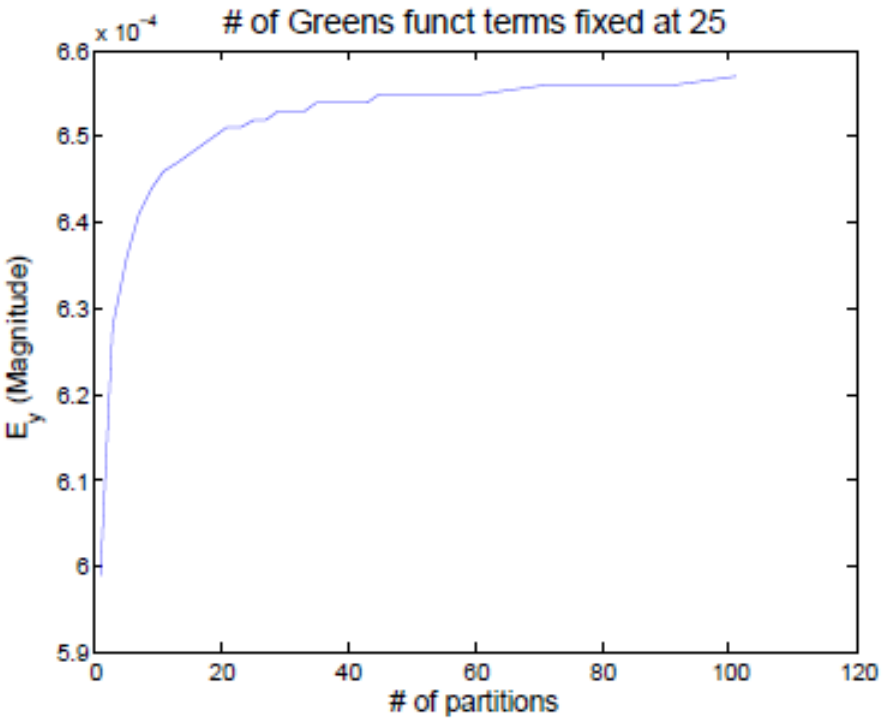

Figure 3.5: Magnitude of the scattered field computed for a slot above a conductor-backed layer of FGM-125 as a function of the Number of partitions. Number of terms used in the Greens function expansion is 25.

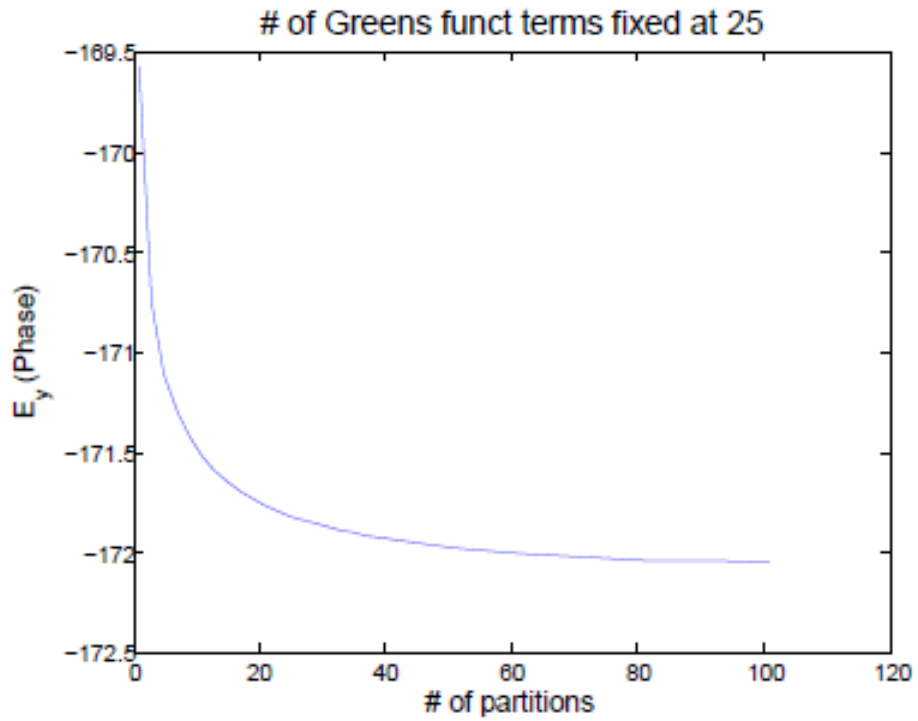

Figure 3.6: Phase of the scattered field computed for a slot above a conductor-backed layer of FGM-125 as a function of the number of partitions. Number of terms used in the Greens function expansion is 25.

3.5 Solution Validation

In order to validate the solutions outlined in the preceding sections, the results must be compared against known numerical results. No results were found in the literature for comparison for the case of the field scattered by a slot in an aperture screen above a material layer. However, the literature search yielded references to compare against the radiation of a slot antenna. Assuming a line source excitation, the input impedance of the slot antenna can be compared to published results. The results in [8] allow for comparison against slot antenna radiation above a dielectric half-space and above a conductor-backed dielectric. The slot antenna radiation characteristics are considered in free-space, above a half-space of dielectric material and above a conductor-backed free-space region.

Given a line source with amplitude I placed at a position $x = x_0$, as shown in Figure 3.2, the input impedance can be found once the voltage across the slot has been computed as

$$V(x) = \sum_{n=-N}^{N} a_n f(x - n\Delta). \tag{3.264}$$

The input impedance, which can be expressed as

$$Z_{in} = R + jX, \tag{3.265}$$

is given by

$$Z_{in} = \frac{\sum_{n=-N}^{N} a_n f(x - n\Delta)}{I}. \tag{3.266}$$

3.5.1 Slot Antenna above a Half-Space Material Layer and above a Conductor-backed Material Layer

The input impedance of a center-fed slot antenna above a half-space of dielectric material is computed. The material considered has a permittivity of $\epsilon_r = 2.55$. The results obtained, shown in Figure 3.7, are compared with the work done by Kominami et al [9]. The slot impedance plot in Figure 4 of [9] agrees closely with that in Figure 3.7. The discrepancy in the results is likely attributable to the use of EDB (entire-domain basis) functions by the authors of the paper for the representation of the slot voltage, whereas PWS (piecewise sinusoidal) functions are used in this work.

The case of a slot above a conductor-backed layer of the same dielectric material ($\epsilon_r = 2.55$) is also shown in Figure 3.7, although this case is not considered by the authors. The thickness of the material layer considered is $t = 0.25\lambda_0$. It is instructive to note that the input resistance is considerably higher in the vicinity of the resonance and exhibits a narrower Q-curve for the conductor-backed case. This suggests that the inclusion of the conductor backing accentuates the resonance.

Finally, a slot antenna placed above a layer of MagRAM FGM-125 is examined and the input impedance is computed as a function of slot normalized length. First, a case of a half-space of FGM-125 is considered and then a case with a 1/8 inch thick layer of FGM-125 is also considered. The results obtained are shown in Figure 3.8. The Q of the conductor backed antenna is lower than that of the half-space case. This is due to dissipation of energy in the material. The bandwidth of the antenna is quite significant when compared against the lossless case in Figure 3.7 and this bodes well for wideband characterization of absorbing materials.

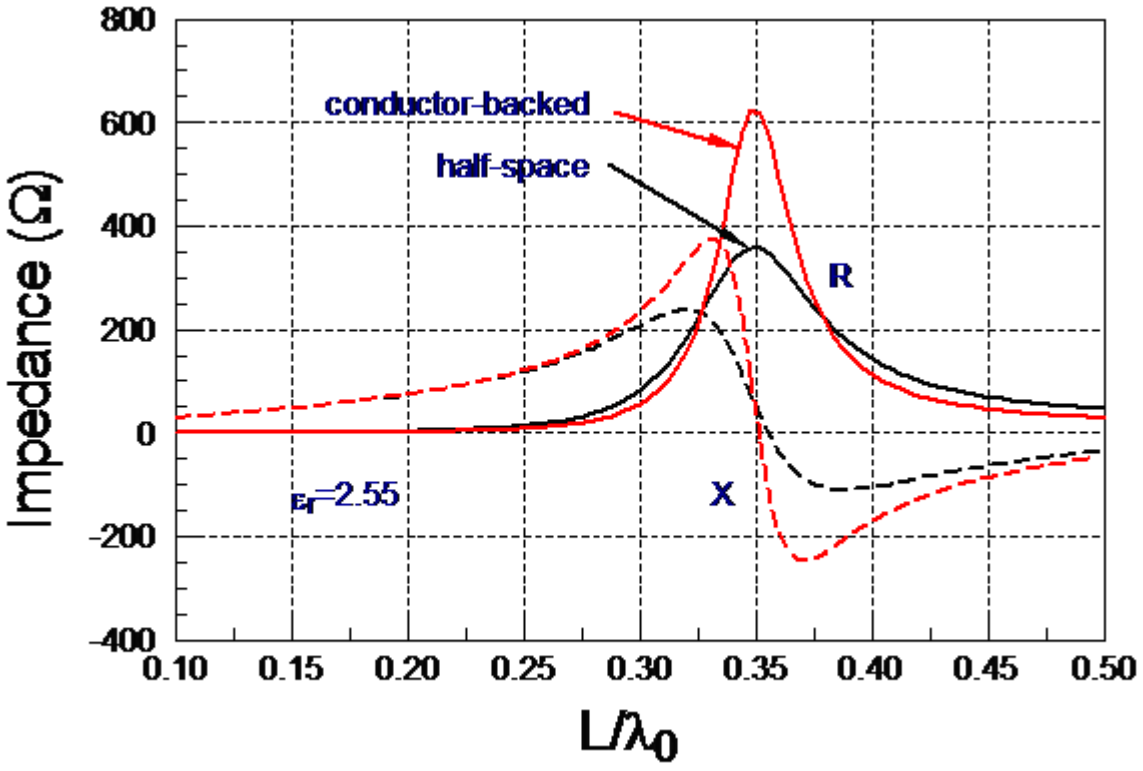

Figure 3.7: Input impedance of a slot antenna located in a conducting screen above a half space with $\epsilon = 2.55\epsilon_0$ and $\mu = \mu_0$ and above a conductor-backed layer with the same properties. The slot length is L and the slot width is $w = 0.02L$. The layer thickness for conductor-backed case is $t = 0.25\lambda_0$. $N = 41$ piecewise sinusoids were used to represent the slot voltage.

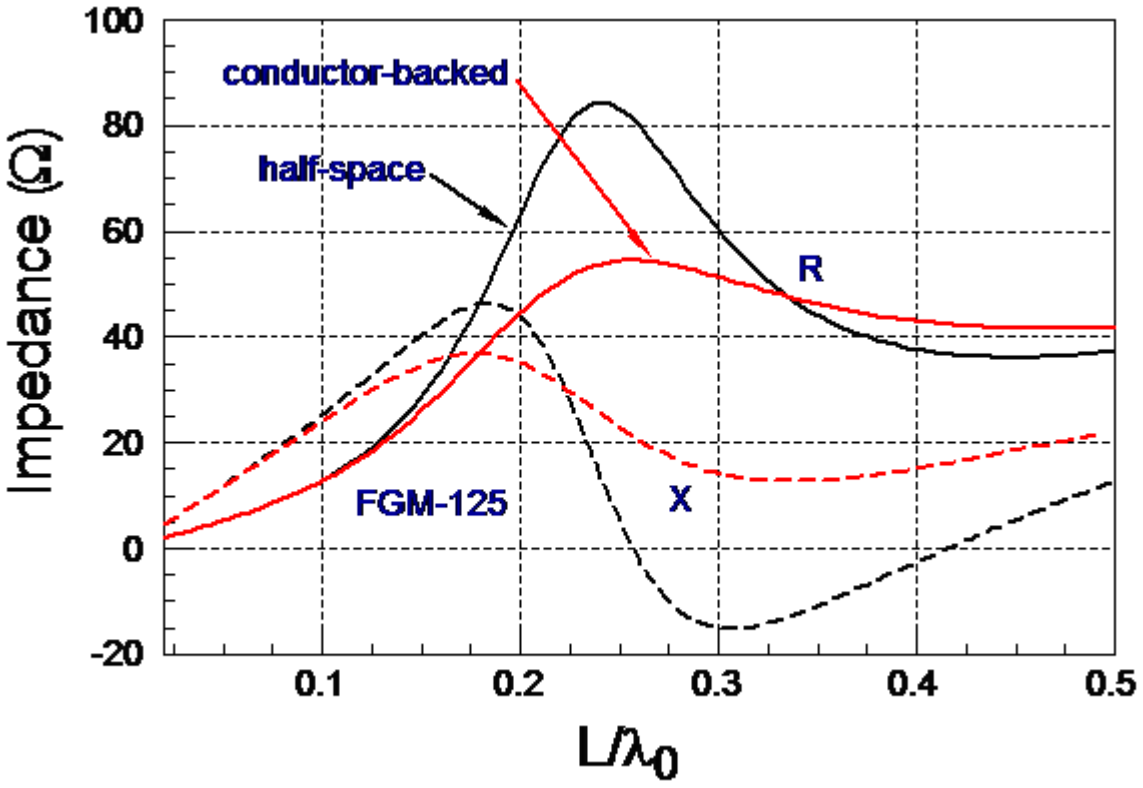

Figure 3.8: Input impedance of a slot antenna located in a conducting screen above a half space of FGM-125 with $\epsilon = (7.32 - j0.0464)\epsilon_0$ and $\mu = (0.576 - j0.484)\mu_0$ above a conductor-backed layer with the same properties. Slot length is L, slot width is $w = 0.002L$ and layer thickness for conductor-backed case is $t = 0.125$ inches. N = 41 piecewise sinusoids were used to represent the slot voltage.

3.5.2 Slot Antenna above Free Space Layer with Varying Thicknesses

The effect of the thickness of the material layer on the slot impedance is investigated by varying the thickness, t, of a material layer underneath a conducting screen with the material set as free space. This is compared to work published by Ostner [8]. The results, shown in Figure 3.9, are consistent with expectations. The antenna becomes shorted out as the ground plane is moved close to the slot. On the other hand, as the distance between the ground plane and the slot is increased, the radiation resistance rises until it even exceeds that of the unbacked case at about 0.3λ. This effect may be accounted for by ducting of energy away from the slot in the form of TEM guided wave modes [8]. This is possibly advantageous for material characterization since it is useful in interrogating the underlying material. There is good agreement between the results generated from the solution and Ostner's results although there are some slight discrepancies. It is possible that the differences can be accounted for by differences in the feed models and the computational techniques employed.

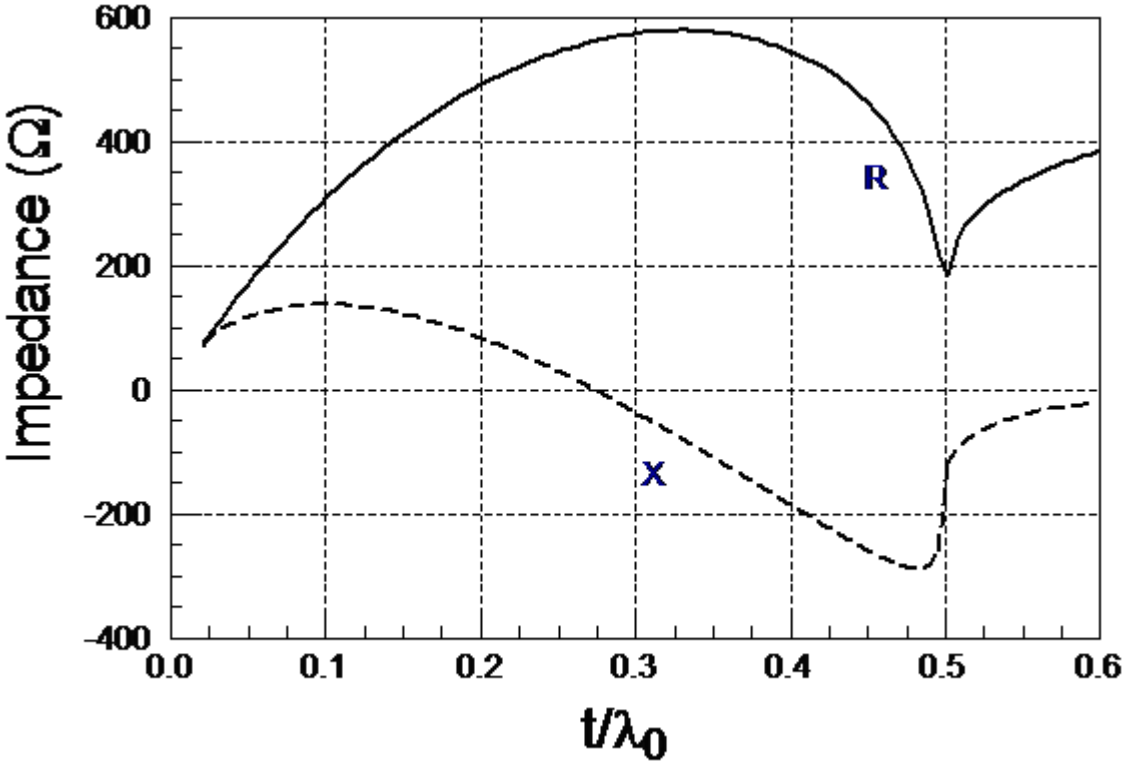

Figure 3.9: Input impedance of a slot antenna located in a conducting screen with a conducting plate located a distance t behind. The region between the slot and the plate is free space. The slot length is $L = 50$ mm and the slot width $isw = 1$ mm. N = 41 piecewise sinusoids were used to represent the voltage.

3.6 Summary

In this chapter, numerical results are given for solution of the MFIE presented in Chapter 2. The results have been shown to be consistent with theoretical expectations and have been validated against results published in the literature for slot antenna radiation. The material parameter extraction procedure is examined in detail in the next chapter.

BIBLIOGRAPHY

[1] I. S. Gradshteyn and I. M. Ryzhik. *Table of integrals, series, and products*. Elsevier/Academic Press, Amsterdam, seventh edition, 2007. Translated from the Russian, Translation edited and with a preface by Alan Jeffrey and Daniel Zwillinger.

[2] R. Harrington. Origin and development of the method of moments for field computation. *IEEE Antennas and Propagation Magazine*, 32(3):31–35, 1990.

[3] IMSL, Inc. *The IMSL libraries: FORTRAN subroutines for mathematics and statistics. Math/Library for mathematical applications, Stat/Library for statistical analysis, Sfun/ Library*. IMSL, Houston, TX, USA, 1989.

[4] Jacob Coetzee. Efficient spectraldomain analysis of open asymmetrical multiconductor transmission lines. *Microwave and Optical Technology Letters*, 8:206 – 209, 03 1995.

[5] Milton Abramowitz and Irene A. Stegun. *Handbook of Mathematical Functions with Formulas, Graphs, and Mathematical Tables*. Dover, New York, ninth dover printing, tenth gpo printing edition, 1964.

[6] George Arfken. *Mathematical Methods for Physicists*. Academic Press, Inc., San Diego, third edition, 1985.

[7] Constantine A Balanis. *Antenna theory: analysis and design*. Wiley-Interscience, 2005.

[8] H. Ostner and E.M. Biebl. Planar slot antennas backed by a ground plane. In *Proceedings of IEEE Antennas and Propagation Society International Symposium*, pages 612–615 vol.2, 1993.

[9] M. Kominami, D. Pozar, and D. Schaubert. Dipole and slot elements and arrays on semi-infinite substrates. *IEEE Transactions on Antennas and Propagation*, 33(6):600–607, 1985.

CHAPTER 4

Extraction of Material Parameters

4.1 Introduction

The feasibility of the extraction procedure for the proposed technique hinges on the assumption that the slot provides a perturbation that produces an observable difference between the conductor-backed measurement and the slotted conductor measurement. A measurement technique that provides "enough information" to extract ϵ and μ is desirable. In this chapter, investigations into whether the scattered field has sufficient dependence on the material parameters are presented. The specifics of the extraction procedure are also detailed in this chapter. First, there is a short discussion on peculiarities in calibration for this technique and the need for particular care in the calibration approach.

4.2 Considerations for Calibration

Consider a plane wave incident at an angle θ_0 on a slotted conductor above a conductor-backed material sample as shown in Figure 4.1. The following parameters are chosen: an incident angle $\theta_0 = 45$ degrees, a slot length $L = 20$ mm, a slot width $w = 1$ mm, a layer thickness $t = 0.125$ inches, a frequency of 2.88 GHz and an observation point 50 cm from the center of the slot. N = 100 piecewise sinusoids are used to represent the slot voltage in the Galerkin's method solution for the scattered field. An incident field strength of $E_0 = 1$ V/m is assumed. The sample is assumed to be MagRAM FGM-125 which has representative parameters $\epsilon_r = 7.319669 - j0.046408$ and $\mu_r = 0.575582 - j0.484231$. Figures 4.2 and 4.3 show the computed scattered field in amplitude and phase respectively vs. scattering angle θ measured from the normal to the slot for both FGM-125 and free-space [1]. For the dimensions considered here, the amplitude of the scattered field in both cases are quite close. The small size of the slot accounts for this. The phase values, on the other hand, are markedly different.

Calibration is required before the implementation of the proposed technique and performance of measurements on the conductor-backed material. In free-space measurement

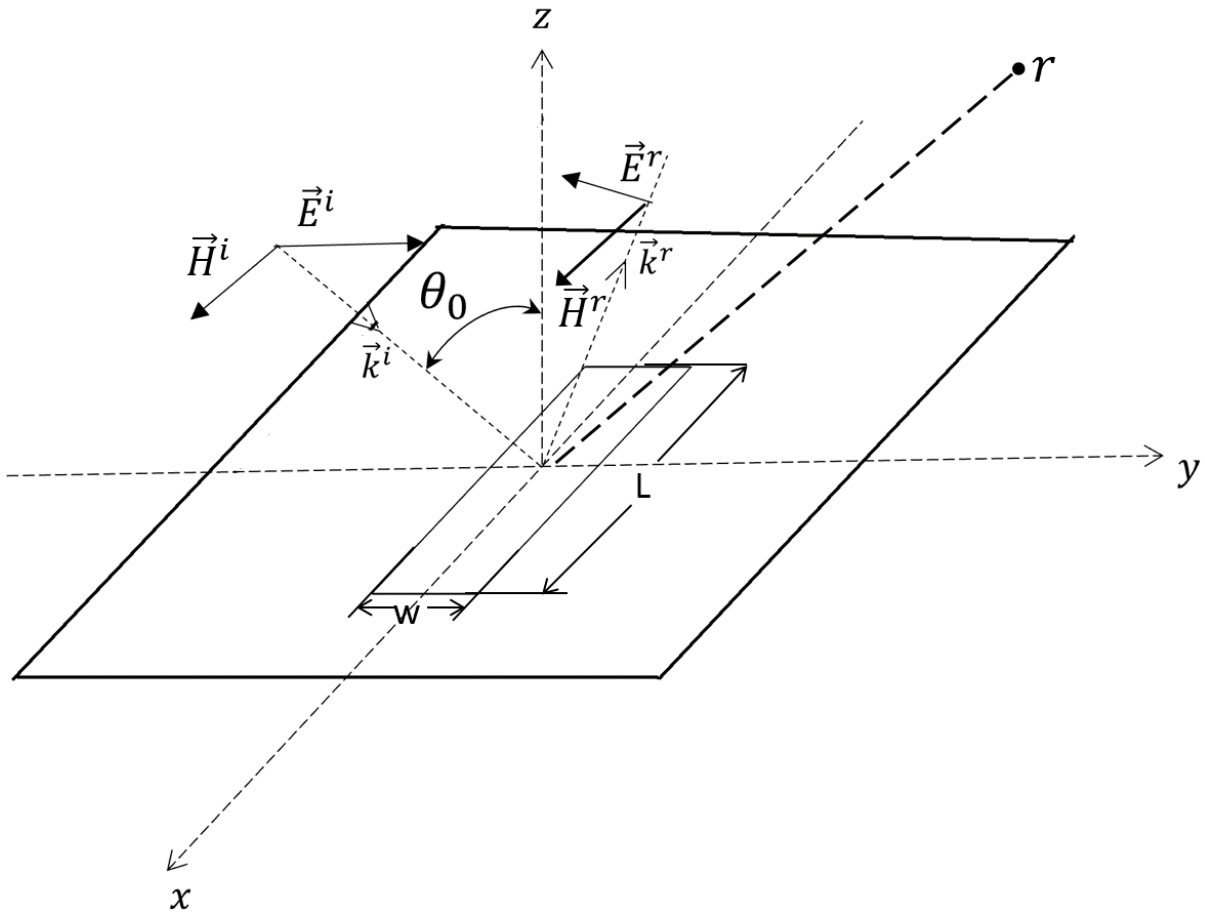

Figure 4.1: Figure showing plane wave incidence on slotted conductor surface.

techniques, it is typical to carry out calibration using a conducting plate [2]. However, such an approach is not applicable here because the field incident on a shorting plate is only reflected in the specular direction. This specular reflection makes it unfeasible to measure the response in the backscatter direction. An alternative approach involves calibration against a slotted conductor in free-space. This is achieved by computing the ratio between the scattered field amplitude for a slot above a conductor backed layer of material and the scattered field for a slot in a conductor in free space. Figures 4.4 and 4.5 show the computed scattered ratios in amplitude and phase for the same slot dimensions and parameters above for FGM-125 and free-space. The figures show that the ratios remains fairly flat despite changes in the scattering angle. This implies that there is some flexibility in the choice of the incident

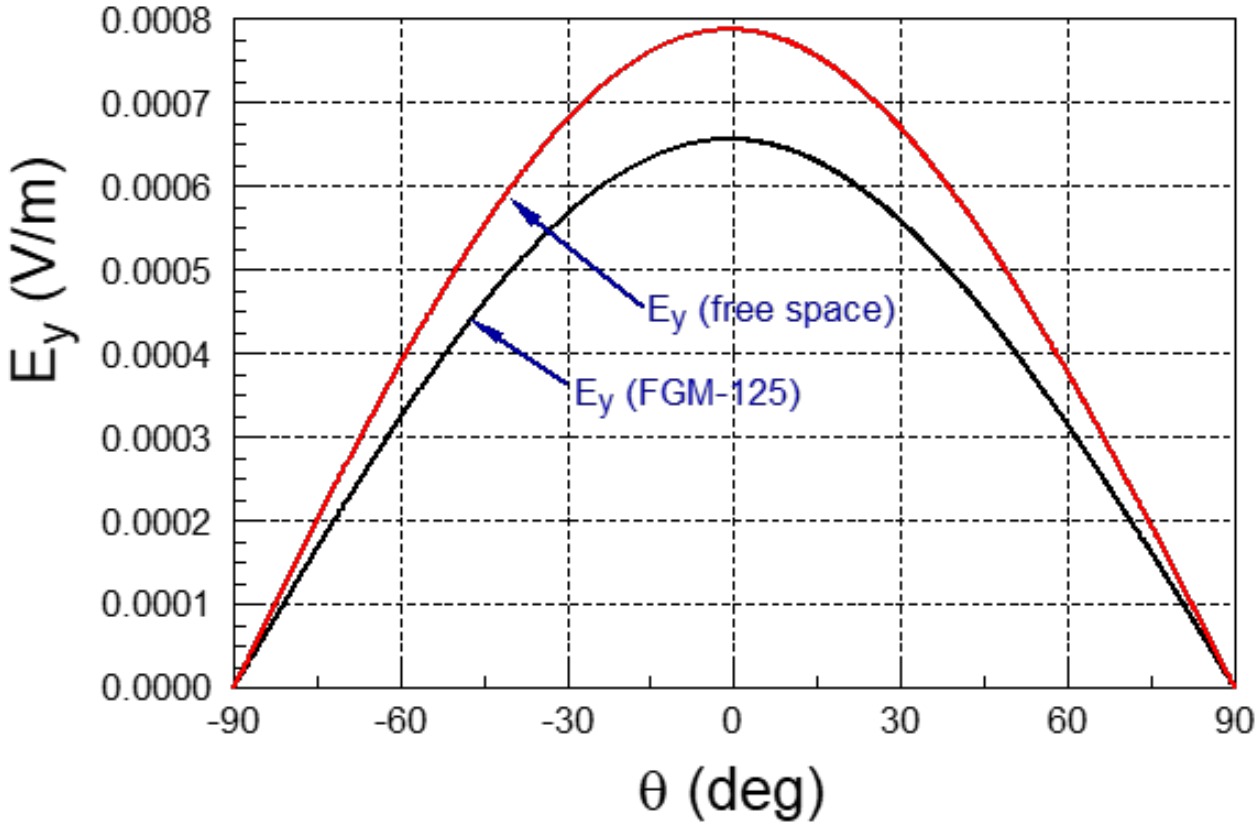

Figure 4.2: Scattered field amplitude for a slot above a conductor-backed layer of FGM-125 and for a slot in a screen immersed in free space. Incident field strength is 1 V/m. Incident field angle is $\theta_0 = 45^\circ$. Slot length is $L = 20$ mm , slot width is $w = 1$ mm, and layer thickness for conductor-backed case is $t = 0.125$ in. $N = 100$ piecewise sinusoids were used to represent the slot voltage. Observation distance is $R = 50$ cm and frequency is $f = 2.88$ GHz.

angle. However, it may be desirable to avoid choosing the specular angle because of the dominance of the specular reflection at that angle. Angles close to grazing should also be avoided because of the weakened signal strength and diffraction effects. An incident angle close to $\theta_0 = 45^\circ$ is chosen and an observation angle at $\theta = 45^\circ$ is similarly chosen.

4.3 Effect of ϵ and μ Variation on the Scattered Field

The viability of the proposed technique can be assessed by varying notional values of ϵ and μ and observing what effect the variations have on the scattered field. Figures 4.4 and 4.5 show results obtained when both ϵ and μ are varied by 10%. As can be observed, there is a reduction in the scattered ratio of about 5 dB and an increase in the phase of about

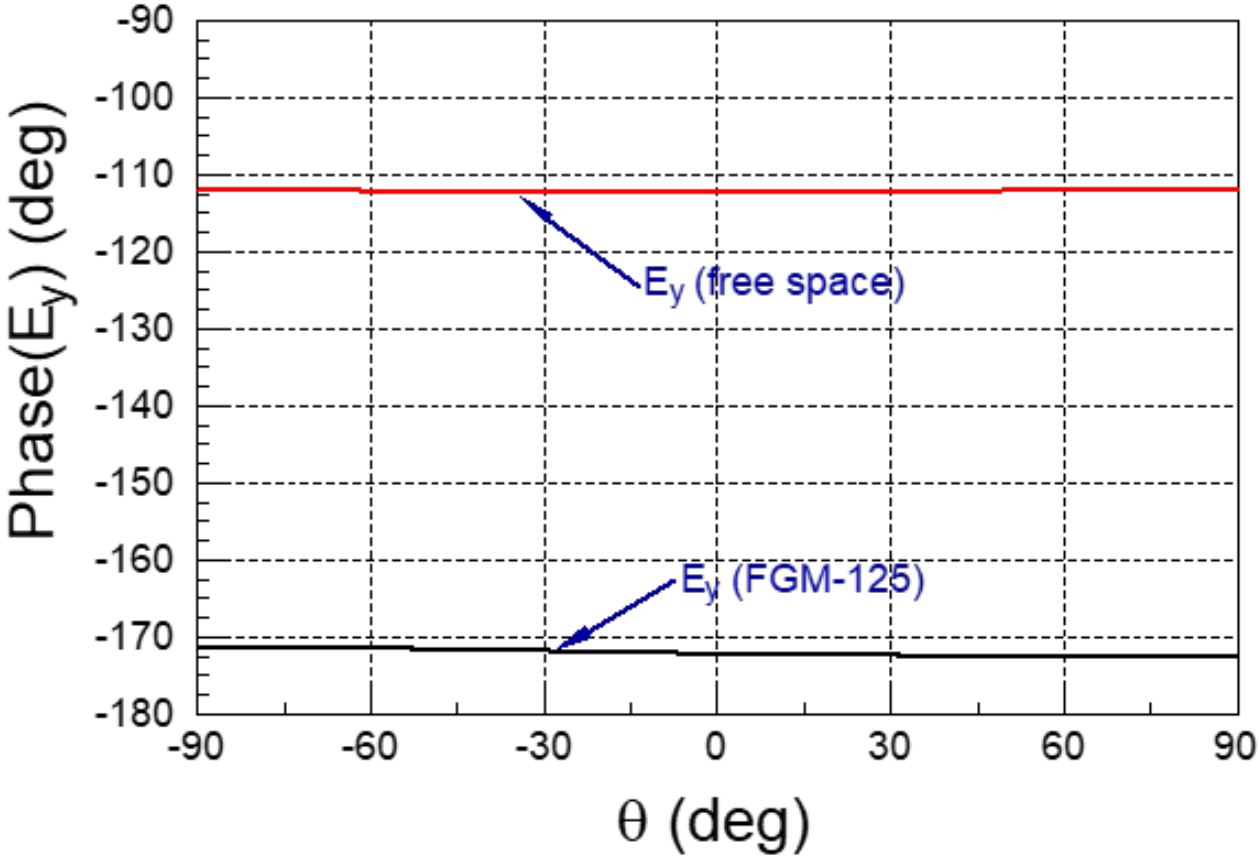

Figure 4.3: Scattered field phase for a slot above a conductor-backed layer of FGM-125 and for a slot in a screen immersed in free space. Incident field strength is 1 V/m. Incident field angle is $\theta_0 = 45^\circ$. Slot length is $L = 20$ mm , slot width is $w = 1$ mm, and layer thickness for conductor-backed case is $t = 0.125$ in. $N = 100$ piecewise sinusoids were used to represent the slot voltage. Observation distance is $R = 50$ cm and frequency is $f = 2.88$ GHz.

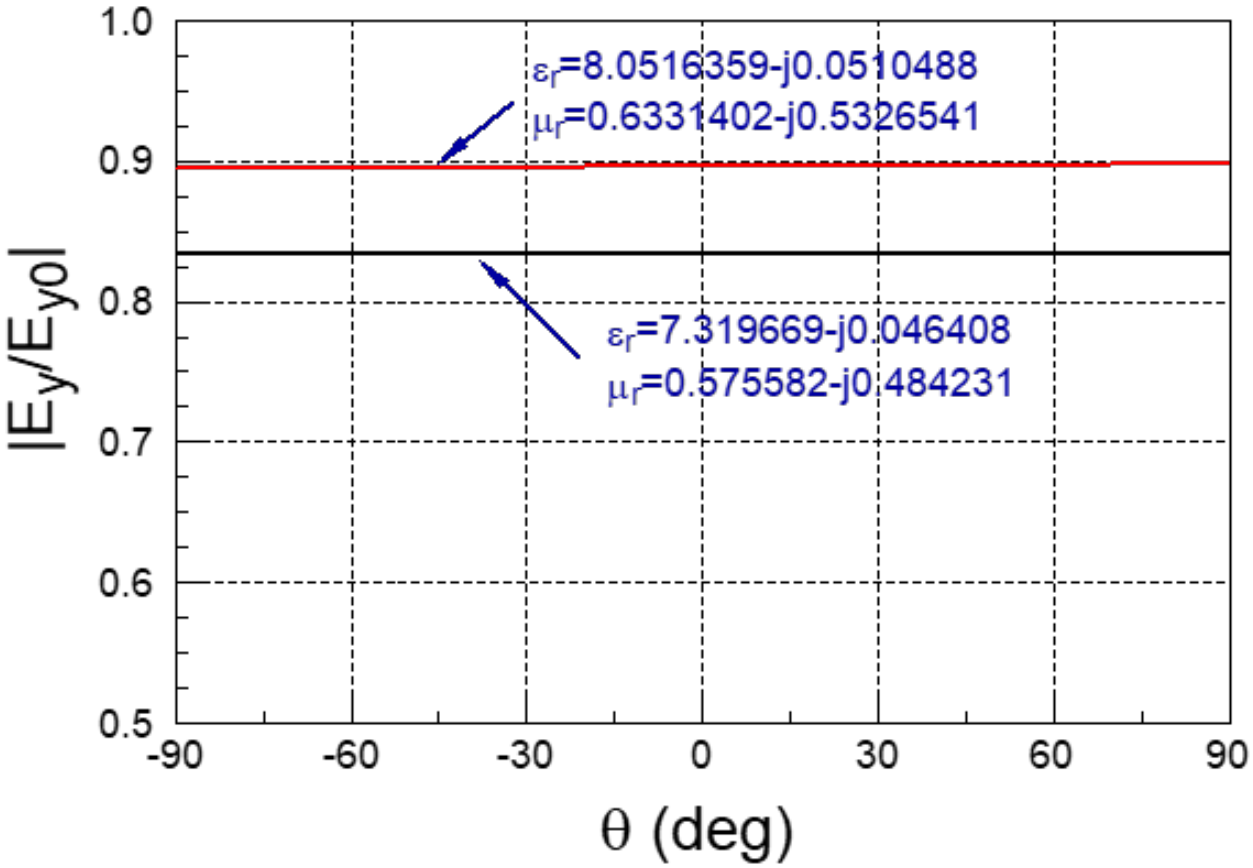

Figure 4.4: Ratio of scattered field amplitudes for a slot above a conductor-backed layer of FGM-125 to the scattered field for a slot in a screen immersed in free space. Incident field strength is 1 V/m. Incident field angle is $\theta_0 = 45^\circ$. Slot length is $L = 20$ mm, slot width is $w = 1$ mm, and layer thickness for conductor-backed case is $t = 0.125$ in. $N = 100$ piecewise sinusoids were used to represent the slot voltage. Observation distance is $r = 50$ cm and frequency is $f = 2.88$ GHz.

4.5°. These are measurable changes that suggest that the proposed technique is viable for extracting the constitutive parameters of a material sample.

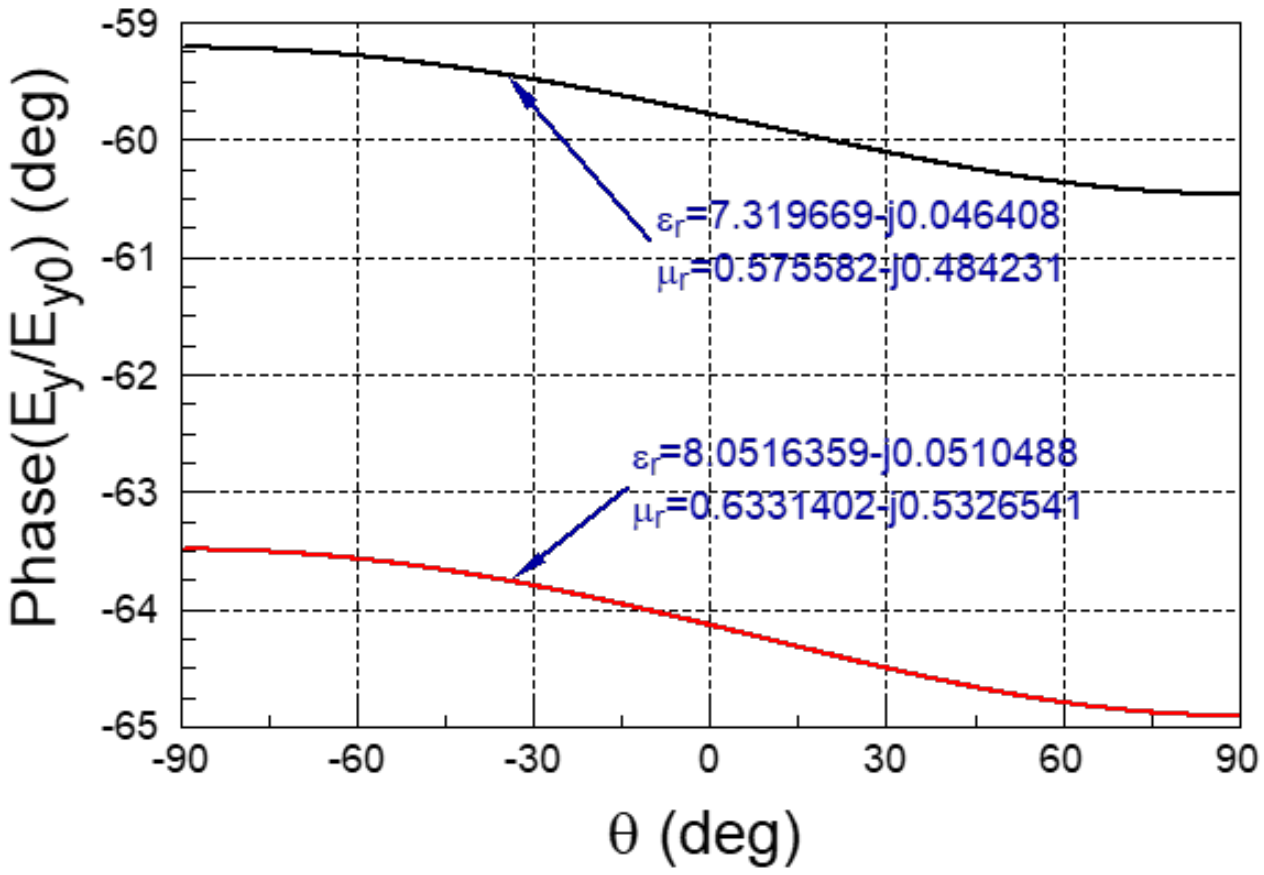

Figure 4.5: Ratio of scattered field phases for a slot above a conductor-backed layer of FGM-125 to the scattered field for a slot in a screen immersed in free space. Incident field strength is 1 V/m. Incident field angle is $\theta_0 = 45^\circ$. Slot length is $L = 20$ mm, slot width is $w = 1$ mm, and layer thickness for conductor-backed case is $t = 0.125$ in. $N = 100$ piecewise sinusoids were used to represent the slot voltage. Observation distance is $r = 50$ cm and frequency is $f = 2.88$ GHz.

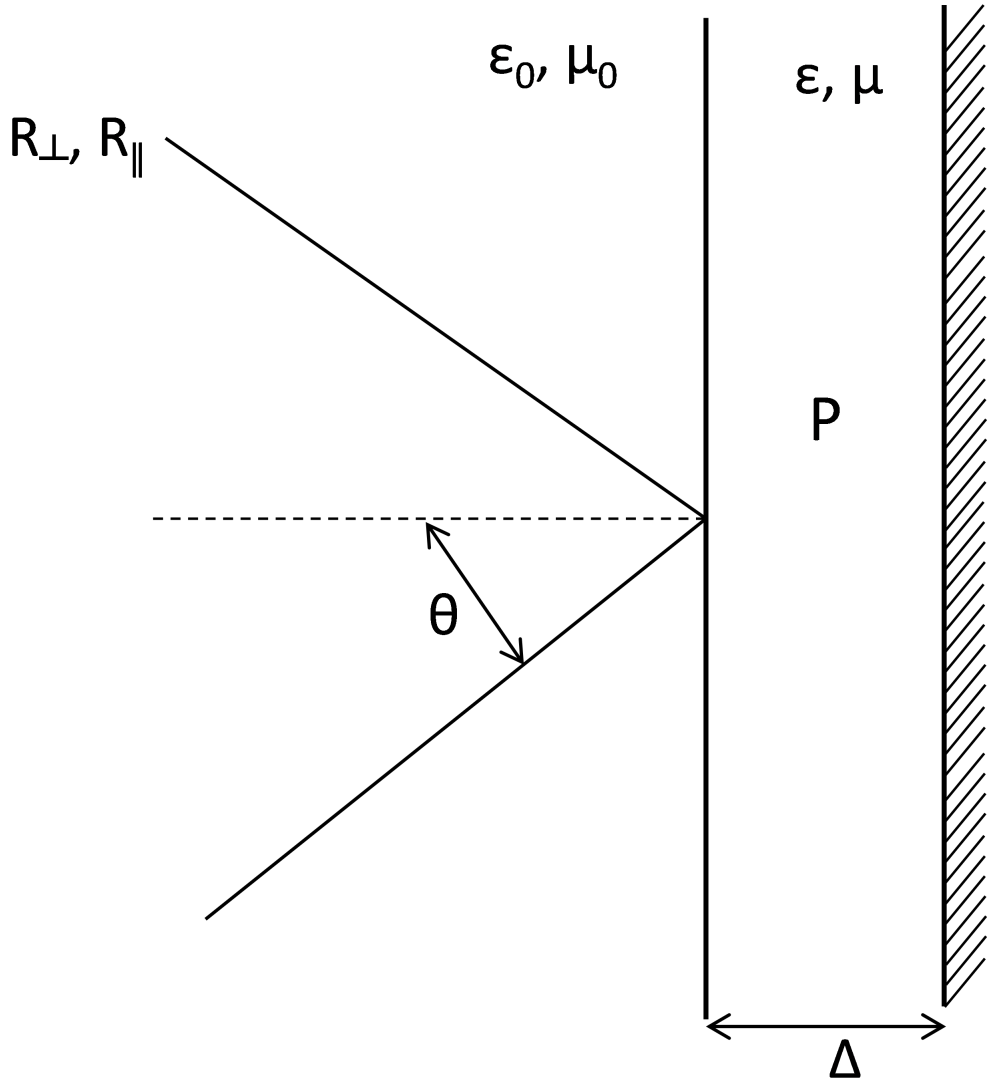

Figure 4.6: Plane wave incident on a conductor-backed material sample.

4.4 Constitutive Parameter Extraction

4.4.1 Extracting ϵ and μ from S-Parameter Measurements

Consider Figure 4.6 where a plane wave is incident on a conductor-backed layer of material. The propagation factor P is given by

$$P = e^{-jk_z\Delta}, \tag{4.1}$$

where $k_z^2 = k_0^2 - k^2 \sin^2\theta$ with $k^2 = \omega^2\mu\epsilon$. The global reflection coefficient can be expressed for perpendicular and parallel polarization as

$$R_\perp = \frac{\Gamma_\perp - P^2}{1 - \Gamma_\perp P^2}, \tag{4.2}$$

and

$$R_\parallel = \frac{\Gamma_\parallel - P^2}{1 - \Gamma_\parallel P^2}, \tag{4.3}$$

respectively. Here, the perpendicular interfacial reflection coefficient $\Gamma_\perp$ is given by

$$\Gamma_\perp = \frac{Z_\perp - Z_{0\perp}}{Z_\perp + Z_{0\perp}} \tag{4.4}$$

where

$$Z_\perp = \frac{k\eta}{k_z} \tag{4.5}$$

is the wave impedance in the material region while

$$Z_{0\perp} = \frac{\eta_0}{\cos\theta} \tag{4.6}$$

is the wave impedance in free space. Here, $\eta = \sqrt{\mu\epsilon}$ is the intrinsic impedance of the medium and $\eta_0 = \sqrt{\mu_0\epsilon_0}$ is the intrinsic impedance of free space. Similarly, the parallel interfacial reflection coefficient is given by

$$\Gamma_\parallel = \frac{Z_\parallel - Z_{0\parallel}}{Z_\parallel + Z_{0\parallel}} \tag{4.7}$$

where

$$Z_{\parallel} = \frac{k_z \eta}{k} \tag{4.8}$$

is the wave impedance for parallel polarization within the material and

$$Z_{0\parallel} = \eta_0 \cos\theta \tag{4.9}$$

is the free-space wave impedance. Substituting (4.5) and (4.6) into (4.4) gives

$$\Gamma_{\perp} = \frac{k\eta\cos\theta - k_z\eta_0}{k\eta\cos\theta + k_z\eta_0} \tag{4.10}$$

while substituting (4.8) and (4.9) into (4.7) gives

$$\Gamma_{\parallel} = \frac{k_z\eta - k\eta_0\cos\theta}{k_z\eta + k\eta_0\cos\theta}. \tag{4.11}$$

In order to extract ϵ and μ, two distinct measurements are required: 1) a reflection measurement of a conductor-backed material without a slot, and 2) a reflection measurement of a conductor-baked material with a slot. The two different reflection measurements are denoted by S_{11}^{o} and S_{11}^{s} respectively. For the first measurement scenario, the global reflection coefficient can be expressed as

$$S_{11}^{o} = \frac{\Gamma^{o} - P^2}{1 - \Gamma^{o}P^2}, \tag{4.12}$$

from (4.12), Γ^{o} can be determined as

$$\Gamma^{o} = \frac{S_{11}^{o} + P^2}{1 + S_{11}^{o}P^2}. \tag{4.13}$$

This demonstrates that the interfacial reflection coefficient can be computed from the mea-

sured global reflection coefficient.

Consider the case of perpendicular polarization. The expression in (4.10) can be rearranged to give

$$\frac{\eta}{\eta_0} = \frac{1+\Gamma_\perp}{1-\Gamma_\perp}\frac{k_z}{k\cos\theta}. \tag{4.14}$$

Similarly for the case of parallel polarization, (4.11) can be rearranged so that

$$\frac{\eta}{\eta_0} = \frac{1+\Gamma_\parallel}{1-\Gamma_\parallel}\frac{k\cos\theta}{k_z}. \tag{4.15}$$

Since $\eta/\eta_0 = \sqrt{\mu_r/\epsilon_r}$, the ratio of the permeability and permittivity can be computed if S_{11}^o is measured. Recalling from $k^2 = \omega^2\mu\epsilon$ and $k_z^2 = k_0^2 - k^2\sin\theta$ that only products of ϵ_r and μ_r appear in k and k_z, the ratio μ/ϵ_r can be written in terms of measured S-parameters and the product $\mu_r\epsilon_r$. The theoretical expressions for the scattered field in the second measurement scenario (with the slot present) are also functions of ratios and products of ϵ_r and μ_r. The computed ratios can be substituted so that only the product remains unknown. Defining a relative wave number $k_r = k/k_0$, S_{11}^o can be used to eliminate $\eta_r = \eta/\eta_0$ and $\mu_r = k_r\eta_r$. This leaves the complex permittivity, ϵ_r, as the only remaining unknown. It can be determined by solving the equation

$$S_{11}^T(k_r) - S_{11}^s = 0 \tag{4.16}$$

where S_{11}^s is the measured reflection coefficient with the slot in place as mentioned earlier and $S_{11}^T(k_r)$ is the theoretical global reflection coefficient with the slot in place. Once k_r is found the complex permittivity and permeability can be computed from $\epsilon = k_r/\eta_r$ and $\mu = k_r\eta_r$ respectively. As will be discussed in the next chapter, the equation in (4.16) is solved by utilizing a root solver.

4.5 Summary

In this chapter, special calibration considerations that arise due to the nature of the proposed slotted conductor technique have been highlighted. Based on results presented, the technique appears to be able to capture changes in the complex constitutive parameters. Additionally, the extraction approach following S-parameter measurements has been described in detail. In the next chapter, sensitivity of the extraction procedure is considered and verified.

BIBLIOGRAPHY

[1] K.J. Vinoy and R.M. Jha. *Radar Absorbing Materials: From Theory to Design and Characterization*. Springer US, 1996.

[2] Philip G. Bartley and Shelley B. Begley. A new free-space calibration technique for materials measurement. In *2012 IEEE International Instrumentation and Measurement Technology Conference Proceedings*, pages 47–51, 2012.

CHAPTER 5

Aperture Optimization

5.1 Introduction

Before an experimental implementation of the proposed technique was undertaken, investigations were carried out to understand the robustness of the technique. The sections that follow detail error analysis performed to assess the sensitivity of the technique to uncertainties in the values of the measured S-parameters. Following that, assessments of the performance of aperture screen technique are presented. Finally, optimizations on the aperture screen parameters are carried out. This is important as the aperture screen design must be carefully chosen to facilitate the extraction process. Ultimately, there is a need to identify optimal slot parameter combinations that ensure that the constitutive parameters are accurately extracted when the aperture screen technique is implemented in the field.

5.2 Inversion Problem Solution

As covered in the previous chapter, the material constitutive parameters (ϵ and μ) can be extracted by solving the transcendental equation

$$S_{11}^{T}(k_r) - S_{11}^{s} = 0. \tag{5.1}$$

Here, S_{11}^{s} is the measured reflection with the aperture screen in place and $S_{11}^{T}(k_r)$ is the theoretical global reflection coefficient with the screen in place. S_{11}^{T} is obtained by taking the ratio between the theoretical scattered field with the aperture screen in place, E_y, and the incident field amplitude, E_0. The equation in (5.1) can be solved by utilizing a root search approach. However, a solution may be difficult to obtain in the presence of noise or measurement error when using the root search approach.

A solution can alternatively be found by minimizing the following error

$$E = \left| S_{11}^{T}(k_r) - S_{11}^{s} \right|^2 . = 0. \tag{5.2}$$

An inversion code was written in MATLAB for implementing the minimization. A solution is found given a set of design parameters that is, for a given aperture length and width the complex permittivity and permeability of a material are extracted. The forward problem is implemented by making calls to an executable generated after compiling Fortran code for the numerical solutions. The hybrid MATLAB-Fortran approach makes it possible for the forward problem to be computed quickly while allowing for access to the various solvers available in MATLAB for the minimization. Newton's method is used to perform the minimization. The code is validated by "going around in a circle." S parameters are generated for assumed values of ϵ and μ using the forward problem and then inserted into the inverse problem to get back the original values of the constitutive parameters.

Error Analysis Parameters	
Frequency, f (GHz)	2.88
Slot length, l (mm)	20
Slot width, w (mm)	1
Material thickness, t (mm)	3.175
Incidence Angle ($^{\circ}$)	90
Observation Angle ($^{\circ}$)	90
Observation Distance (mm)	500

Table 5.1: Parameters utilized for Error Analysis.

5.3 Error Analysis

In order to assess the robustness of the proposed technique, the material extraction can be tested by investigating the sensitivity of the resulting extracted constitutive parameters to uncertainties in the S-parameter measurement. Two approaches were explored for this sensitivity analysis, namely the Monte Carlo method and the standard error propagation method. The aim of this analysis is to provide some insight into how noise propagates through the inversion process. For a non-robust technique, the error would be greatly amplified. Unless otherwise stated, the parameters shown in Figure 5.1 are considered for the error analysis in the later sections. The Monte Carlo method and the standard error propagation method are discussed briefly before delving into the error analysis results.

5.3.1 Monte Carlo Method

The Monte Carlo method is the primary approach considered for the error analysis because of its simplicity and the insight it provides into the statistical behavior of processes. Monte-Carlo analysis is used for assessing the viability of processes with the with evaluation of a large number of tests. Example of scenarios where Monte Carlo type analyses have been employed with great success include design of robots, tuning of antennas, design of mechanical fixtures and optimization of chemical plants [1].

In general, Monte-Carlo analyses find application in situations where the execution of multiple experiments is not physically feasible or may be exorbitantly expensive. The ability to carry out multiple simulations in relatively quick fashion may be more practical. This

makes it possible to assess the behavior of processes in ways that would have been impossible before widespread improvements and access to computational resources allowed for the running of a great number of numerical tests [1]. For the purposes here, Monte Carlo simulation provides insight into the robustness of the proposed technique. The simulations are carried out by perturbing S-parameter measurements with Gaussian noise and observing the propagation of error through the extraction process.

5.3.2 Standard Error Propagation Method

The standard error propagation method is implemented as an alternative to the Monte Carlo Method. The error propagation method involves the computation of derivatives and provides the advantage of quicker computation [2]. The mathematical details of the approach are covered in Appendix 7.1. In implementing this approach, the Cauchy-Reimann equations can also be leveraged to reduce the number of required computations. The S-parameters can be expressed in polar form as $S = Ae^{j\phi}$ where A is the amplitude and ϕ is the phase, thus

$$\frac{\partial \epsilon_r''}{\partial \phi} = A\frac{\partial \epsilon_r'}{\partial A} \tag{5.3}$$

and

$$\frac{\partial \epsilon_r'}{\partial \phi} = -A\frac{\partial \epsilon_r''}{\partial A}. \tag{5.4}$$

Since the complex permittivity and permittivity are extracted from the inversion procedure, only one derivative needs to be computed with respect to the amplitude for complex ϵ and another for complex μ. The derivatives with respect to the phase can be obtained from the Cauchy-Reimann relations in (5.3) and (5.4).

5.3.3 Monte Carlo Simulation Results

A 125 mil thick conductor-backed layer of FGM-125 with constitutive parameters $\epsilon_r = 7.319099 - j0.046408$ and $\mu_r = 0.575582 - j0.484231$ is considered at 2.88 GHz. The forward problem for a layer without the aperture screen is used to obtain the reflection S-parameter

for the case of normal incidence. The forward problem for a layer with the aperture screen (dimensions: 20 mm by 1 mm) in place is also used to obtain reflection S-parameters for the normal incidence case. As covered in the previous chapter, in practice it is disadvantageous to chose the specular angle as the observation angle due to the dominance of the specular reflection. However, from the numerical calculations the scattered field can be computed as a standalone quantity so this problem is avoided here.

Random Gaussian noise is added to the reflection S-parameters. The noise parameters are chosen to correspond to worst-case uncertainty values for an Agilent 8510C network analyzer which are 0.02 dB in amplitude and 1° in phase [3]. The noisy S-parameters generated are taken as "measured" data from which ϵ and μ are extracted. The extraction process is performed $N = 100$ times and the resulting statistics are generated. The standard deviation of the extracted parameters corresponds to the propagated error. It should be noted that a larger value for N leads to greater confidence in the statistical distribution obtained. The standard deviation obtained for ϵ is $0.136 + j0.357$ while that for μ is $0.0155 + j0.0361$. These values correspond to 2%, 3% and 7% errors in ϵ', μ' and μ'', respectively. There is a very large value in the error of ϵ'' but this is likely attributable to the fact that the extracted value is very small and cannot be properly captured by the proposed technique. In Figures 5.1 through 5.4, histograms showing the real and imaginary parts of the extracted parameters are presented. Although a larger choice for the value N will lead to even more statistically meaningful results, the results show that the extracted results form a Gaussian-like distribution as expected. Examining the mean values of ϵ and μ ($7.30 - j0.253$ and $0.561 - j0.500$ respectively) reveal that they are close to their nominal values but suggests the need for a larger number of trials.

The appropriate number of trials for the analysis is determined by plotting the extracted parameters against increasing values of N. The results which are presented in Figures 5.5 through 5.8 show the errors in the constitutive parameters normalized against their nominal values. It can be seen that the results become fairly stable beyond N = 500 trials. Since

these results are normalized, they also represent an estimate of the percent error in the extracted parameters due to VNA uncertainty. It can be seen that the real and imaginary part of μ exhibit about a 5% and 7% error respectively while the real part of ϵ exhibits error of about 3%. The imaginary part of ϵ experiences an extremely large error of 1300% which, as mentioned earlier, is due to the very small nominal value.

5.3.3.1 Comparison against Two-Thickness Techniques

The results obtained for the propagated error using the aperture technique seem quite promising. However, it is important to compare these results against another material extraction technique to properly assess the performance of the proposed technique. The two-thickness method is considered for this comparison. It is chosen since it is also a reflection-only technique involving the presence of a conductor backing as is the case with the proposed technique. The two-thickness technique is described in detail in [4]. A similar Monte Carlo error analysis is carried out using the two thickness method and the ratios of the standard deviations of the constitutive parameters generated from the aperture technique and the two-thickness are computed and plotted.

The resulting ratios are shown in Figures 5.9 through 5.12 for ϵ', ϵ'', μ' and μ''. A ratio less than unity indicates that the proposed technique performs better then the two-thickness method. This is the case for all four constitutive parameters. The results thus demonstrate that the proposed technique is indeed promising for accurate extraction of the parameters. The two thicknesses considered for the two-thickness implementation are 125 mils and 250 mils (that is, one layer of FGM-125 for the first thickness and two layers of FGM-125 for the second thickness).

5.3.4 Monte Carlo-Standard Error Propagation Comparison

Table 5.2 shows results from a comparison of the Monte Carlo method and the error propagation method for the proposed technique. Again, a 3.175 mm thick layer of FGM 125 with the following parameters is used: slot length = 20 mm, slot width = 1 mm, frequency = 2.88 GHz, $\epsilon_r = 7.319099 - j0.046408$ and $\mu_r = 0.575582 - j0.484231$. The uncertainty in the

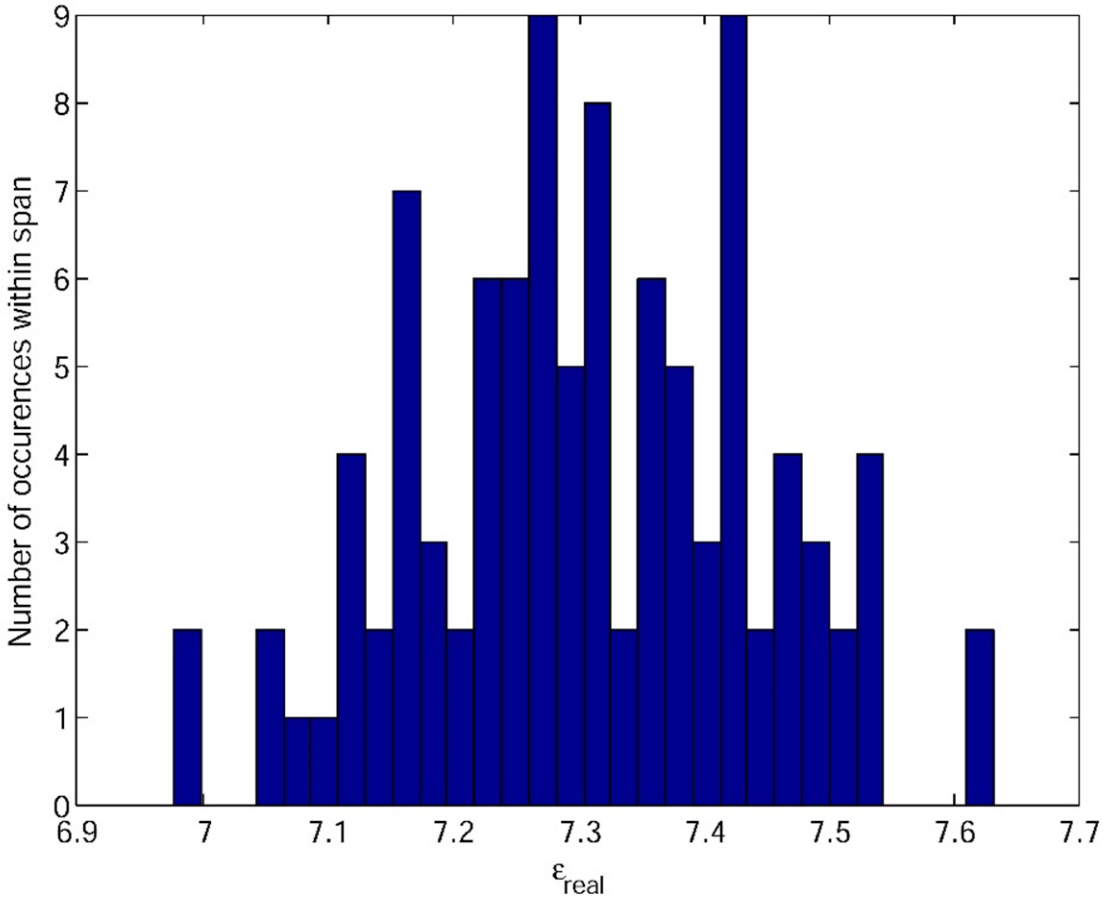

Figure 5.1: Real part of ϵ extracted from noisy data for $N = 100$ Monte Carlo trials.

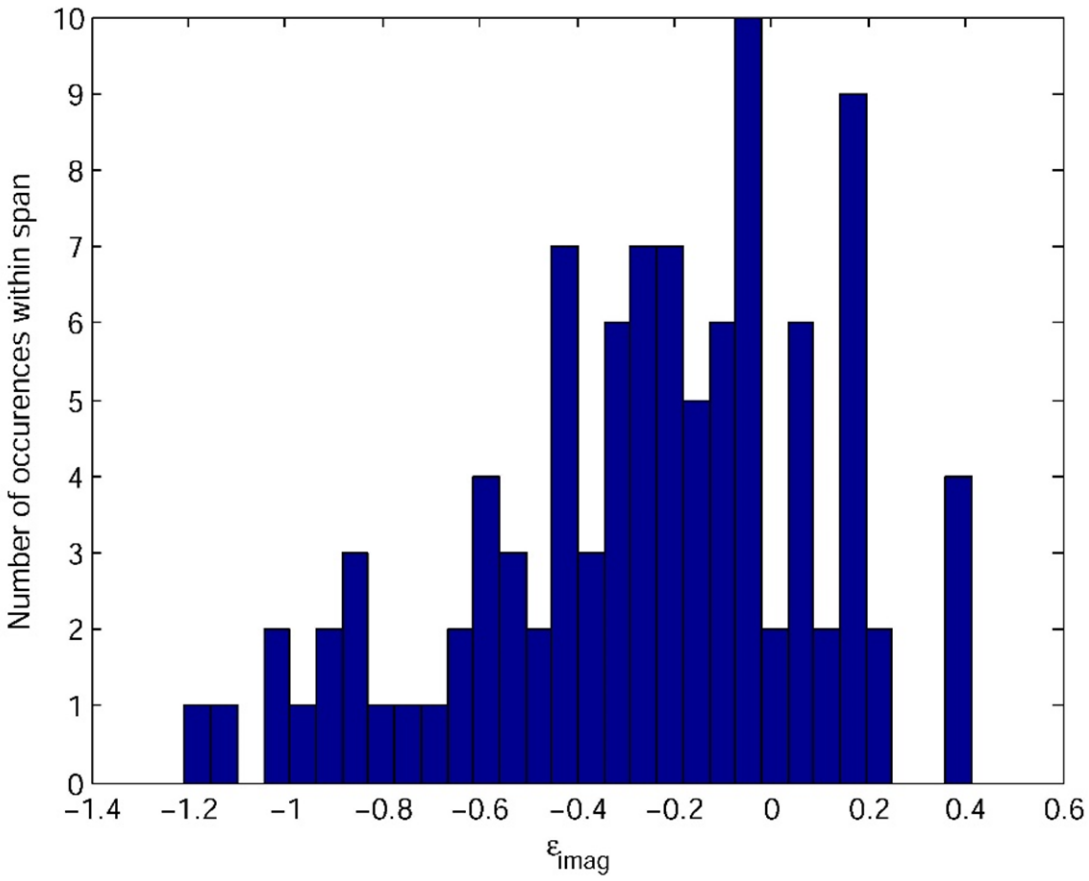

Figure 5.2: Imaginary part of ϵ extracted from noisy data for $N = 100$ Monte Carlo trials.

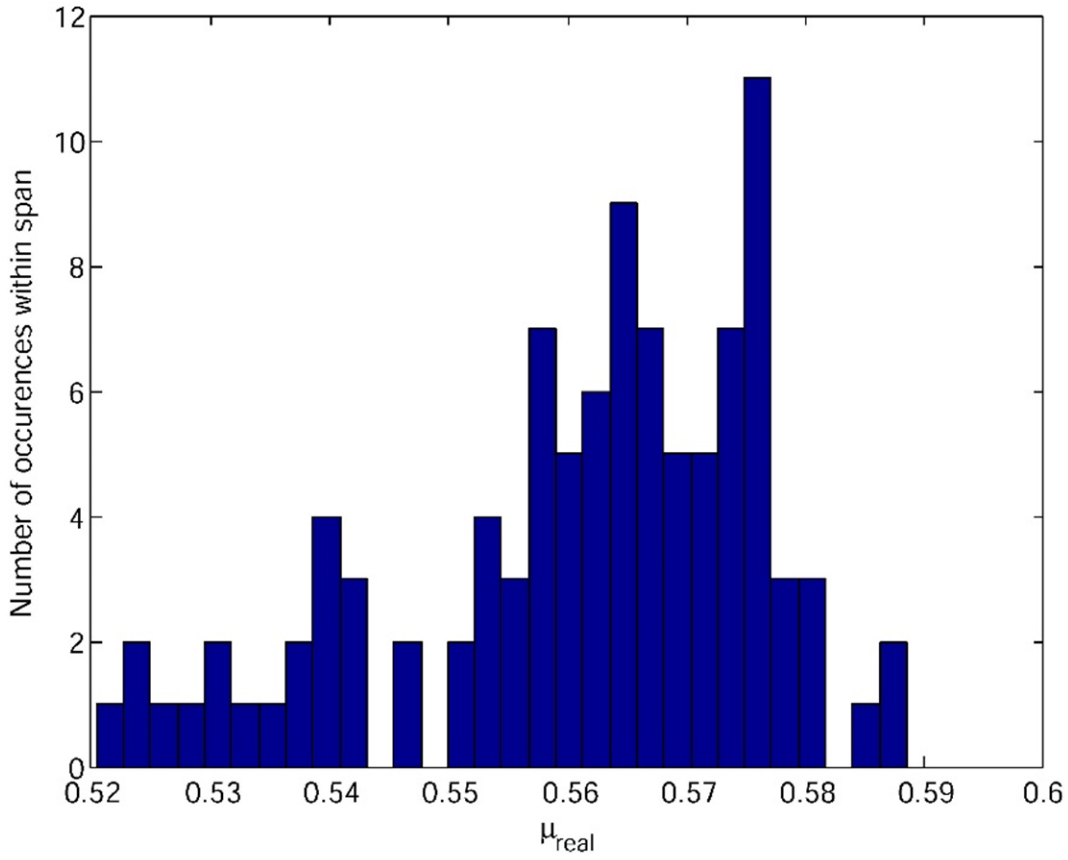

Figure 5.3: Real part of μ extracted from noisy data for $N = 100$ Monte Carlo trials.

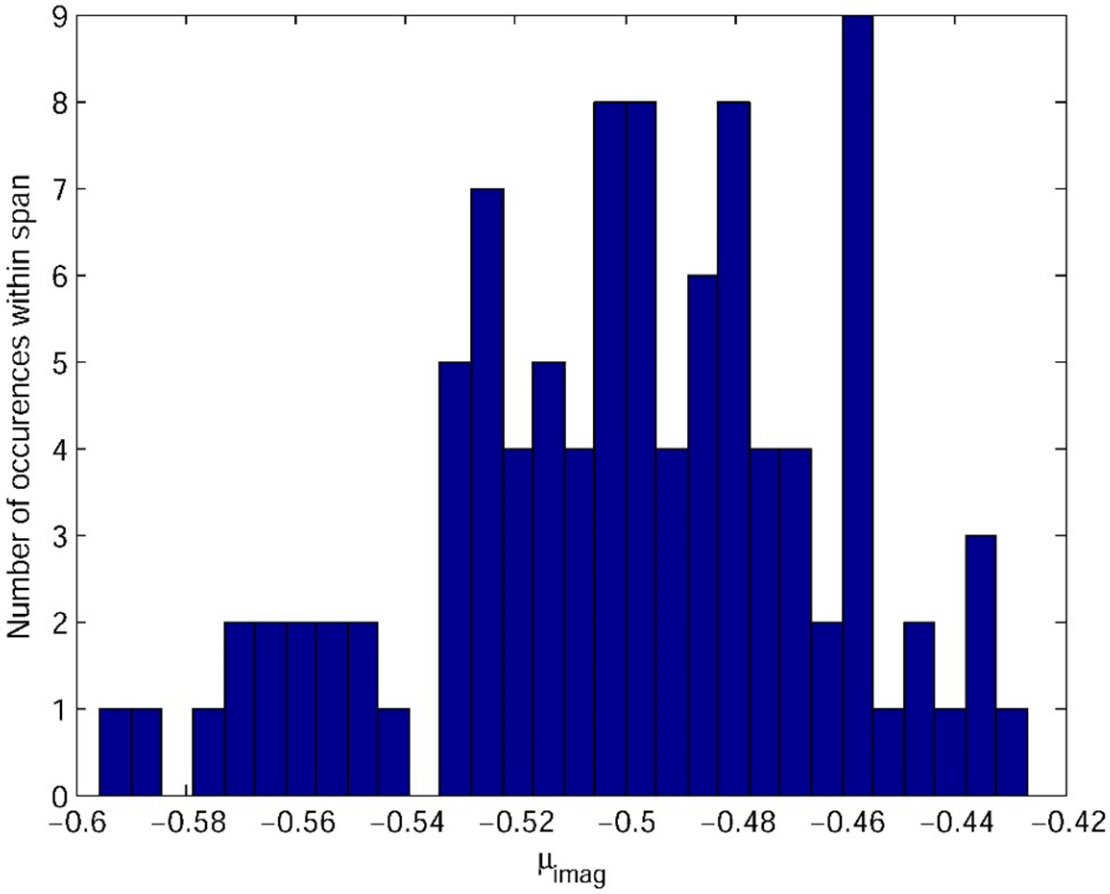

Figure 5.4: Imaginary part of μ extracted from noisy data for $N = 100$ Monte Carlo trials.

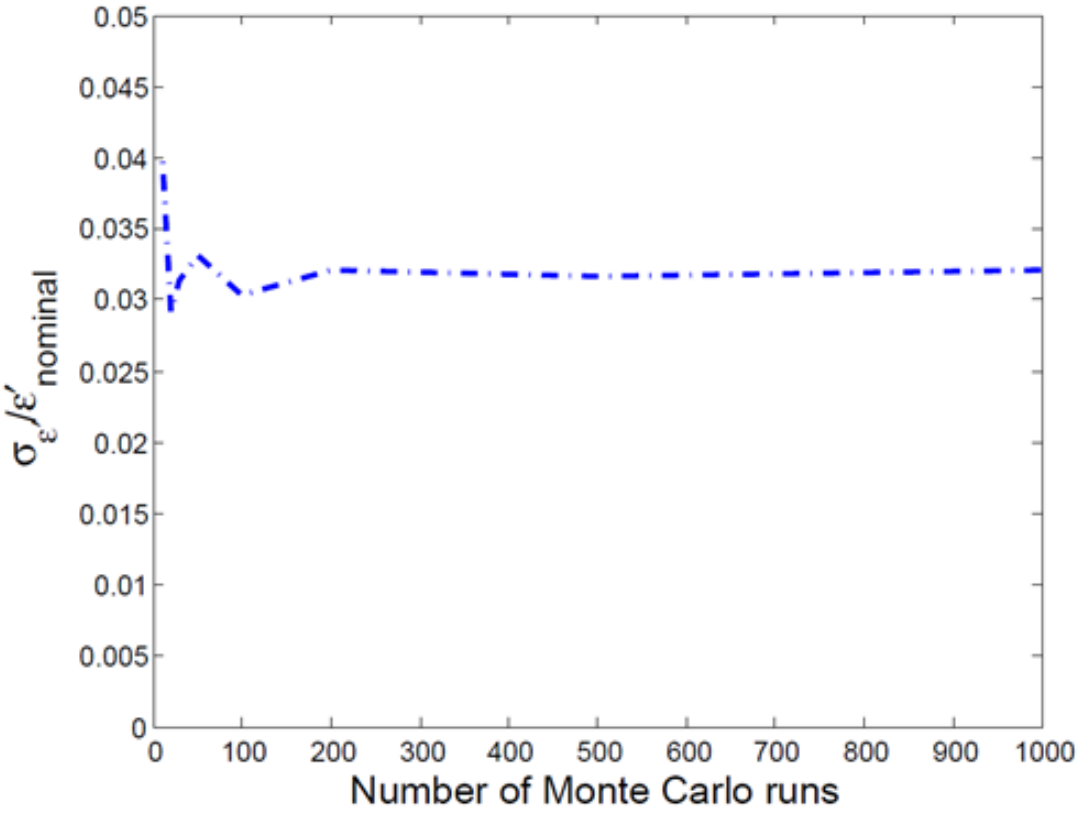

Figure 5.5: Error in the real part of ϵ normalized to the nominal value of the real part of ϵ, as a function of the number of Monte Carlo trials.

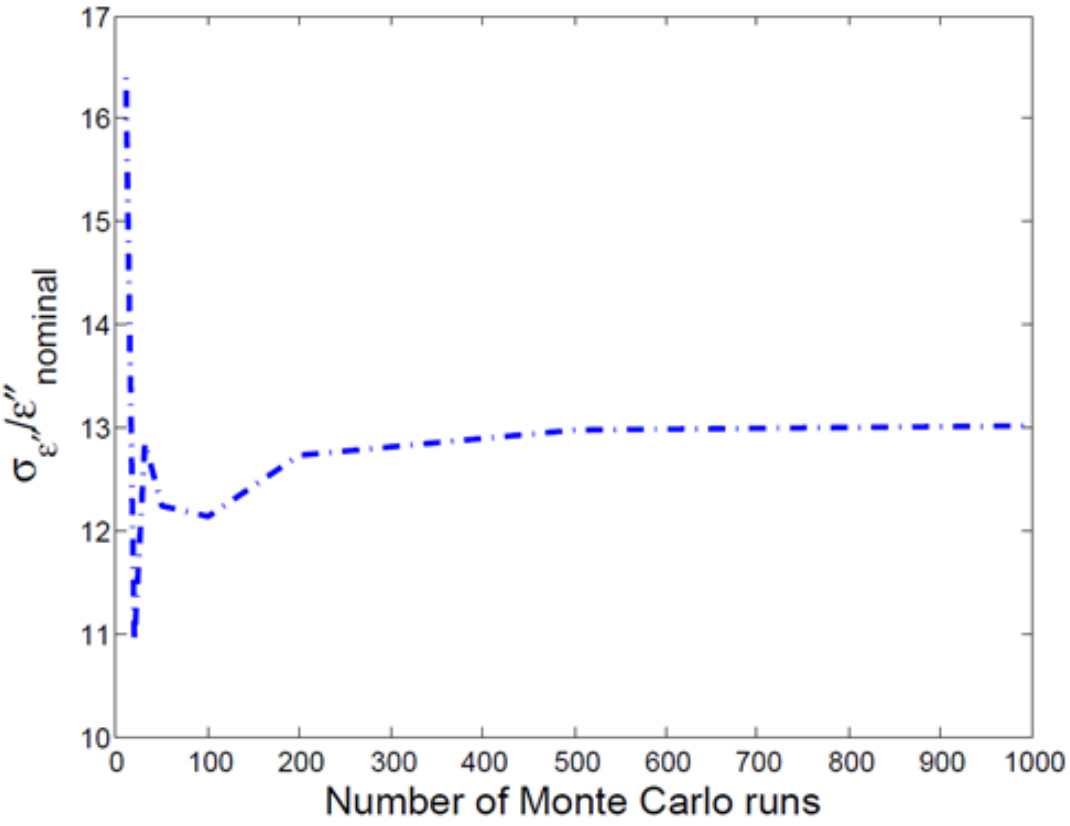

Figure 5.6: Error in the imaginary part of ϵ normalized to the nominal value of the imaginary part of ϵ, as a function of the number of Monte Carlo trials.

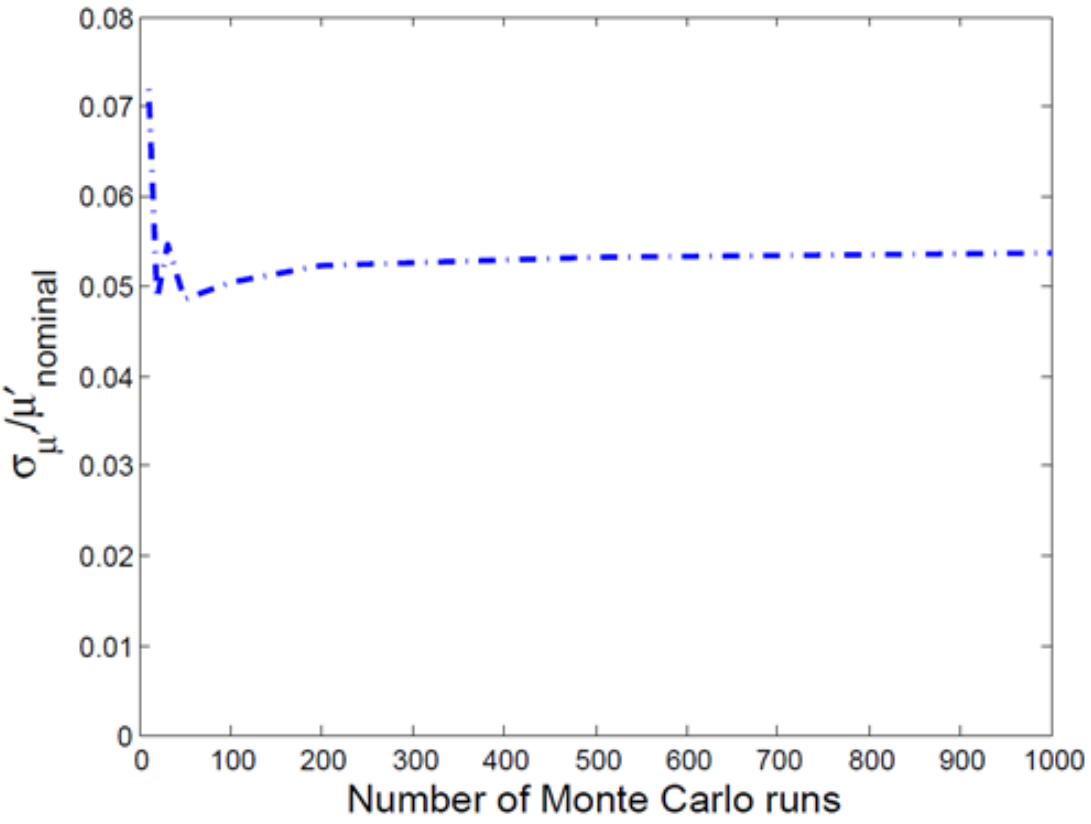

Figure 5.7: Error in the real part of μ normalized to the nominal value of the real part of μ, as a function of the number of Monte Carlo trials.

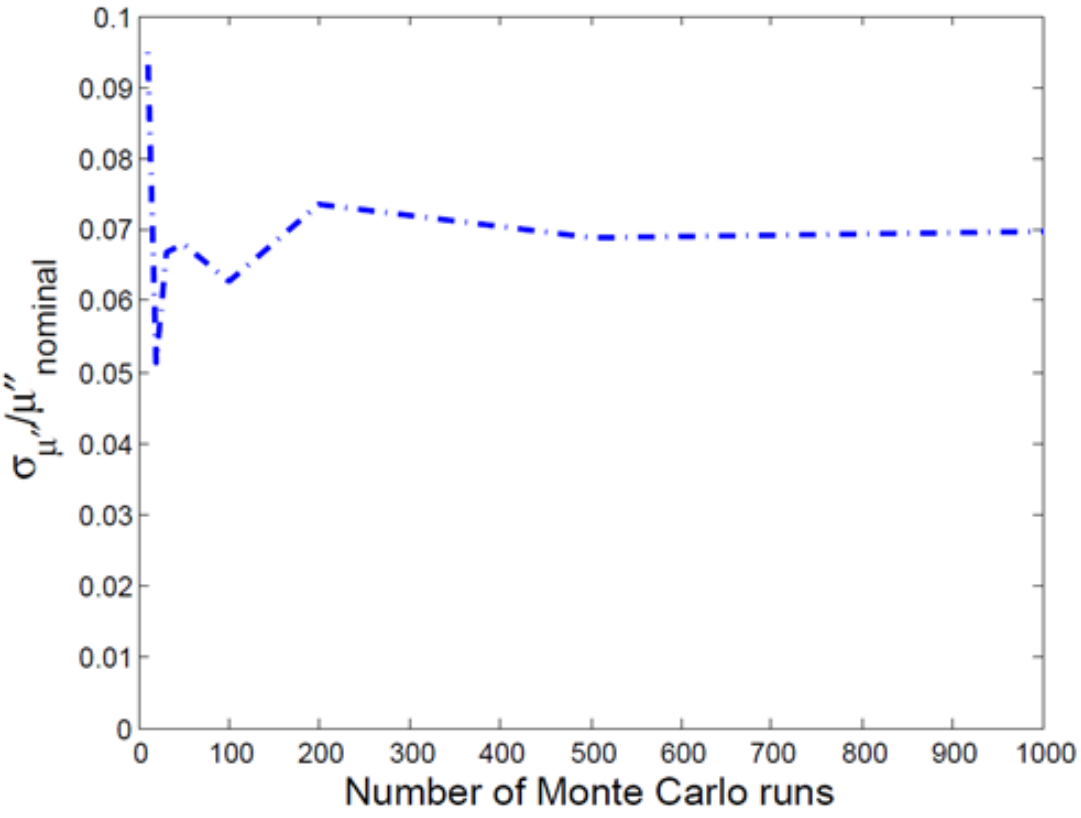

Figure 5.8: Error in the imaginary part of μ normalized to the nominal value of the real part of μ, as a function of the number of Monte Carlo trials.

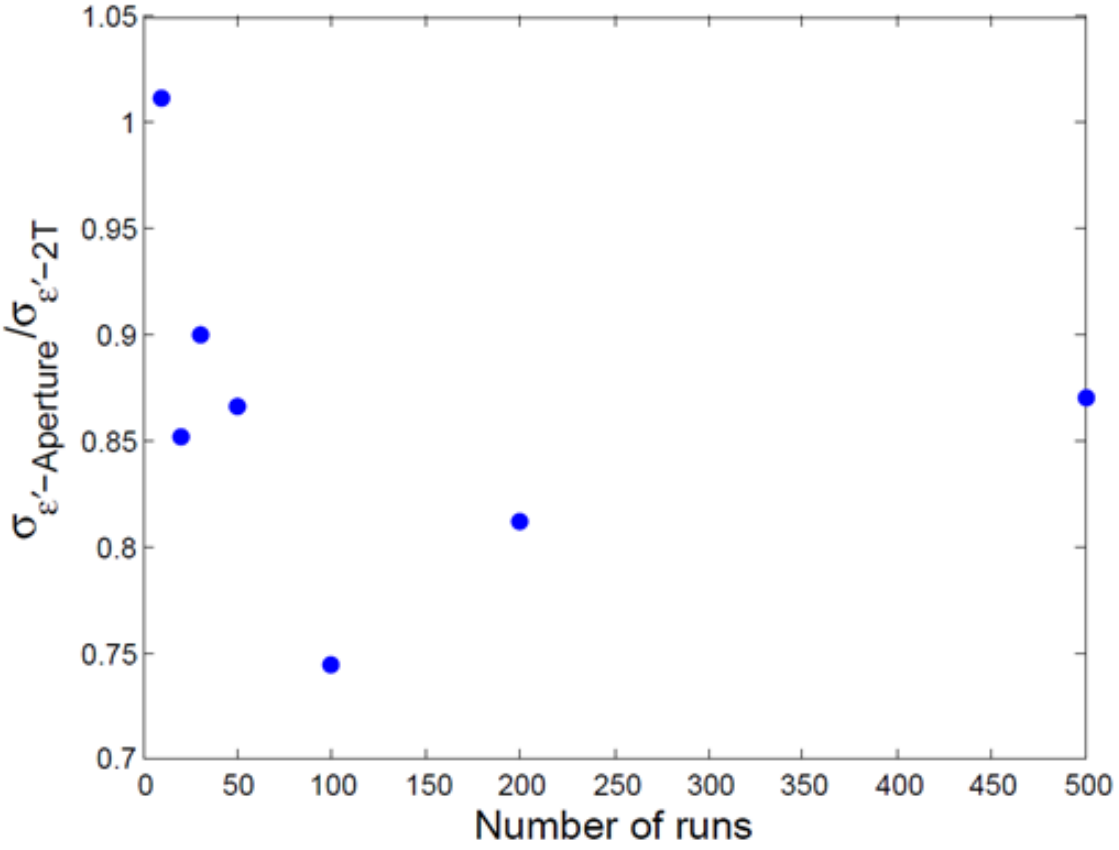

Figure 5.9: Ratio of the error in the real part of ϵ extracted using the aperture method to the error in the real part of ϵ extracted using the two thickness method.

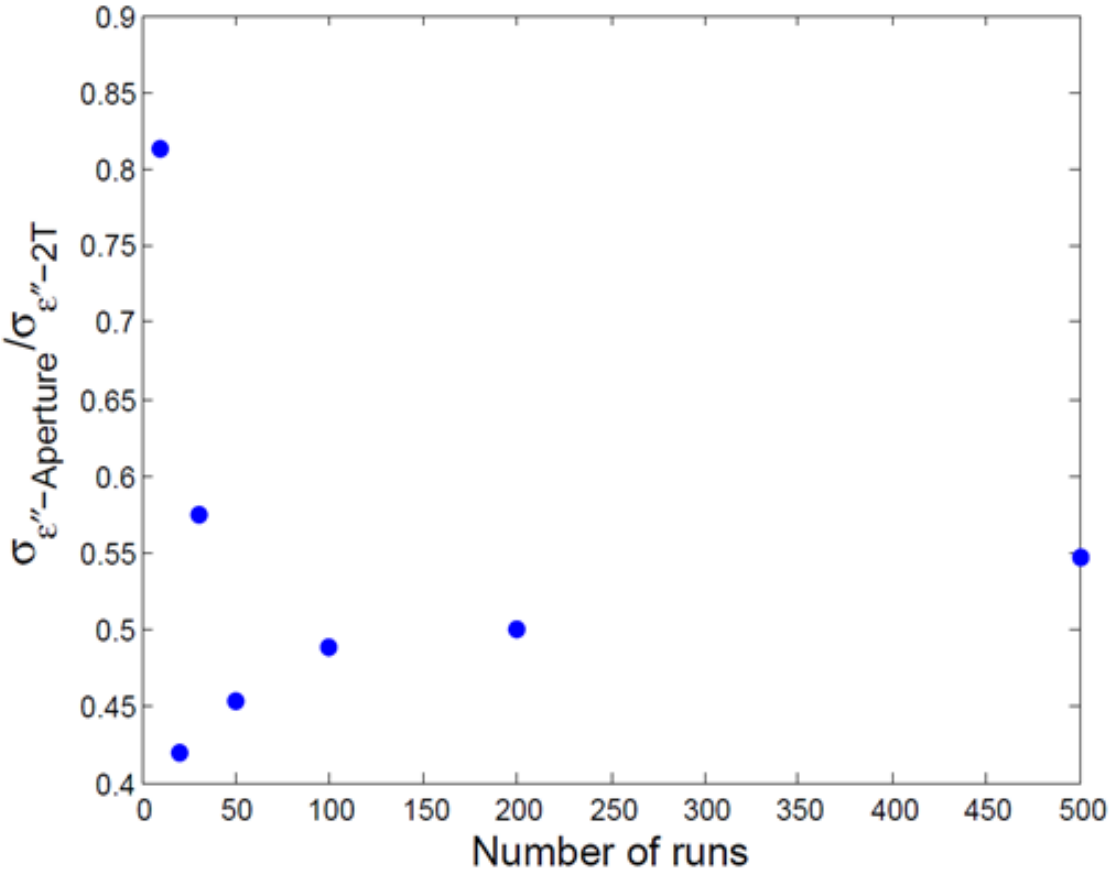

Figure 5.10: Ratio of the error in the imaginary part of ϵ extracted using the aperture method to the error in the imaginary part of ϵ extracted using the two thickness method.

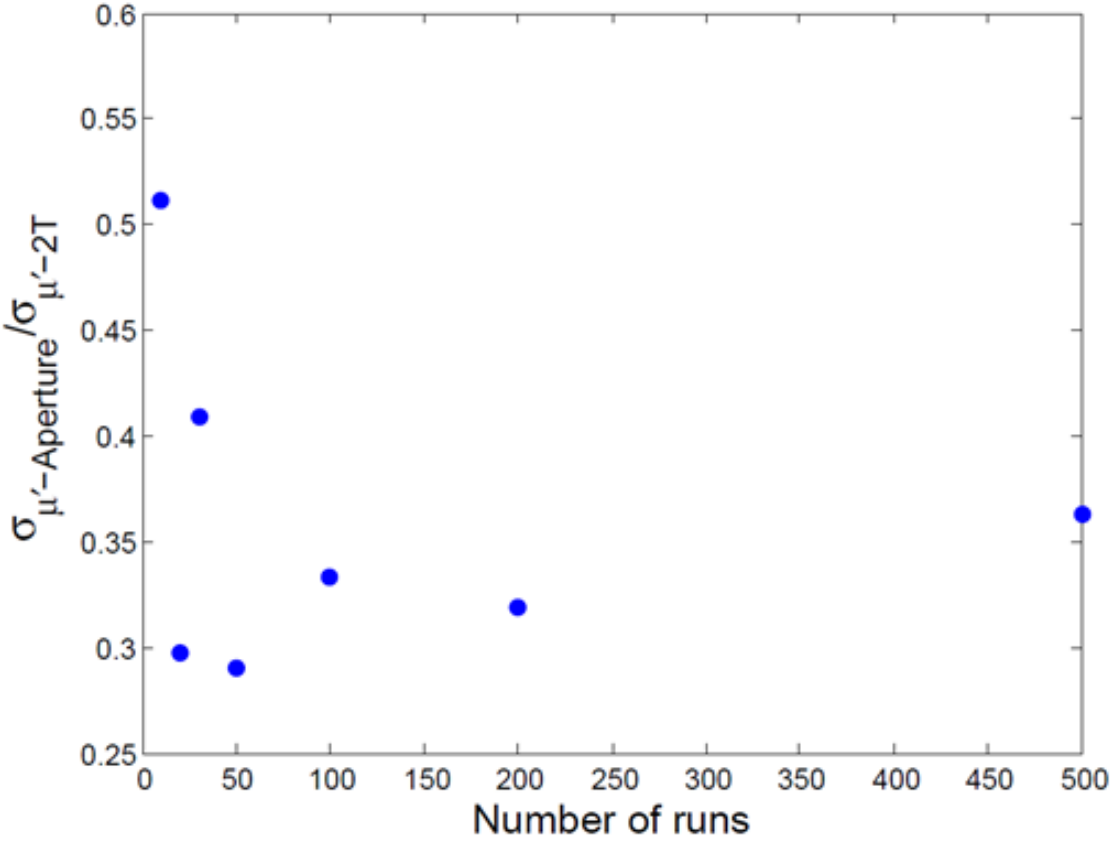

Figure 5.11: Ratio of the error in the real part of μ extracted using the aperture method to the error in the real part of μ extracted using the two thickness method.

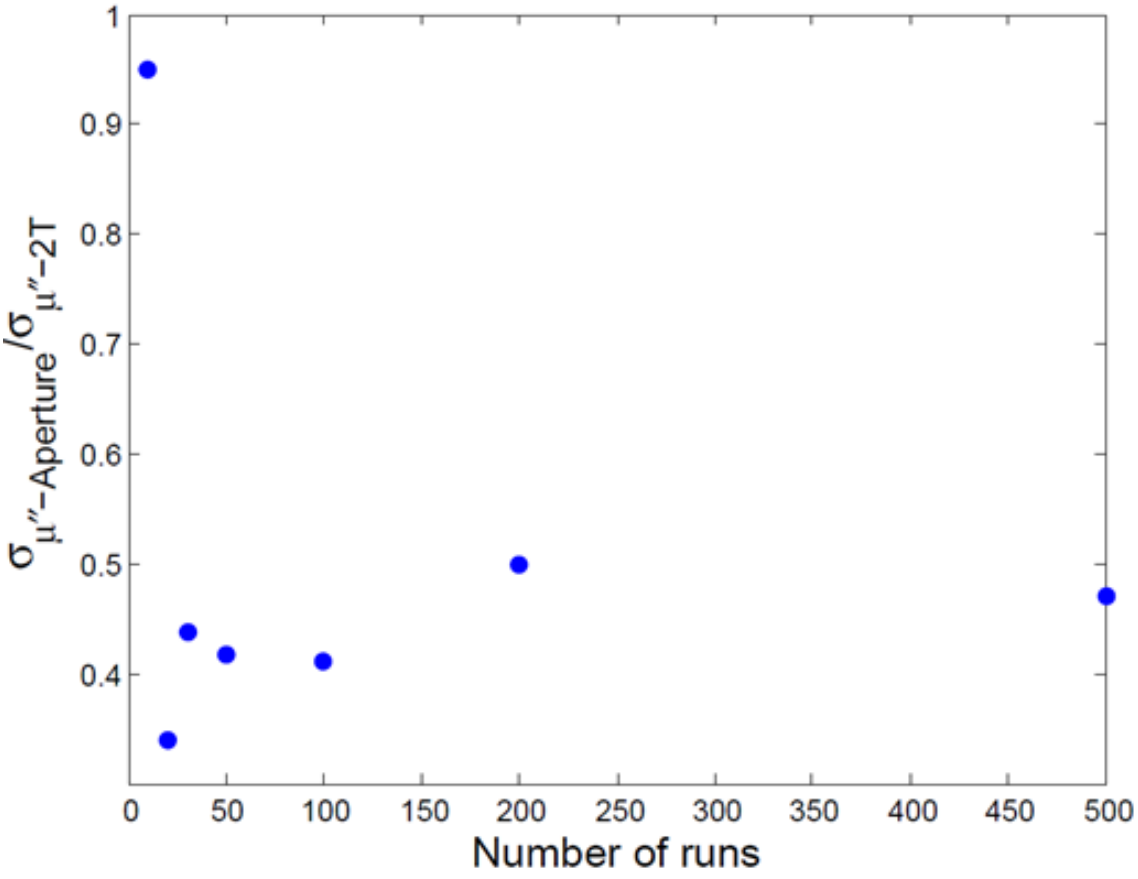

Figure 5.12: Ratio of the error in the imaginary part of μ extracted using the aperture method to the error in the real part of μ extracted using the two thickness method.

Nominal Values	μ Monte Carlo	σ Monte Carlo	σ Standard Error Propagation
$\mu_r' = 0.575582$	0.571117589435909	0.029018113230405	0.044402395382609
$\mu_r'' = 0.484231$	0.481316041647672	0.030315888555527	0.013964580830703
$\epsilon_r' = 7.319669$	7.310639156841075	0.221753603346064	0.326685227301673
$\epsilon_r'' = 0.046408$	0.051783551099407	0.563802891858627	0.283864841444781

Table 5.2: Comparison of Monte-Carlo and Standard Error Propagation Method.

S-parameters is assumed to be 0.02 dB in amplitude and 1° in phase. $N = 60$ trials were used for the number of trials in the Monte Carlo method. The excitation field was assumed to be a plane wave normally incident and polarized across the slot, and the scattered field was computed 500 mm from the center of the slot along an angle 45° from the normal. For both approaches, there are huge error values in the extraction of ϵ''. This is, however, not surprising since as stated earlier this technique is not well suited to the extraction of the very small values of the imaginary part of the permittivity.

5.4 Aperture Optimization

Several parameters including the dimension of the aperture, the direction and polarization of the incident wave, the distance and direction of observation must be carefully chosen in the design of the aperture screen. The observation angle is considered first. Monte Carlo simulations are performed to assess the effect of varying the observation angle with the other parameters set as follows: frequency = 2.88 GHz, slot length = 20 mm, slot width = 1 mm, material thickness = 3.175 mm and N = 500 runs. The observation angle is varied while normal incidence is assumed. The results obtained are shown in Figures 5.13 and 5.14. It should be immediately apparent that the results are not symmetric about zero. This is because for each Monte Carlo run a new set of random numbers are generated. As such, it not unexpected that the results are asymmetric. An observation angle of 45° is chosen since there does not appear to be a huge dependence on the observation angle. This angle is chosen and fixed for the other parameter investigations.

The slot dimensions are considered next. A Monte Carlo simulation is carried out with

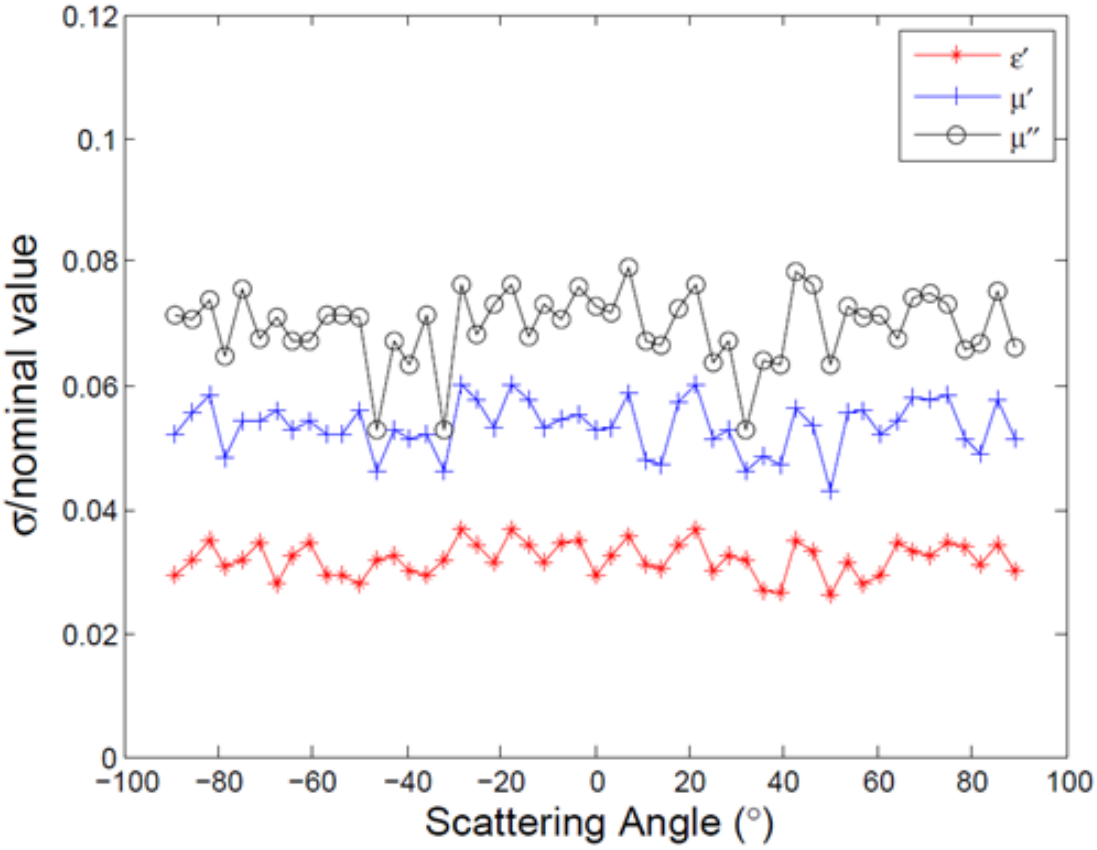

Figure 5.13: Effect of observation (scattering) angle on propagated error for the real part of ϵ, the real part of μ and the imaginary part of μ.

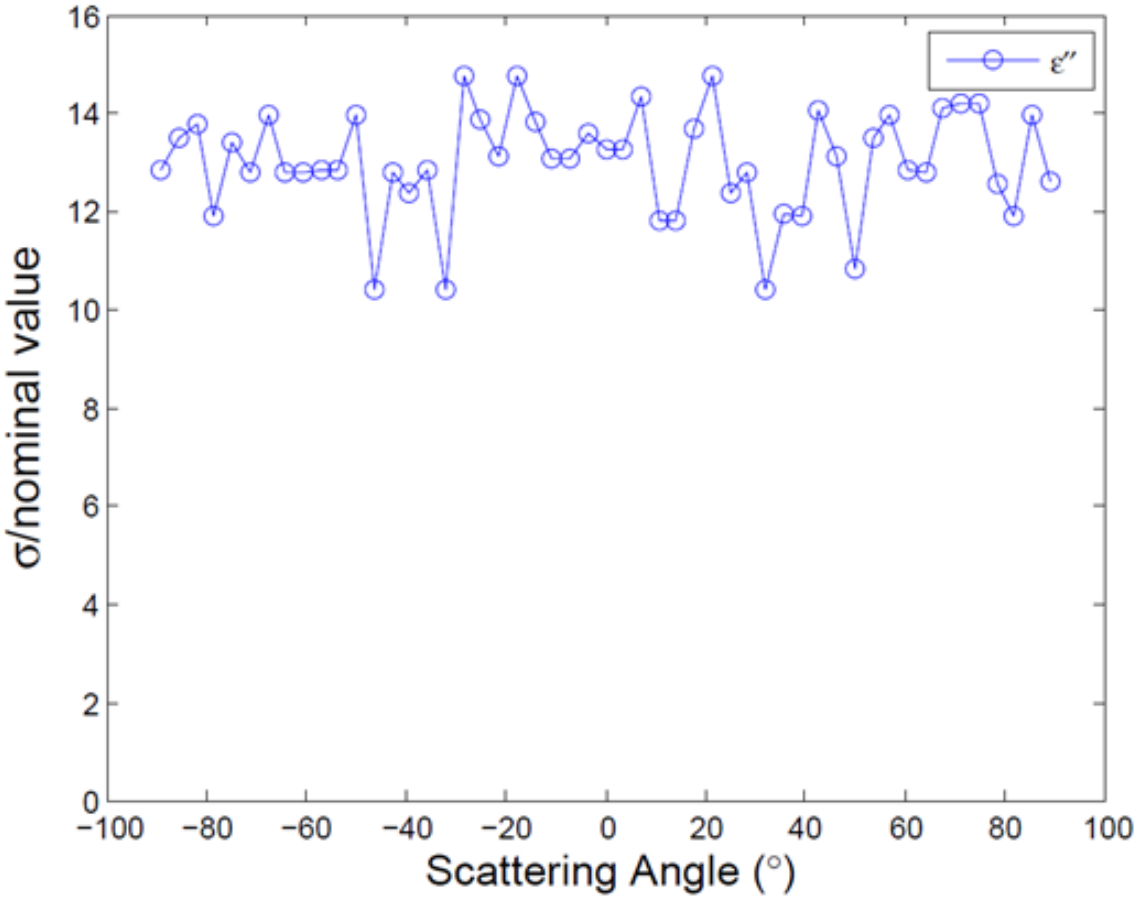

Figure 5.14: Effect of observation (scattering) angle on propagated error for the imaginary part of ϵ.

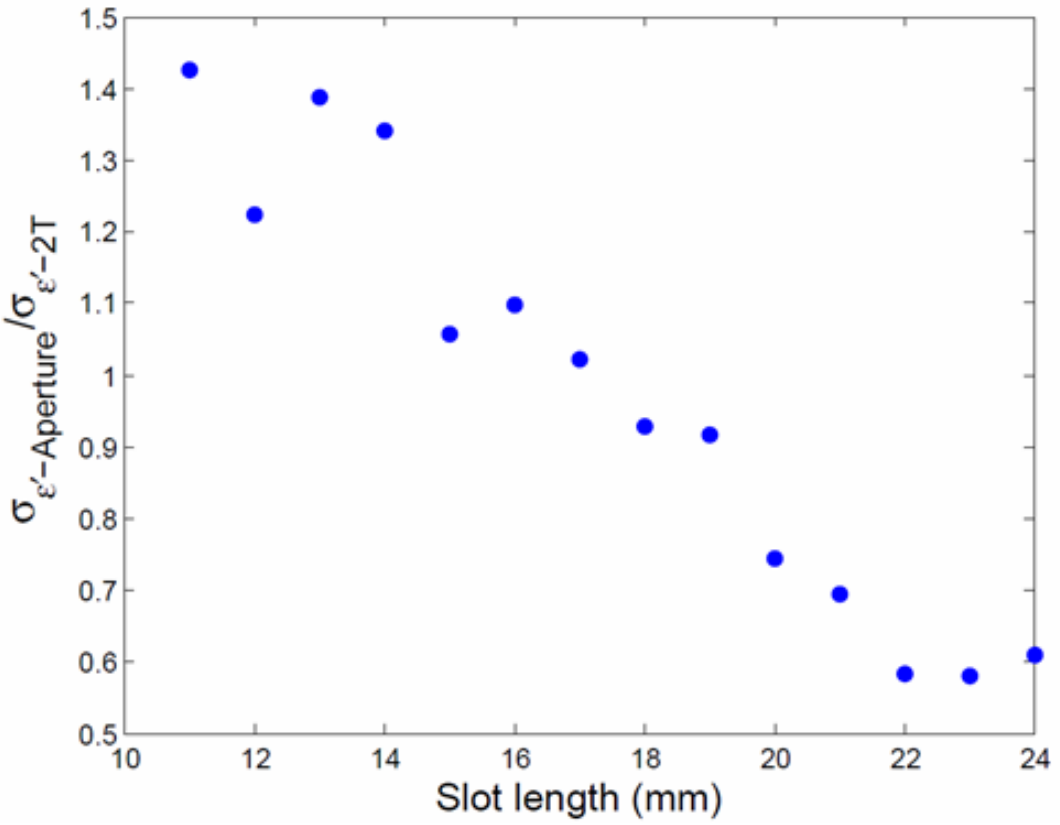

Figure 5.15: Effect of slot length on propagated error for the real part of ϵ.

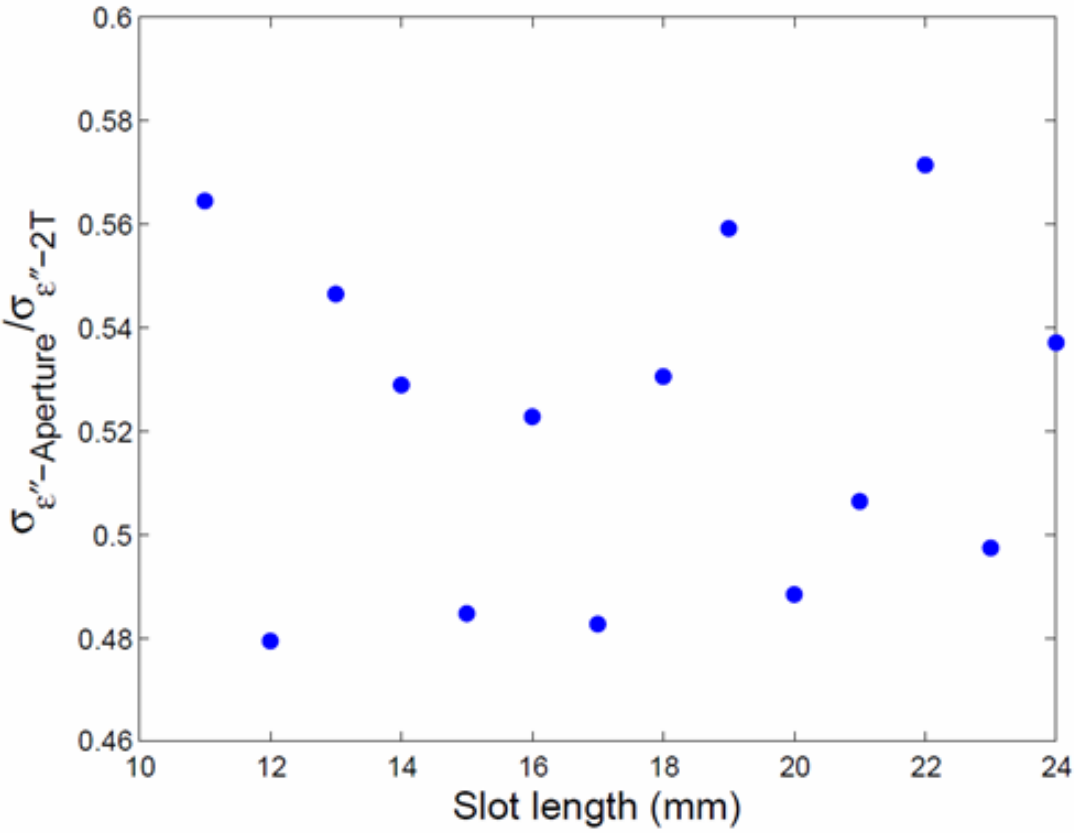

Figure 5.16: Effect of slot length on propagated error for the imaginary part of ϵ.

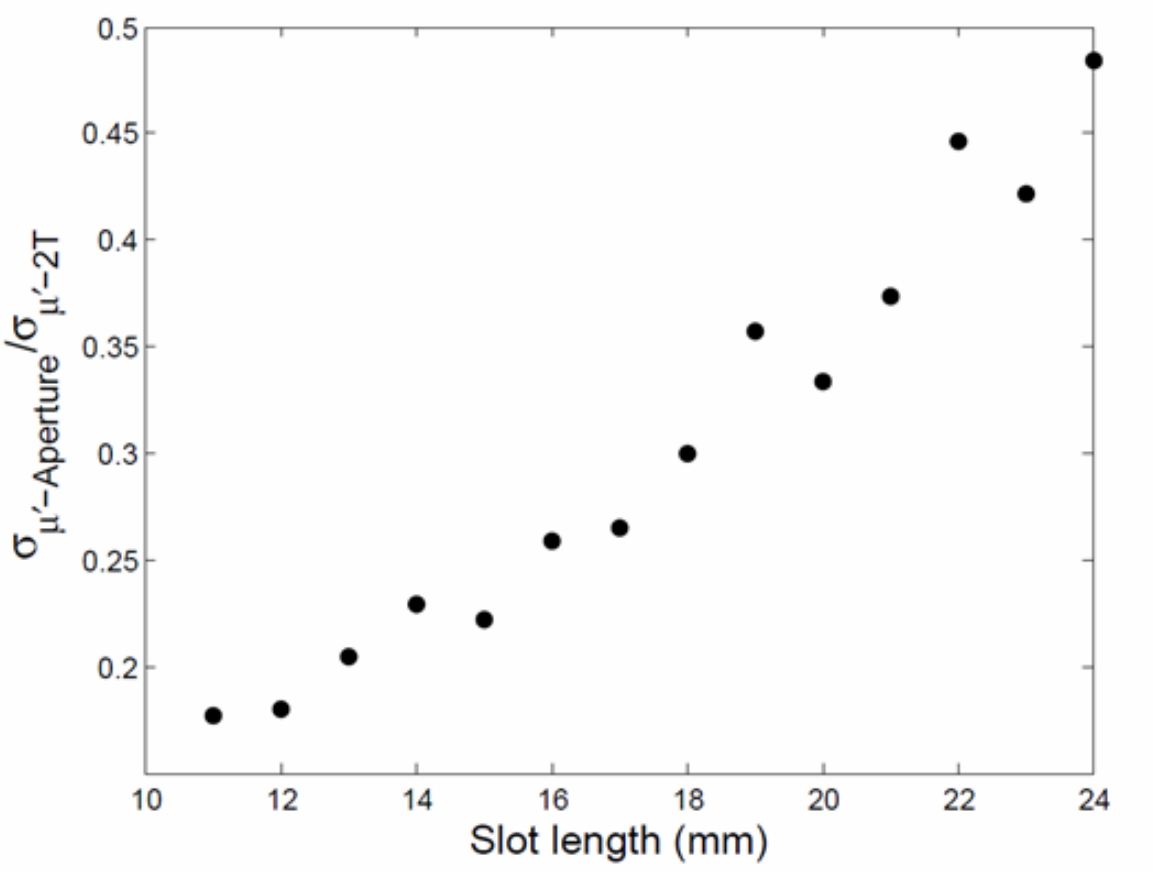

Figure 5.17: Effect of slot length on propagated error for the real part of μ.

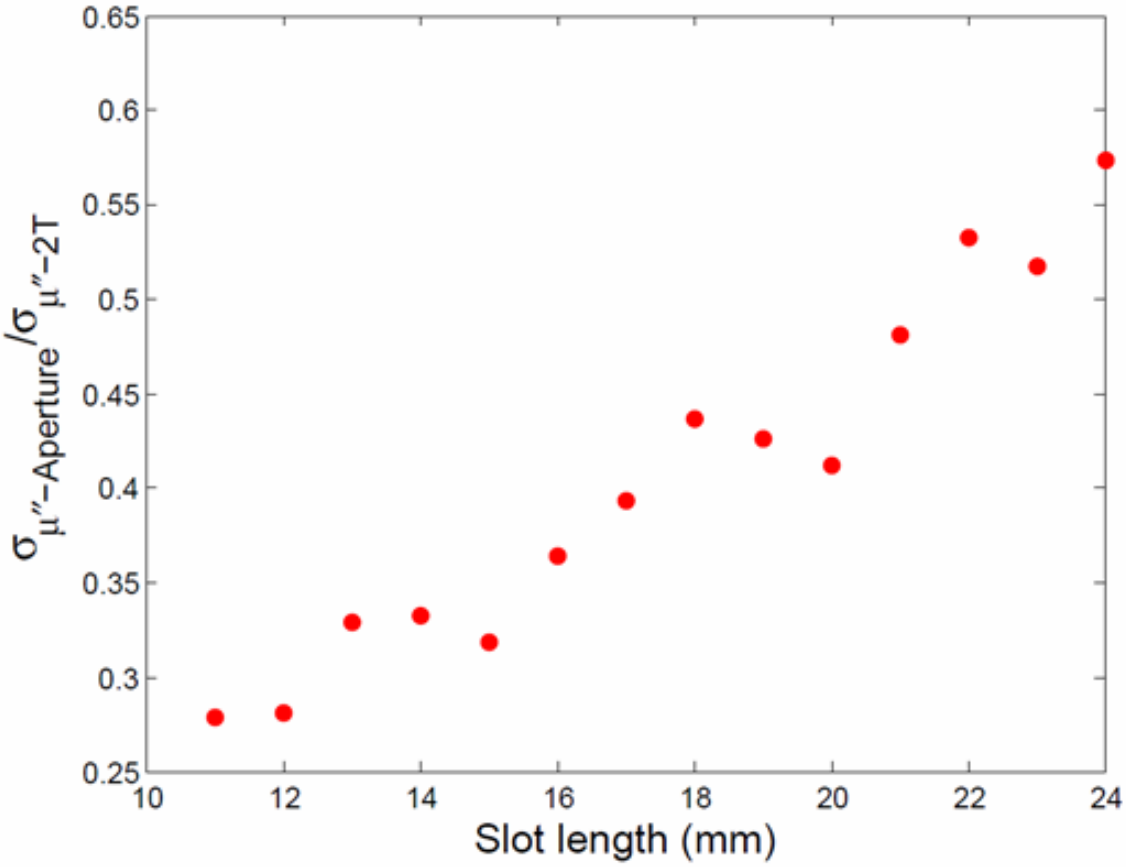

Figure 5.18: Effect of slot length on propagated error for the imaginary part of μ.

Optimal Slot Design	
f (GHz)	2.88
l (mm)	20
w (mm)	1
t (mm)	125

Table 5.3: Chosen optimal aperture screen design parameters.

the slot width kept fixed at 1 mm and the slot length varied. For assessing the effect of changing the slot dimensions, the two-thickness method is considered for comparison again. The results are presented in Figures 5.15 through 5.18. The results show that the error in ϵ' decreases markedly as the slot length is increased from 10 mm to 24 mm. Around 22 mm, which corresponds to the resonant length in free-space, a minimum occurs. On the other hand, for ϵ'', the error does not seem to be affected to the same extent relative to the two-thickness method. For μ' and μ'', an increase in the slot length leads to increase in the error.

5.4.1 Aperture Design Choice

These results obtained in Figures 5.15 through 5.18 show that a "good" choice in the slot length can be determined by striking a balance between the error propagated in ϵ and μ. It should be noted that different length combinations may be chosen to obtain the best results for the various parameters. However, that approach has not been considered in detail in this work. A major determinant of the choice in the aperture design parameters is the practicality of implementation of the design in an experimental setup. An experimental implementation can be carried out by taping a layer of copper tape over a layer of the material-under-test with a conductor backing. How achievable this process is has a major impact on what parameters are chosen in the design and testing of the aperture technique.

5.5 Summary

In this chapter, sensitivity analysis carried out to assess the robustness of the proposed aperture technique are presented. The results show that the technique demonstrates reasonable error values in the extraction of the real part of the permittivity (ϵ'), the real and imaginary parts of the permeability (μ' and μ'') whereas large error values are obtained for the imaginary part of the permittivity (ϵ''). The results obtained for the constitutive parameters other than the imaginary part of the permittivity suggest that the proposed technique is viable for experimental implementation. In cases where an accurate extraction of ϵ is desired, it is recommended that a different method be utilized.

BIBLIOGRAPHY

[1] Samik Raychaudhuri. Introduction to monte carlo simulation. In *2008 Winter Simulation Conference*, pages 91–100, 2008.

[2] K.J. Vinoy and R.M. Jha. *Radar Absorbing Materials: From Theory to Design and Characterization*. Springer US, 1996.

[3] Agilent Technologies. *Agilent Technologies 8510C Network Analyzer System Operating and Programming Manual*. Agilent Technologies Inc.., Santa Rosa, CA, U.S.A., 2001.

[4] R. Fenner, E. J. Rothwell, and L. Frasch. A comprehensive analysis of free-space and guided-wave techniques for extracting the permeability and permittivity of materials using reflection-only measurements. *Radio Science*, 47, 01 2012.

CHAPTER 6

Experiments

6.1 Introduction

Upon the establishment and theoretical validation of the proposed aperture technique, experimental implementation followed. As covered in the previous chapter, the error analysis results predict a robust technique having performance that compares favorably against the two-thickness technique. A question arises: does this robust performance hold true in the field? Experimental validation should involve the measurement of the field reflected by a conductor-backed material layer and the field scattered by a conductor-baked material covered by an aperture screen. To that end, experiments were set up in the range at Michigan State University (MSU) to assess the proposed technique and compare measured results to theoretical predictions.

The experiments at MSU provided encouraging results for measurements of conductor-backed material layers (without the inclusion of the aperture screen). These results will be presented in this chapter. Challenges were encountered that precluded the implementation of the aperture screen measurements in the range at MSU. Beyond the initial conductor-backed material measurements, further experiments were carried out externally in collaboration with Dr Lydell Frasch at Boeing.

As emphasized earlier, unlike many of the other characterization techniques mentioned in Chapter 1, the proposed technique provides the promise of a nondestructive and non-contact means of characterization. It should be noted that the technique does not strictly meet this criteria in its current experimental implementation. It is better described only as being non-destructive since the illuminating mechanism makes no direct contact with the material being interrogated. However, contact has to made since it is necessary to place an aperture adjacent to the sample being measured for the experiments. It is anticipated that with the future design of an appropriate applicator and modification of the numerical solution approach it can be truly non-destructive and non-contact. The different measurements carried out are

detailed in the sections that follow. The purpose of the experiments are to demonstrate the ability of the proposed aperture technique in successfully extracting the constitutive parameters of a given material in the field.

6.2 MSU Measurement Setup and Implementation

The reflectivity arch range at MSU pictured in Figures 6.1 and 6.2 was used for the first series of measurements that were carried out. As shown in the figures, the range consists of a semi-circular metallic rail structure with a pedestal located at its center for holding samples to be measured. The range has a diameter of 6.096 m. Transmitting and receiving horn antennas with converging lenses are mounted on the range at a height of 1.219 m above the floor. The antennas (American Electronics Laboratory model H-1498 with an operating bandwidth between 2 and 18 GHz) can be slid along the rails to attain different angular positions for the plane-wave illumination of the target to be interrogated. This way, the desired incidence and reflection angles can be chosen. The lenses provide a focused beam centered on the sample with low field strength at the edges of the sample. Absorbers were strategically placed in and around the range to prevent unwanted reflections during the measurement process.

A figure illustrating the setup used in the measurement procedure is shown in Figure 6.3. Ports 1 and 2 of an Agilent E5071C vector network analyzer (VNA) were connected to the transmitting and receiving antennas, respectively, through coaxial cables with the target to be measured placed at the center of the arch range as shown. Although both antennas can operate in either transmit or receive mode, only reflection measurements are required for the aperture technique. The reflection measurements were obtained in a bistatic manner with both antennas placed close to each other as shown in 6.4. A bistatic angle of 18° was used in the arrangement; the two antennas were placed along adjacent radials 9° from the normal to the surface of the material sample being measured. The reflections were measured by recording the transmission S-parameter, S_{21} from the transmitting to the receiving port of the VNA. Proper placement and alignment of the material samples was checked with a

laser level.

6.2.1 Measurement Procedure

The procedure for one complete measurement set involves a background measurement, a measurement of a metallic plate, a measurement of the MUT backed by the metallic plate and finally another measurement of the metallic plate. The purpose of the background measurement is to provide a means for subtracting out clutter and isolating the response of the MUT. As such, it should be noted that any modification of the environment after the background measurement would require going back to the beginning of this work-flow as remeasuring the background would be necessitated. The metallic plate measurement is used as a calibrator with the calibration process detailed in [1] employed. For a series of measurements, two of such metallic plate measurements are carried out prior to the first measurement and after the final measurement. This is done in order to have a reference for keeping track of the positional stability of the MUTs and drift across the span of time over which the multiple measurements are performed. The stability and proper alignment of the MUT within the mounting frame used was confirmed using a laser level to check for vertical alignment of the sample through the course of the measurement procedure.

Unless otherwise stated, the following analyzer settings were employed during the measurements: 16 averages with the averaging turned on, an IF bandwidth of 1 KHz, a start frequency of 2 GHz and an end frequency of 18 GHz and 1601 points. A standard 2-port calibration was carried out at the ends of the coaxial cables connected to the horn antennas with the ECal (electronic calibration) functionality on the VNA. These parameters were established after testing out various combinations and striking a balance that enabled reasonable measurement times while still ensuring sufficient dynamic range in the measurements. The measured results are obtained in the form of S-parameter measurements from the VNA in a complex (real and imaginary) format. The corresponding magnitude and phase results are computed in a MATLAB post-processing script.

6.2.2 Measurement Setup Validation

The measurement setup was initially validated by taking a few measurements of known materials. Acrylic and Poly Vinyl Chloride (PVC) samples were measured in the conductor-backed scenario. The results obtained were compared with the theoretical values predicted by equations in Chapter 2 (Section 2.2) for a conductor-backed slab of material. The measured phase results obtained for a 2 ft by 2 ft Acrylic sample layer having a one inch (2.54 cm) thickness are shown in Figure 6.5. These results are compared with theoretical phase values geneated with a dielectric constant of 2.31 which is representative for Acrylic [2] and a loss tangent of zero with the material being assumed as lossless. There is good agreement between the measured and theoretical phase between 2 and 18 GHz but they seem to begin to deviate at higher frequencies.

Similarly, Figure 6.6 shows measured phase results obtained for a 2 ft by 2 ft polyvinyl chloride (PVC) material layer having a one inch (2.54 cm) thickness. The phase values computed using the theoretical expressions from Section 2.2 are again used for comparison. These results are generated with the dielectric constant set to 3.3 [2] and the loss tangent set to zero (lossless assumption). Figure 6.6 shows that there is reasonable agreement between the measured and theoretical results. It should be noted that the discrepancies in results at higher frequencies in both cases are likely attributable to artifacts of the processing steps employed in the measurement calibration as discussed in [1].

6.2.3 RAM Measured Results

The amplitudes of the reflection measurements for Acrylic and PVC are not shown because there was no accurate knowledge of the loss tangent values of the samples. For comparing amplitude measurements, a 0.125-inch thick sample of MT-26 C-RAM was measured. C-RAM is a lossy, carbon filled foam that was chosen because it was readily available and convenient to work with [3]. The availability of C-RAM with adhesive backing allowed for convenience in attaching the sample to a conductor backing. Also, it served as a good starting point for measurements because of its non-magnetic properties. A Nicolson-Ross-Weir

(NRW) waveguide technique implementation [4], [5] was also employed in taking measurements to characterize available C-RAM samples and compare against data published by its manufacturer [3]. A waveguide setup similar to that shown in Figure 6.7 was used. An X-band waveguide was used with a C-RAM sample of thickness 0.125 inches cut to fit in the cross-section of a waveguide spacer of the same thickness. Reflection amplitude and phase results from free-space measurements of a 2 ft by 2 ft, 0.125-inch thick C-RAM sample are compared against the theoretical results generated using constitutive parameters measured by the NRW technique.

A comparison of the measured reflection amplitude and theoretical amplitude is shown in Figure 6.8. As can be seen, there is good agreement between the measured and theoretical amplitude results with discrepancies less than 0.5 dB. On the other hand, the measured and theoretical reflection phase shown in Figure 6.9 do not show good agreement. In the case of the phase results, there are large discrepancies at higher frequencies. Furthermore, the behavior exhibited by the phase measurements is not physically possible as the measured results show an upward trend with an increase in frequency. Over several measurement trials the phase showed marked variation while the amplitude remained relatively unchanged. The inability to properly capture the phase precluded the measurement of the aperture screen with any confidence. Further experiments were carried out on the baseline conductor-backed material setup to investigate the possible sources of measurement error.

6.2.4 Alignment Investigation

In order to determine the source of the measurement error, a 2 ft by 2 ft and 0.225-inch (0.5715 cm) thick sheet of Plexiglass was measured five separate times. The average and standard deviations of the reflection phase and amplitude were calculated. The system was calibrated between each measurement. The reflection amplitude results are shown in Figure 6.10 while Figure 6.11 shows the reflection phase results. In each figure the black line shows the average of the measurements, while the green and red lines show the 95% confidence interval (mean ± 2 standard deviations). The blue line shows the theoretical

curves computed assuming a dielectric constant of 2.31 and a loss tangent of zero. The results show a significant variation between measurements. This variability may account for the poor performance of the C-RAM measurements.

It is hypothesized that the variation in measurement is due to a slight misalignment of the sample with the transmitting and receiving horns. It is difficult to accurately reposition the sample in the pedestal mount after it has been removed, due to slight rotations and difficulty achieving a true vertical stature. Note that at 18 GHz, a shift in distance of about 0.023 mm produces a 2-way phase change of 1 degree, and thus very accurate positioning is crucial to producing reliable measurements. A much more secure measurement system, with the sample placed against a rigid vertical structure, is needed. Alternatively, a focused-beam reflection system, where the sample is placed on a rigid horizontal surface and the antennas are positioned above, would be appropriate. A system that meets the aforementioned requirements was available to Dr Lydell Frasch of Boeing and experiments carried out by him are presented in the sections that follow.

It is instructive to note that simulations can also be carried out using a tool such as HFSS or CST to further investigate the alignment problems. However, that path was not considered as the computational resources available were not amenable to a full-wave simulation approach.

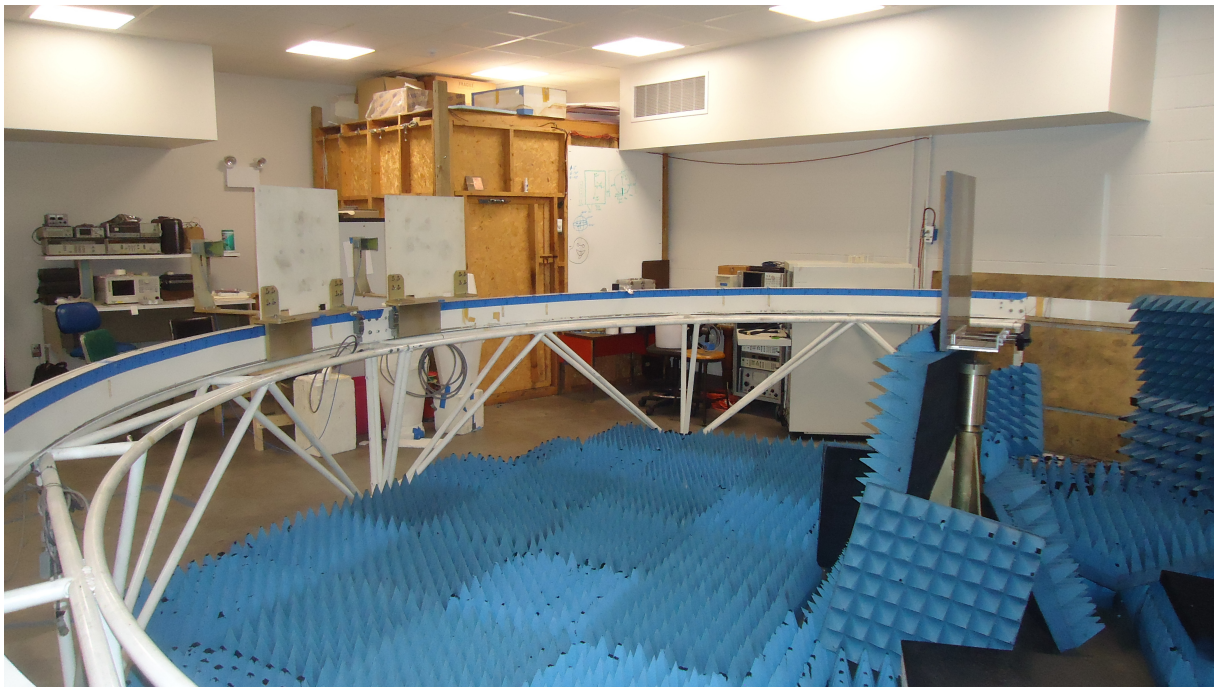

Figure 6.1: Reflectivity arch range at MSU.

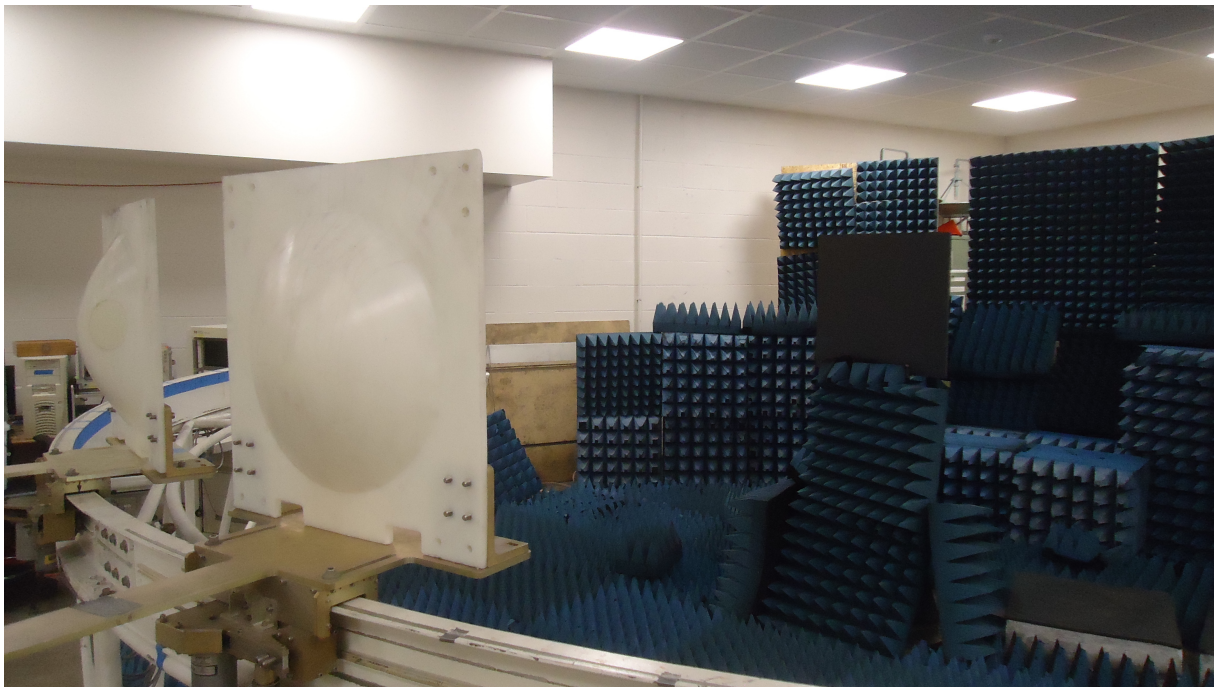

Figure 6.2: Reflectivity arch range at MSU – Alternate view showing sample target.

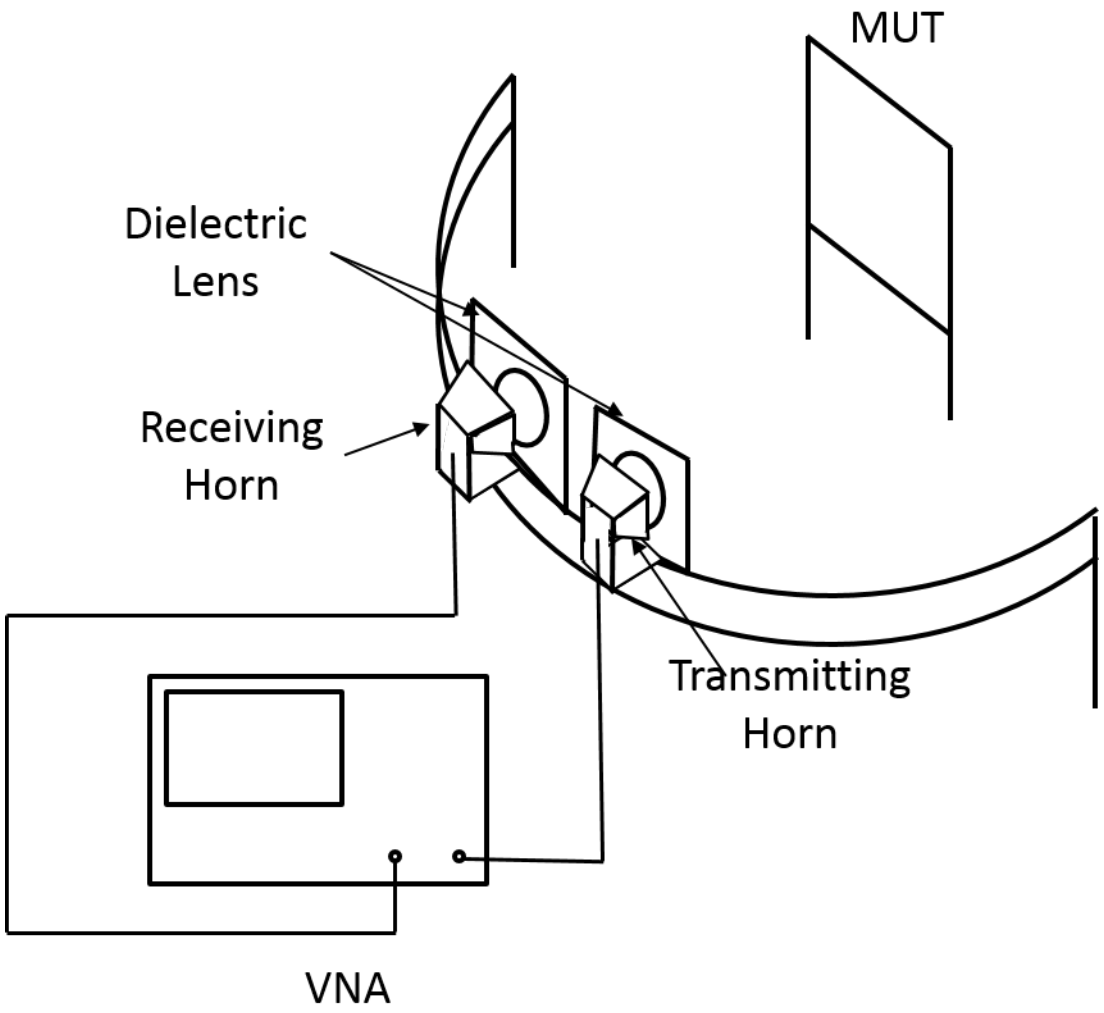

Figure 6.3: Measurement Setup in MSU Arch Range.

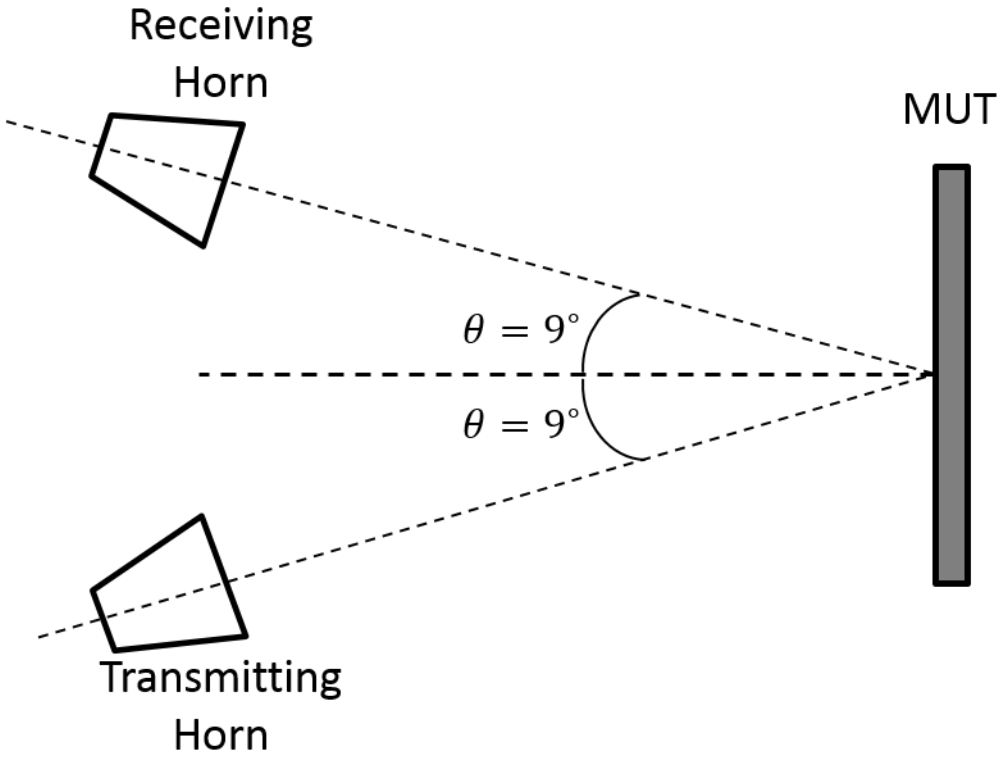

Figure 6.4: Bistatic Geometry Setup.

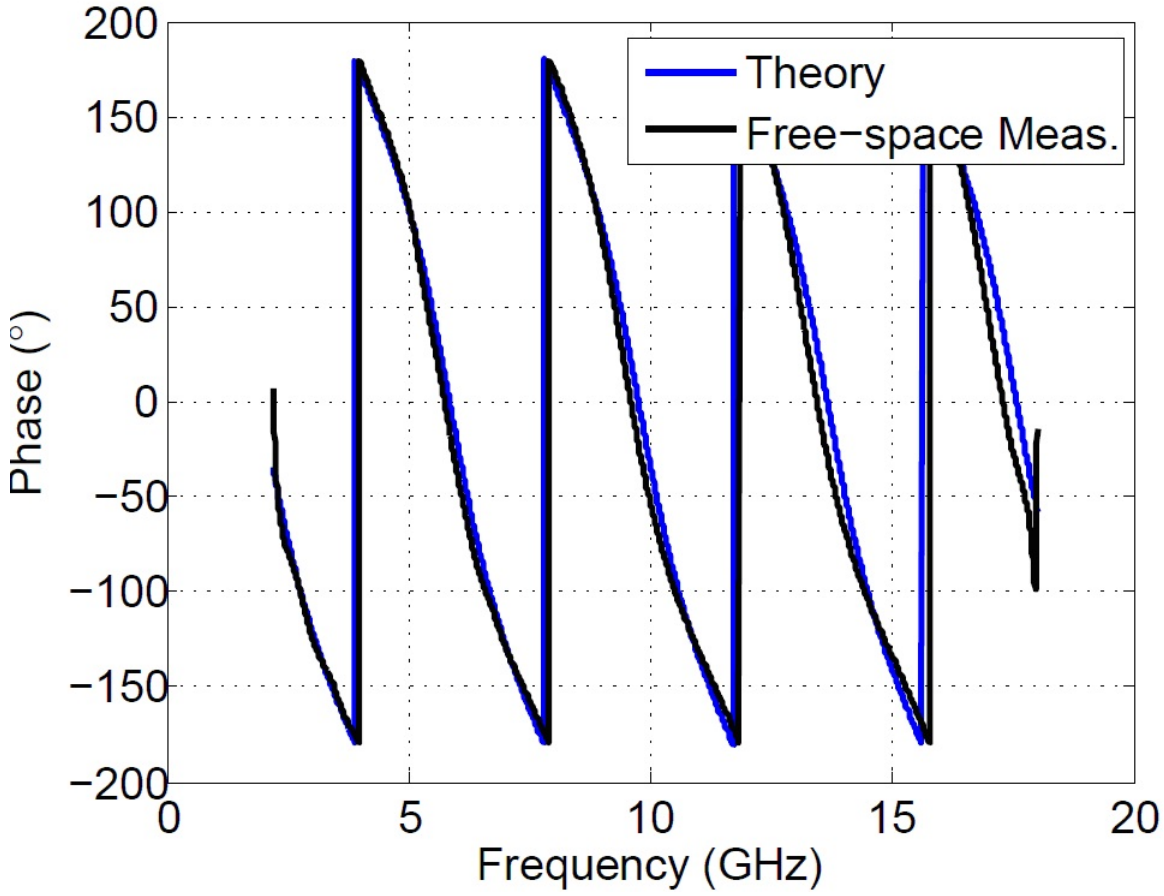

Figure 6.5: Measured and theoretical reflection phase of a 1-inch thick layer of conductor-backed Acrylic.

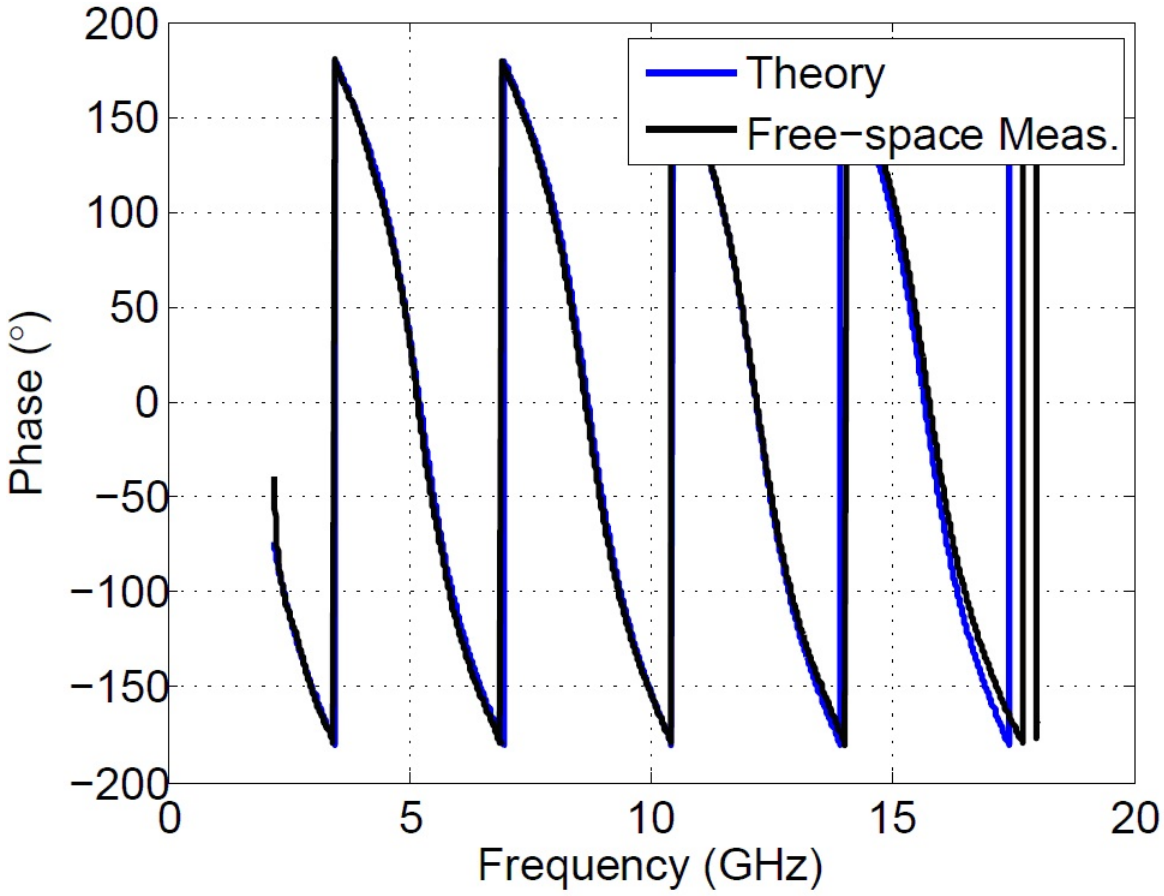

Figure 6.6: Measured and theoretical reflection phase of a 1-inch thick layer of conductor-backed PVC.

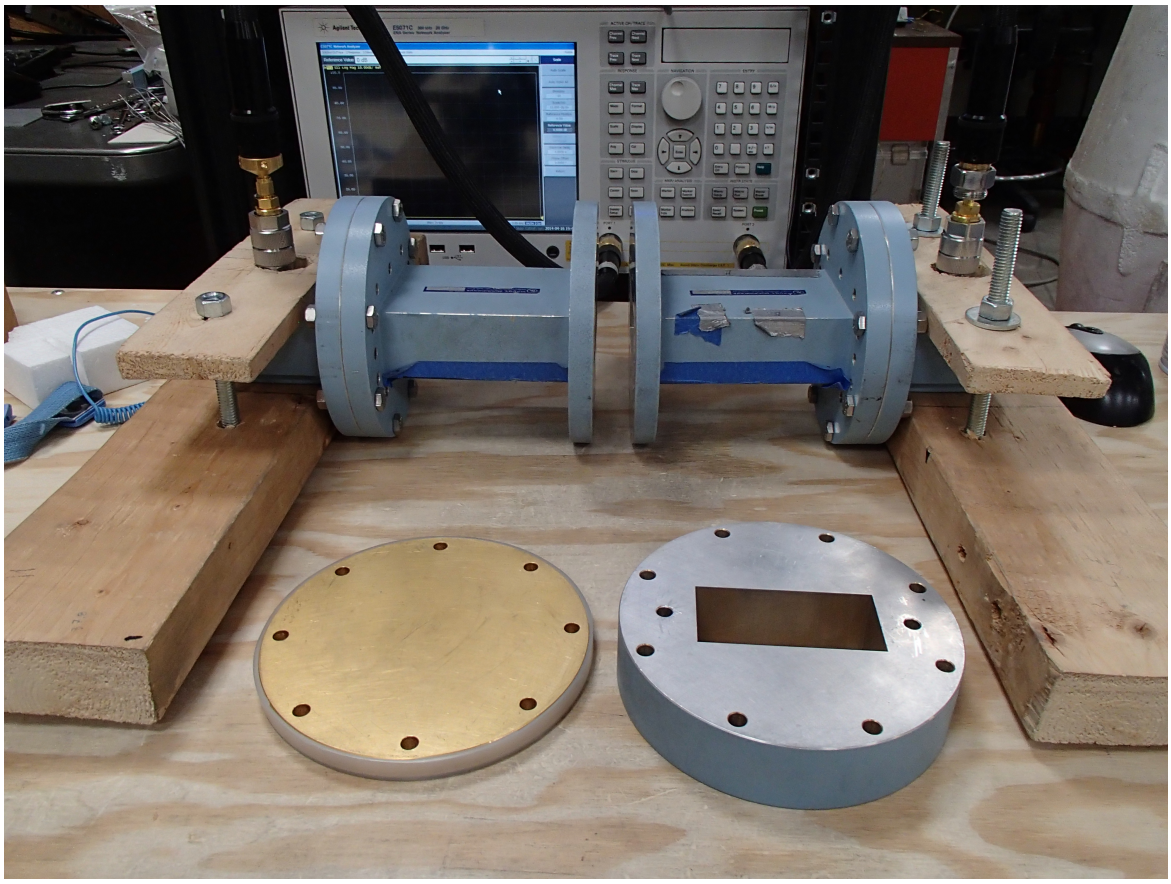

Figure 6.7: Waveguide Material Measurement Setup.

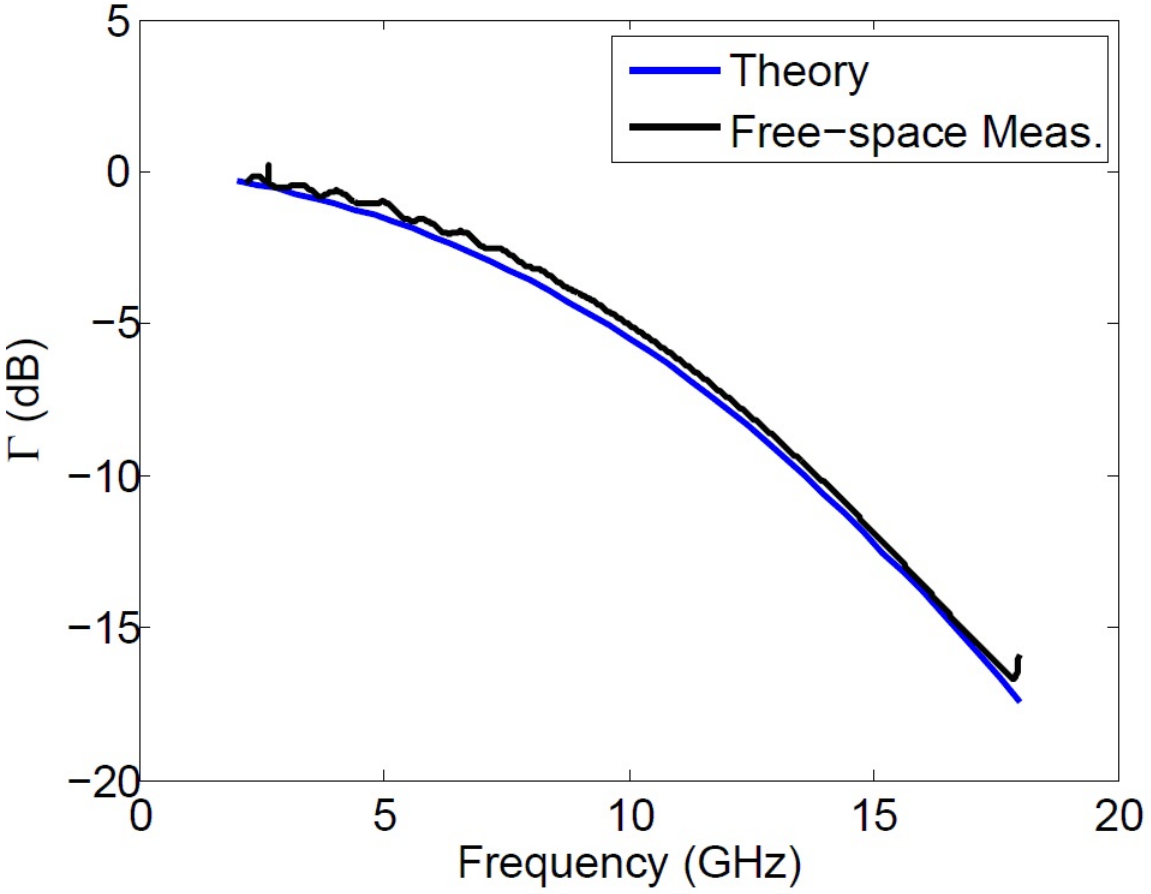

Figure 6.8: Measured and theoretical reflection amplitude of a 0.125-inch thick layer of MT-26 C-RAM.

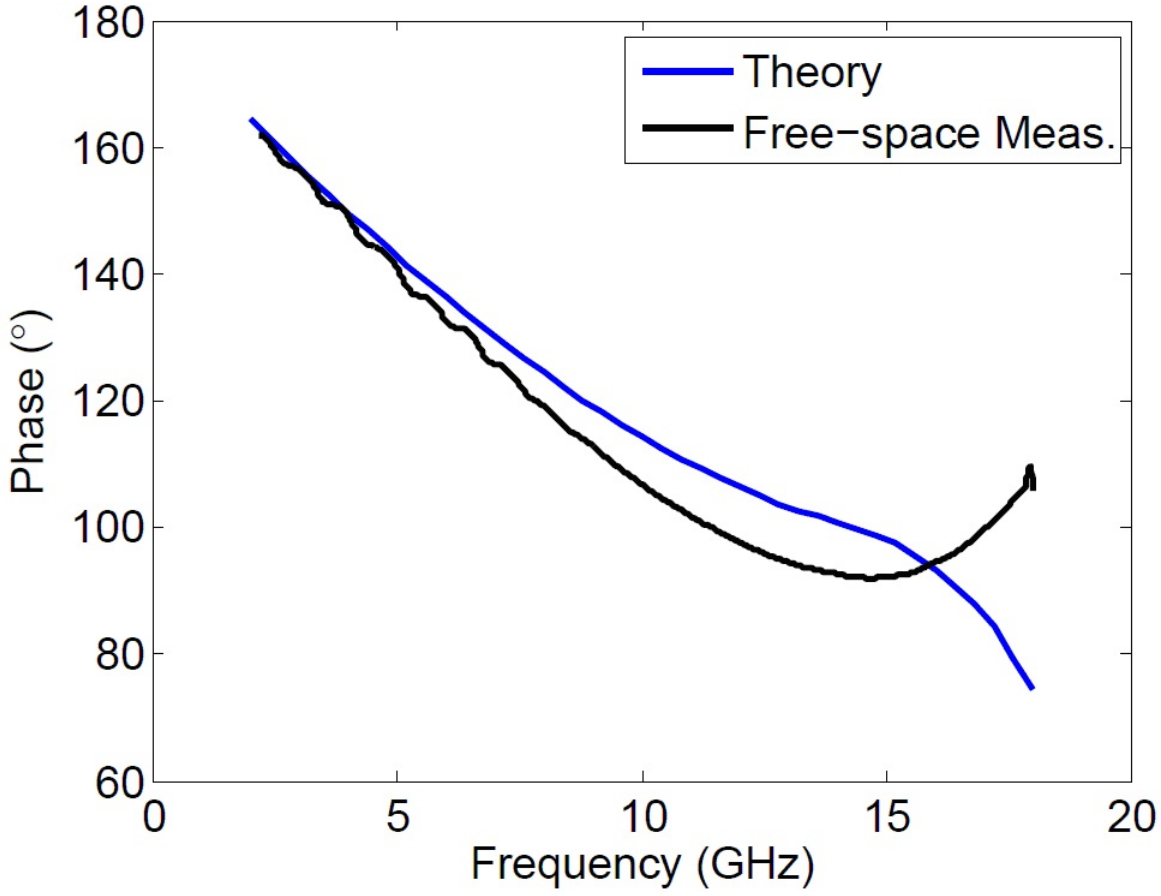

Figure 6.9: Measured and theoretical reflection phase of a 0.125-inch thick layer of MT-26 C-RAM.

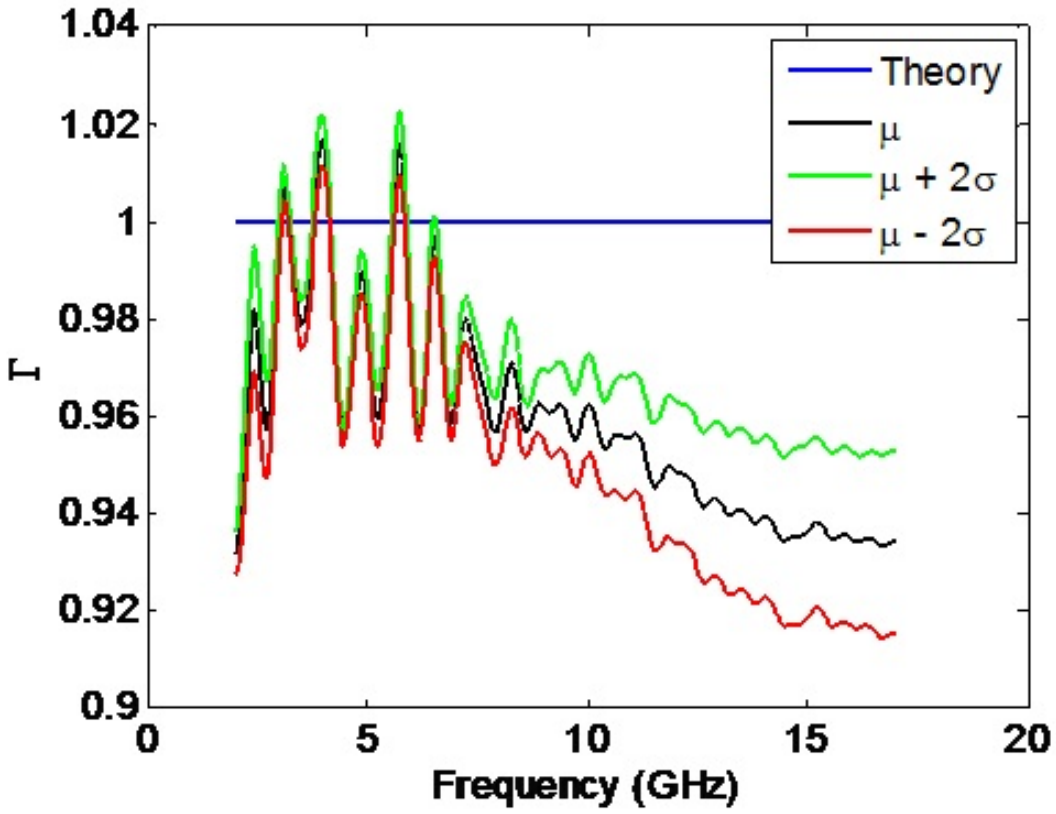

Figure 6.10: Measured and theoretical reflection phase of a 0.225-inch thick layer of Plexiglass.

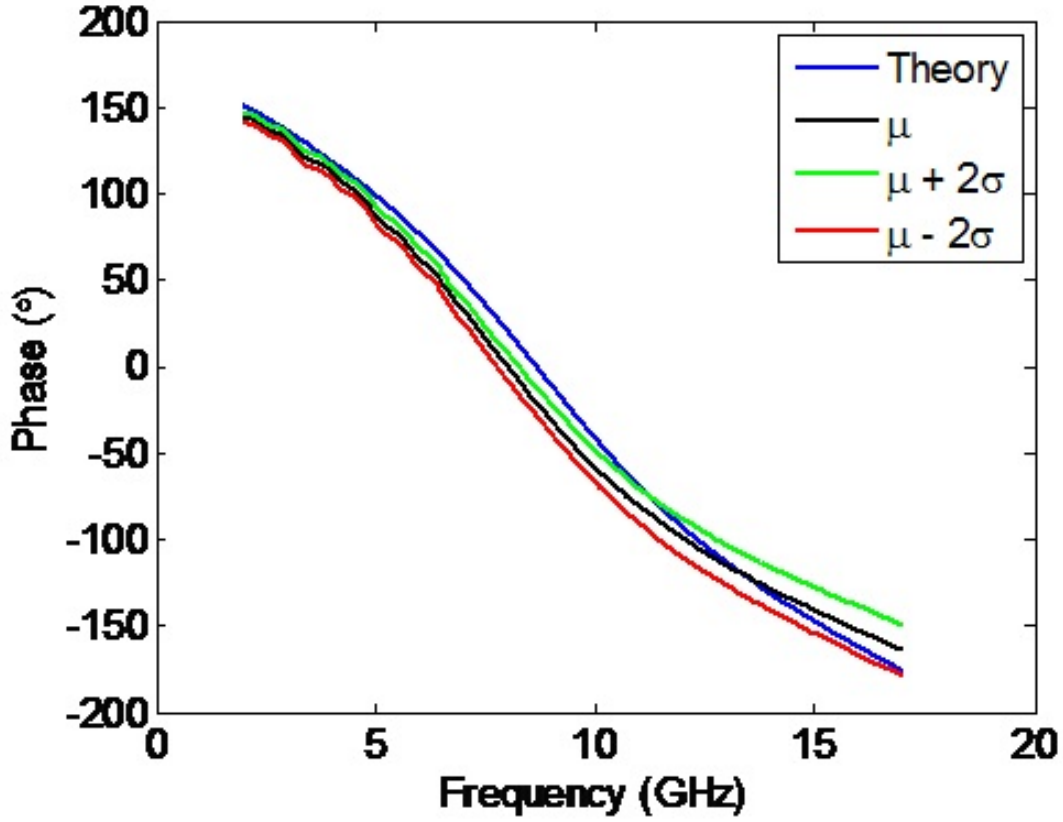

Figure 6.11: Measured and theoretical reflection amplitude of a 0.225-inch thick layer of Plexiglass.

6.3 External Measurements

As mentioned earlier, issues with alignment accuracy made it unfeasible to proceed with the aperture screen measurements in the range at MSU. In collaboration with Dr Lydell Frasch, additional experiments were performed at the Boeing facility in Seattle. The setup utilized for these measurements is a table-top system which ensures better stability in the position of the sample. This is in contrast to the initial measurement setup in the MSU arch range where the vertical orientation of the MUT made accurate alignment difficult to achieve. The configuration that was employed in these measurements is depicted in 6.12. The setup included transmit and receive horn antennas that were moved by positioners to obtain desired incident and scattering angles. The horns were oriented so that the direction of the electric field is perpendicular to the page in the figure shown, which is along the y-direction described by the coordinate system included. An absorber baffle was also present to reduce coupling between the transmit and receive antennas. For all the measurements, calibration was carried out against a metallic plate placed at the same horizontal position as the material samples. It should be noted that no focusing lenses were incorporated into the measurement setup.

6.3.1 Measurement Validation

6.3.1.1 Conductor-Backed Material Measurements

For validation purposes, measurements of a conductor coated MagRAM sample that were taken in the absence of an aperture screen were compared against results generated from the conductor-backed theory shown in Section 2.2. The material properties of the MagRAM sample were determined previously at Boeing utilizing a hybrid approach that combined results obtained from waveguide and free-space implementations of the NRW technique. Figures 6.13 and 6.14 show the material properties of the MagRAM sample utilized in these measurements.

The measured results that were obtained are compared against theoretical results and shown in Figures 6.15 through 6.18. Figures 6.15 and 6.16 show the reflection magnitude and

phase response of the conductor-backed MagRAM, respectively, measured at a bistatic angle of 20°. The results are seen to show agreement except for deviations that can be observed where resonance occurs in the magnitude response. Figures 6.17 and 6.18 show similar results when a bistatic angle of 60° was considered. Again, there is agreement between the theoretical and measured results for both the reflection magnitude and phase except for discrepancies in the vicinity of the resonance. There a couple of factors that may account for these discrepancies in the results. The thicknesses across the material sample surface were not uniform as MagRAM materials are non-rigid. Also, it is not unusual for differences to exist in the constitutive parameters of MagRAM samples across different material batches.

Similar results are obtained for measurements of a foam material and the material AN-74 which is a non-magnetic absorbing material. The permittivity properties of AN-74 are shown in Figure 6.19. The phase results for the 60° bistatic case of the AN-74 measurements are shown in Figure 6.20. As was observed in the case of the MagRAM measurements, the magnitude and phase results generally show similar behavior but begin to deviate as resonances in the magnitude responses are approached.

6.3.1.2 Aperture Screen Adjacent Conductor-Backed Material Measurements

Measurements results for two aperture screens were considered. Firstly, a "small" slot having dimensions l = 20 mm and w = 1 mm was measured and, secondly, a "large" slot with dimensions l = 254 mm and w = 12.7 mm was measured. The aperture screen was implemented by placing a 5 mil thick layer of Aluminum foil with a slot cut out over the conductor backed material layer. Recalling earlier discussions regarding the scattering angle choice, there was a need to refrain from choosing specular scattering angles in order to avoid scenarios where the slot response is dominated by the much larger specular reflection. As such, the slot responses are considered in the case of normal incidence and a scattering angle of 45°.

The measured reflection magnitude and phase results without a slot, with the inclusion of the small slot, and with the inclusion of the large slot are obtained for conductor-backed

MagRAM and conductor-backed AN-74 samples. These results are shown in Figures 6.21 through 6.24. It is notable that the results with the slots differ markedly from the conductor-backed results for the case of AN-74, particularly for the large slot. AN-74 is a more lossy material and is less susceptible to reflections of parallel-plate waveguide modes from the edge of the material sample, which are not accounted for in the theory where the material layer is assumed to be infinite in extent.

The proposed calibration approach where a ratio is taken between the conductor-backed material response in the presence of the slotted conductor and the slotted conductor response in free space is not easily achievable with a table top system. An alternative approach was utilized for validation of the measurements with the aperture screen present. The approach establishes a comparison between the the measurements and the theoretical model by taking ratios of the material response for the conductor-backed MagRAM and the conductor-backed AN-74. The equality of the ratios

$$\frac{MagRAM_m}{AN74_m} = \frac{MagRAM_{th}}{AN74_{th}}. \tag{6.1}$$

should hold if the theoretical and measured results are in complete agreement. Using the described approach, it is possible to compare measured results against the theoretical model. The results obtained are shown in Figure 6.25.

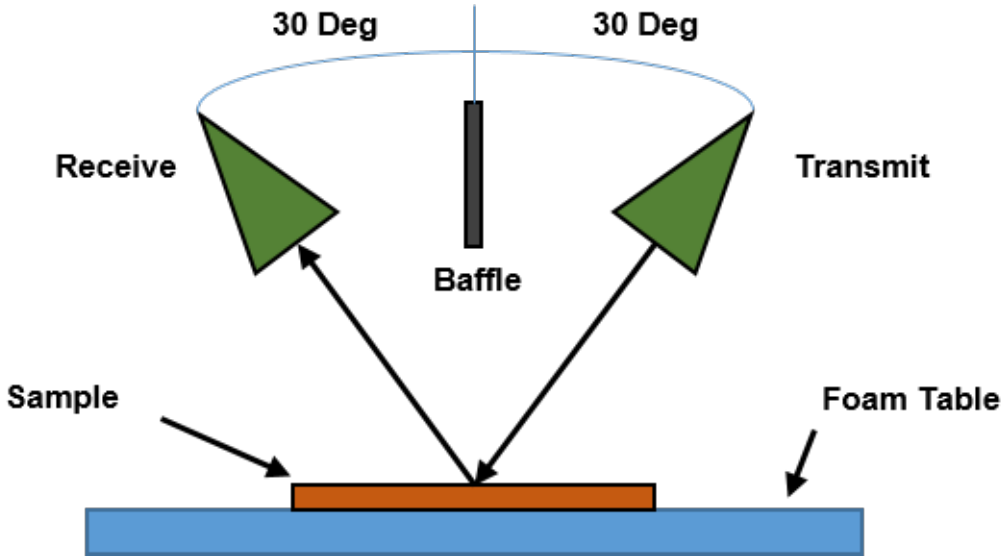

Figure 6.12: Depiction of measurement system employed for experiments at Boeing.

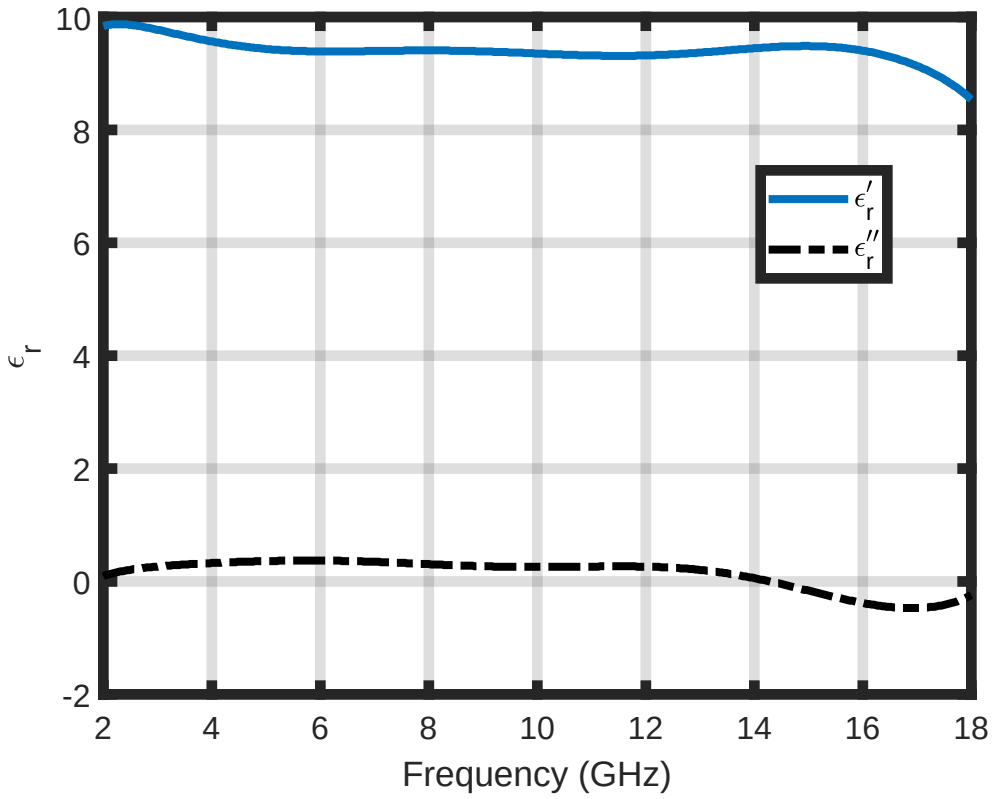

Figure 6.13: Relative permittivity for MagRAM sample utilized in reflection measurements.

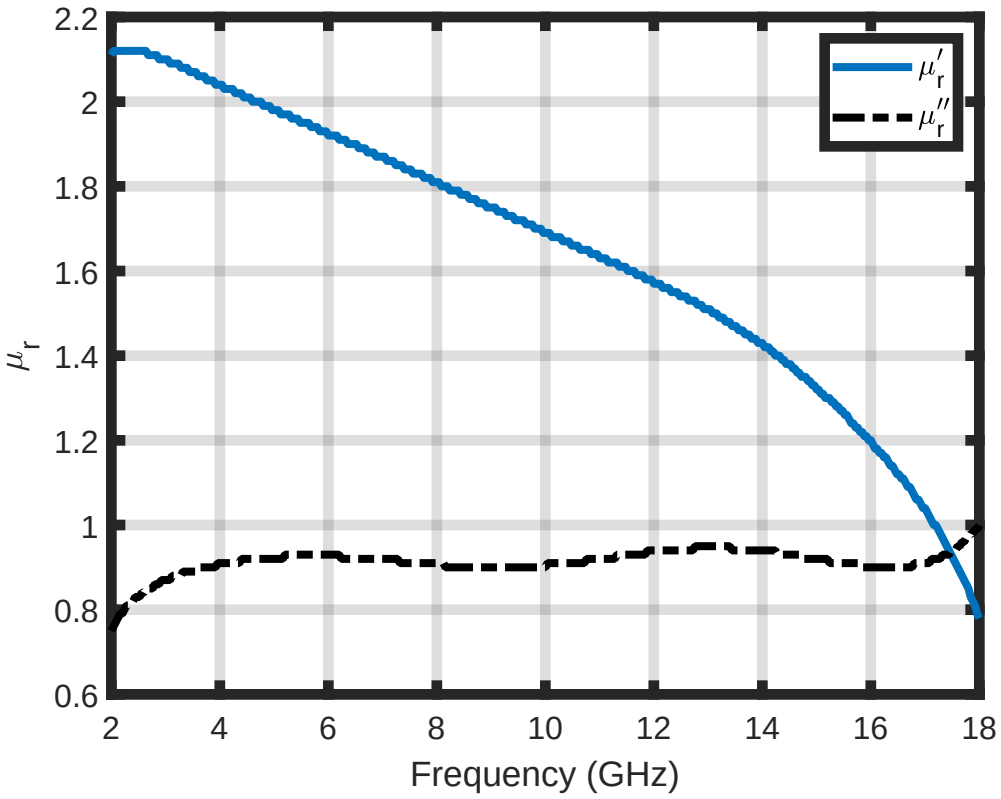

Figure 6.14: Relative permeability for MagRAM sample utilized in reflection measurements.

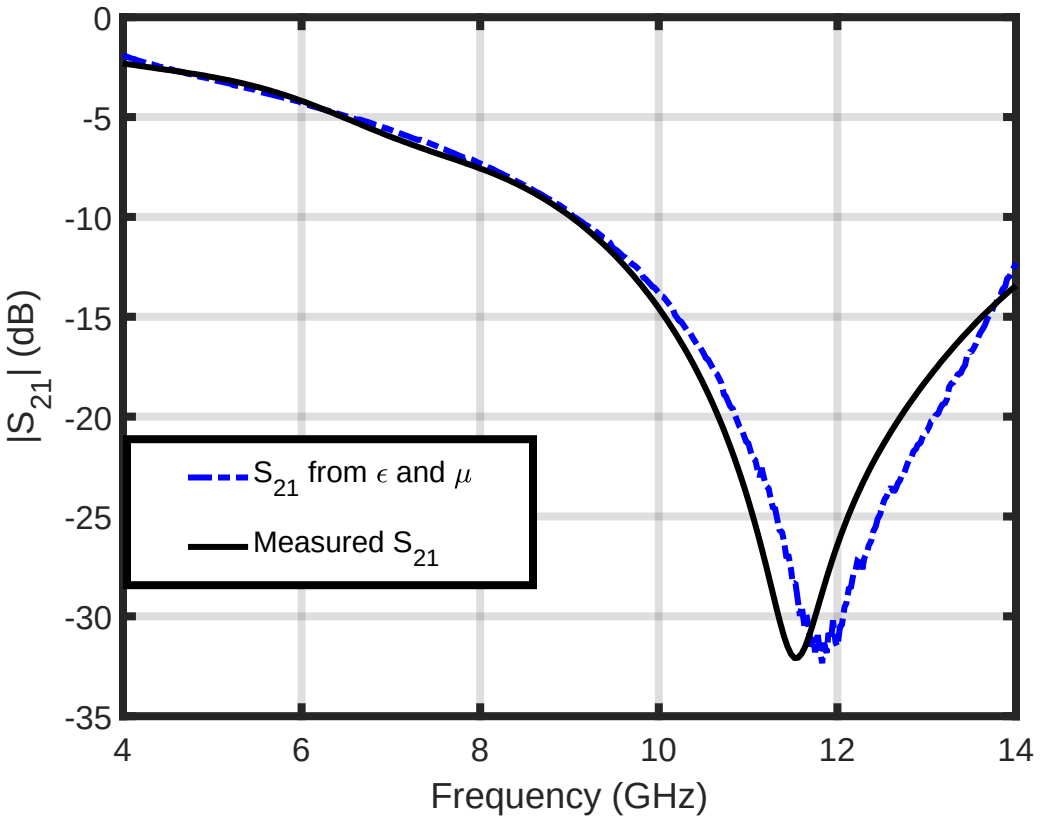

Figure 6.15: MagRAM reflection magnitude validation for 20° bistatic measurement (incidence angle = 10° and scattered angle = 10°).

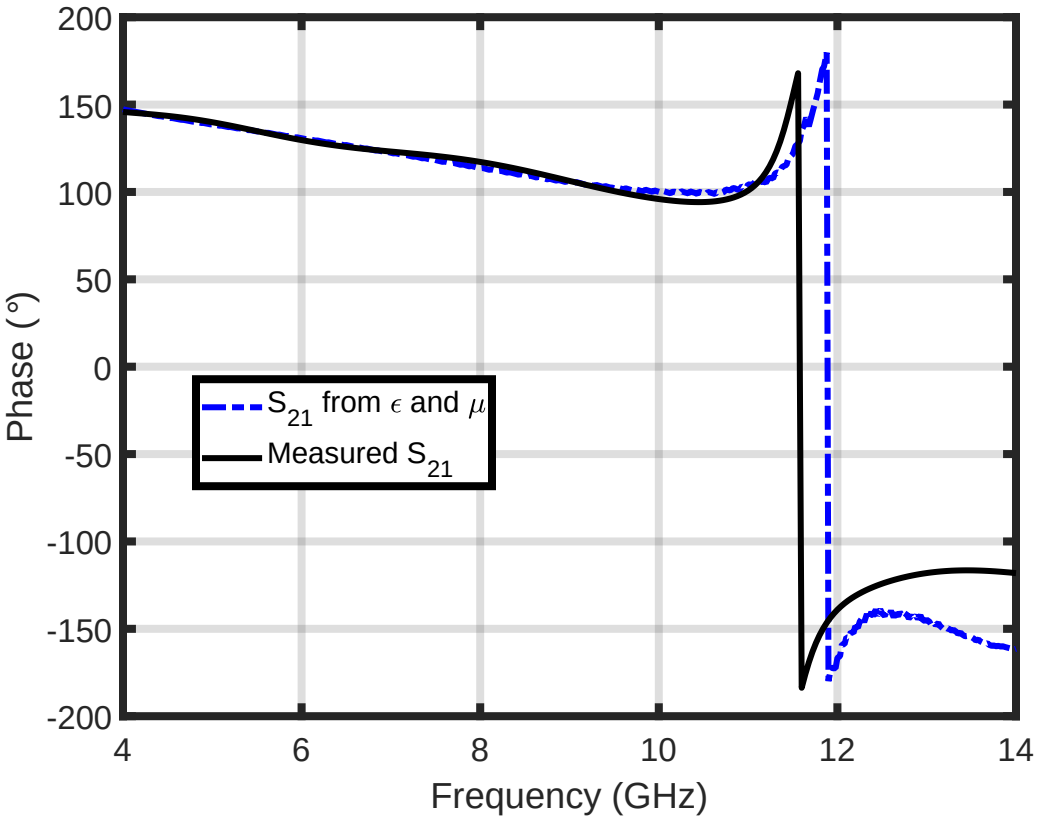

Figure 6.16: MagRAM reflection phase validation for 20° bistatic measurement (incidence angle = 10° and scattered angle = 10°).

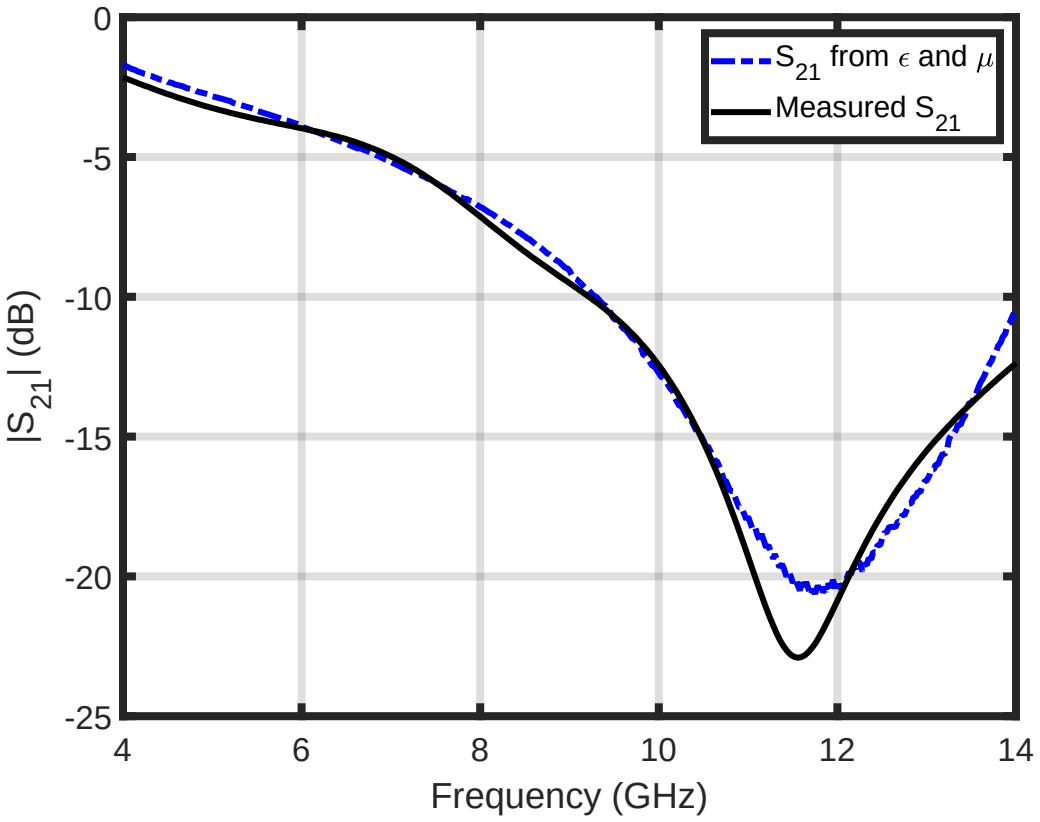

Figure 6.17: MagRAM reflection magnitude validation for 60° bistatic measurement (incidence Angle = 30° and scattered angle = 30°).

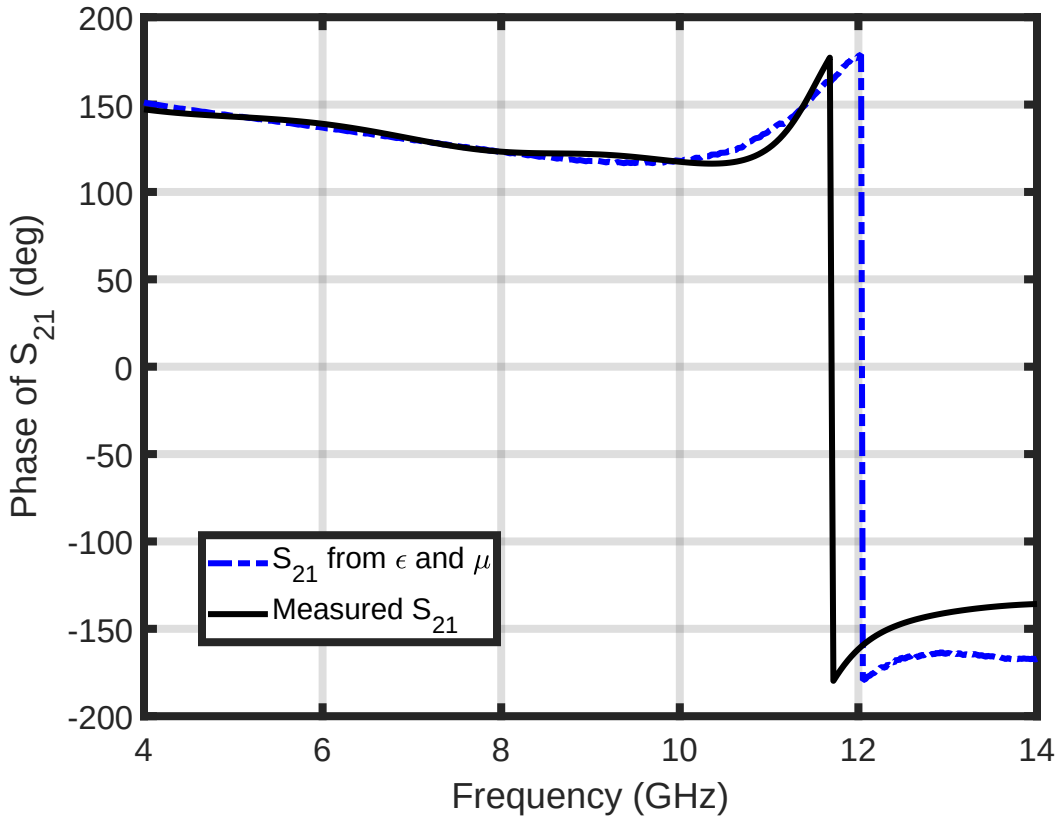

Figure 6.18: MagRAM reflection phase validation for 60° bistatic measurement (incidence angle = 30° and scattered angle = 30°).

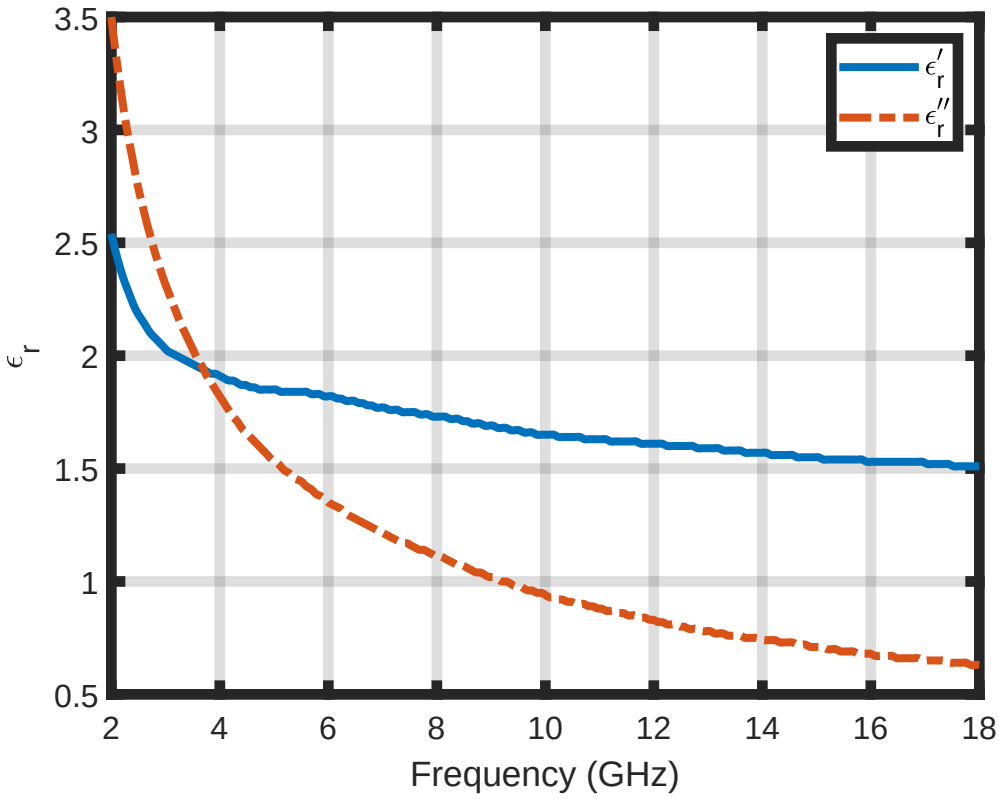

Figure 6.19: Relative permittivity for AN-74 sample utilized in reflection measurements.

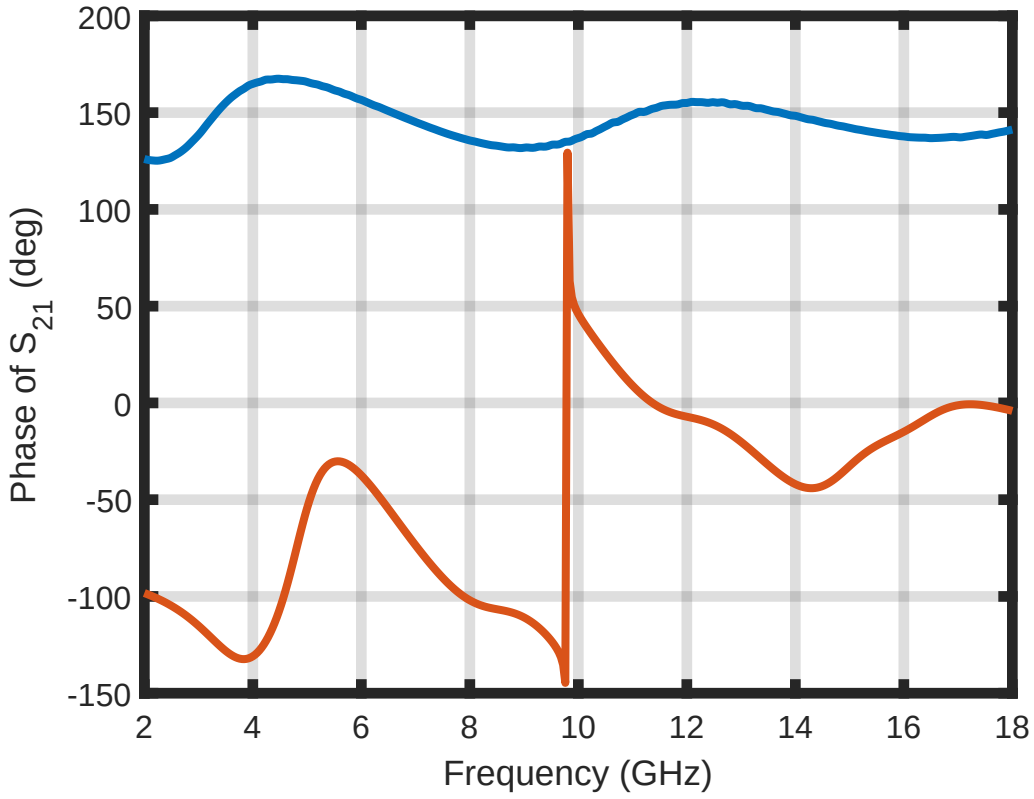

Figure 6.20: AN-74 reflection phase validation for 60° bistatic measurement (incidence angle = 30° and scattered angle = 30°).

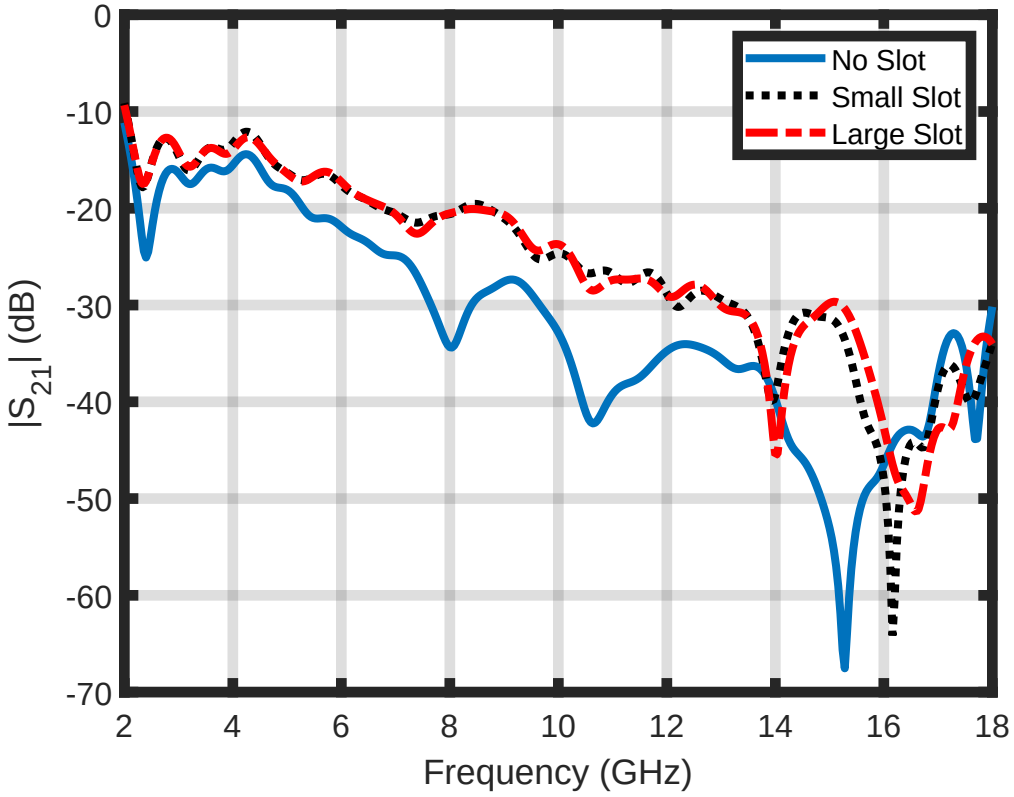

Figure 6.21: S21 magnitude response of conductor-backed MagRAM without an aperture screen present, with the small slot, and with the large slot.

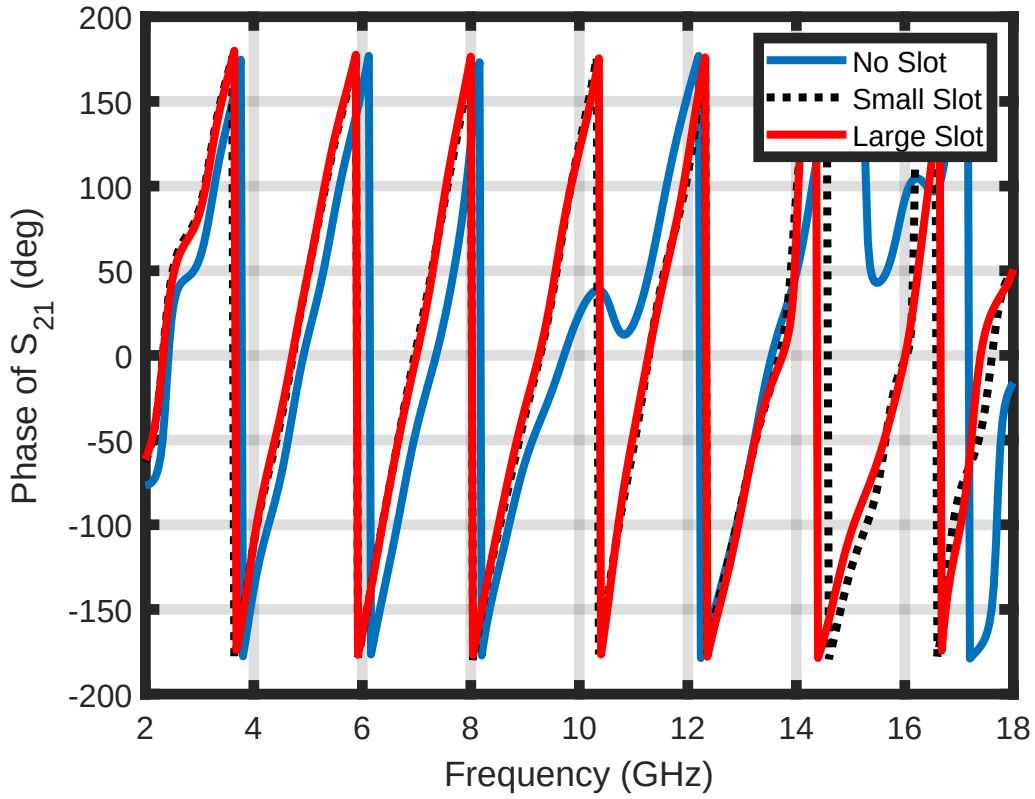

Figure 6.22: S21 phase response of conductor-backed MagRAM without an aperture screen present, with the small slot, and with the large slot.

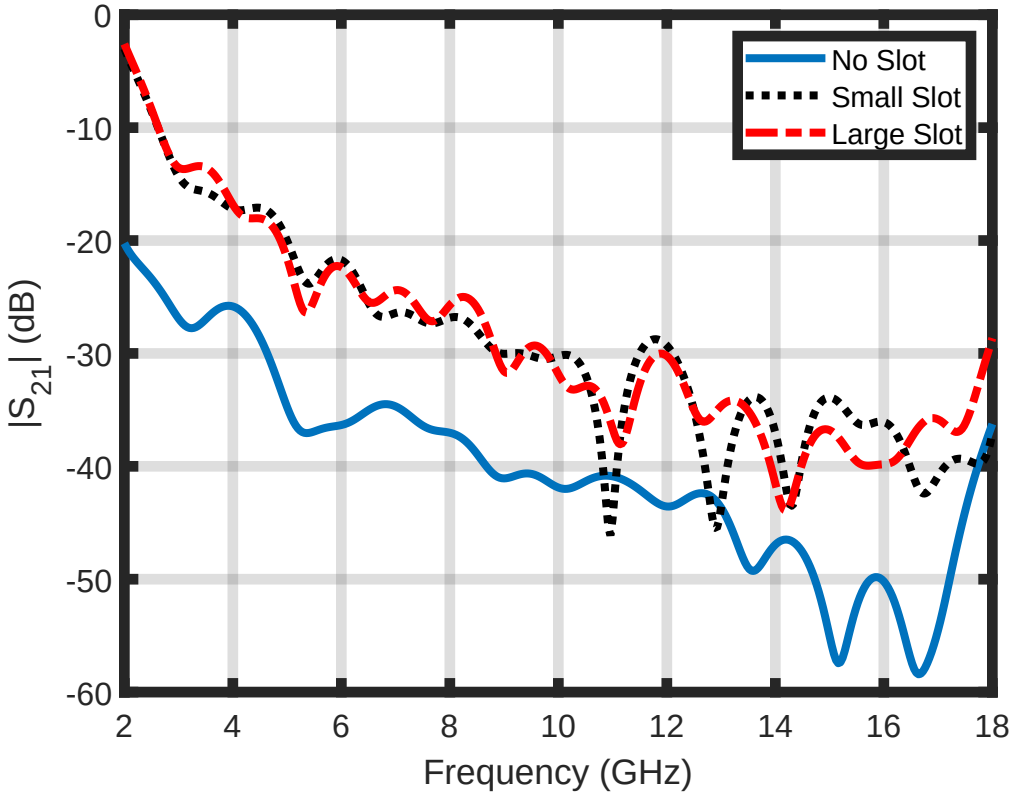

Figure 6.23: S21 magnitude response of conductor-backed AN-74 without an aperture screen present, with the small slot, and with the large slot.

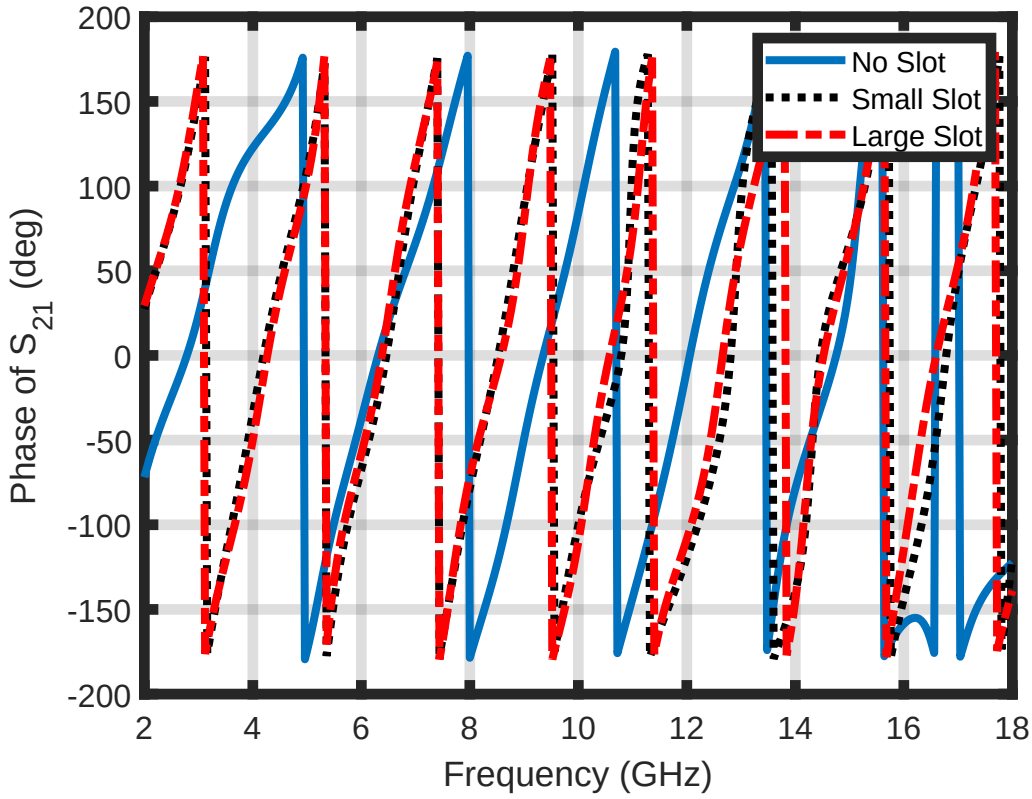

Figure 6.24: S21 phase response of conductor-backed AN-74 without an aperture screen present, with the small slot, and with the large slot.

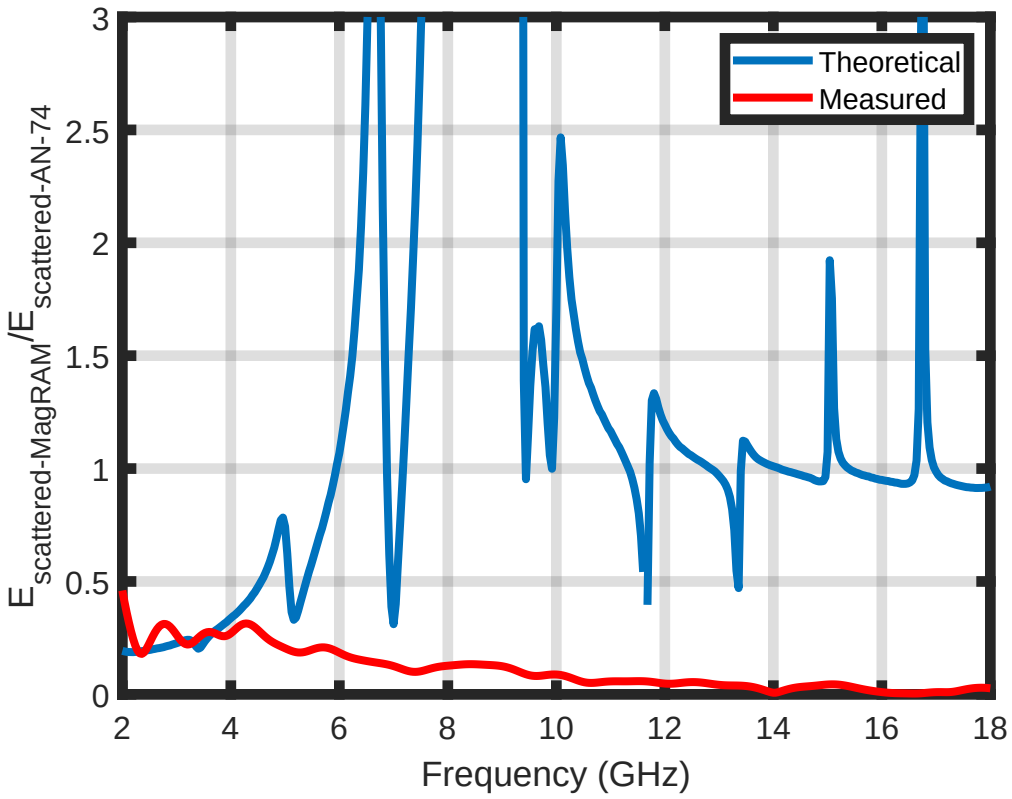

Figure 6.25: Comparison between measured and theoretical results for MagRAM and AN-74.

6.4 Summary

In this chapter, experiments carried out to implement the proposed aperture screen technique are detailed and the results obtained are presented. Experiments carried out in the MSU arch range revealed the sensitivity of the measurement setup to inaccuracies in alignment and the importance of mechanical stability in ensuring that the reflection phase responses are accurately measured. An alternative approach for executing the measurements was needed for the implementation of the aperture screen technique.

Access to external measurements carried out by Dr Lydell Frasch allowed for further experimentation. The results obtained from these measurements compare favorably against theory for the conductor-backed material measurements in the absence of the aperture. However, there was a need for the developments of a different calibration approach before measurement results and theoretical results could be compared with the aperture screen. The comparisons reveal that differences in the theoretical and experimental implementations of the aperture technique have to be explored further. Discussions of these differences are covered in the next chapter.

BIBLIOGRAPHY

[1] Bradley T. Perry, Edward J. Rothwell, and Leo C. Kempel. A comparison of the measured pulse response of layered materials using time- and frequency-domain systems [measurements corner]. *IEEE Antennas and Propagation Magazine*, 49(5):117–123, 2007.

[2] Edward J. Rothwell. Extraction of the wideband dielectric properties of a material layer using measured natural frequencies. *IEEE Transactions on Antennas and Propagation*, 58(2):620–623, 2010.

[3] Cuming Microwave Corporation. C-RAM MT-26 .125" x 24" x 24" PSA "Pressure Sensitive Adhesive.". `https://stores.cumingmicrowave-online-store.com/2-c-ram-mt-26-125-x-24-x-24-psa-pressure-sensitive-adhesive/`.

[4] W.B. Weir. Automatic measurement of complex dielectric constant and permeability at microwave frequencies. *Proceedings of the IEEE*, 62(1):33–36, 1974.

[5] A. M. Nicolson and G. F. Ross. Measurement of the intrinsic properties of materials by time-domain techniques. *IEEE Transactions on Instrumentation and Measurement*, 19(4):377–382, 1970.

CHAPTER 7

Conclusions and Further Work

7.1 Summary

The purpose of the work in this dissertation is to demonstrate the viability of a proposed aperture screen material characterization technique for the extraction of the constitutive parameters of conductor-backed materials. First, a theoretical formulation of the aperture screen problem is presented. Then, a theoretical demonstration is described with a numerical solution of the problem implemented and its robustness shown by considering the sensitivity of the technique to perturbations in the amplitude and phase values of an incident plane wave on an aperture screen adjacent to a conductor-backed material layer. The technique has been shown to exhibit performance that compares favorably against the two-thickness technique.

An experimental implementation in the MSU reflectivity arch range revealed alignment challenges that hindered immediate complete validation of the aperture screen theory through measurements. As such, only measurements of conductor-backed materials in the absence of the aperture screen are described. External measurements obtained from Dr Lydell Frasch made further experimentation possible. The results obtained and presented in this work reveal that the proposed technique shows great promise as an approach for the non-destructive characterization of the material properties of materials. However, further work is necessary to make the technique implementable in the field.

There are a few distinctions between the proposed theoretical model and a realizable experimental implementation that need to be explored in further detail. These include the consideration of a non-zero aperture screen thickness in the theoretical formulation. Also, non-uniformities in the thickness of the material layer being measured, which are not captured in the theoretical implementation, should be considered in more detail.

A drawback to the proposed method is that the aperture screen needs to be placed in direct contact with the MUT. This may not be desirable as it may lead to contamination of

the material. Also, it may be difficult to eliminate air gaps when contact is made with the MUT. In order to make the technique truly non-contact, an offset between the screen and material can be introduced, possibly in the form of cushioned stand-offs. This will require modification of the theoretical model to include the stand-off layer between the aperture screen and the MUT.

Ultimately, this work has has introduced a new free-space technique which can pave the way for the realization of truly non-destructive and non-contact characterization of conductor-backed lossy materials.

APPENDIX A: GREEN'S FUNCTION DERIVATION

The problem considered is shown Figure 7.1. The setup consists of an infinitesimally thick PEC layer with a thin aperture above a conductor-backed material region. The aperture has dimensions $-\frac{L}{2} < x < \frac{L}{2}$ and $-\frac{w}{2} < y < \frac{w}{2}$ with the material layer having dimensions for thickness $-t < z < 0$. The problem is solved by employing Hertzian potential Green's functions of which the details of their derivation are shown here.

Parallel Plate Configuration Green's function

The Hertzian potential wave equation given by

$$\nabla^2 \vec{\Pi}_m + k^2 \vec{\Pi}_m = -\frac{\vec{J}_m}{j\omega\mu} \tag{A.1}$$

can be solved so that the dyadic Green's function is identified. In turn, $\vec{E}$ and $\vec{H}$ can be computed using

$$\vec{E} = -j\omega\mu \nabla \times \vec{\Pi}_m \tag{A.2}$$

and

$$\vec{H} = k^2 \vec{\Pi}_m + \nabla \left(\nabla \cdot \vec{\Pi}_m \right). \tag{A.3}$$

Equation (A.1) can be solved by the method of superposition combining the homogeneous solution and a particular solution as

$$\vec{\Pi}_m = \vec{\Pi}_m^p + \vec{\Pi}_m^h \tag{A.4}$$

where $\vec{\Pi}_m^p$ and $\vec{\Pi}_m^h$ satisfy

$$\nabla^2 \vec{\Pi}_m^p + k^2 \vec{\Pi}_m^p = -\frac{\vec{J}_m}{j\omega\mu} \tag{A.5}$$

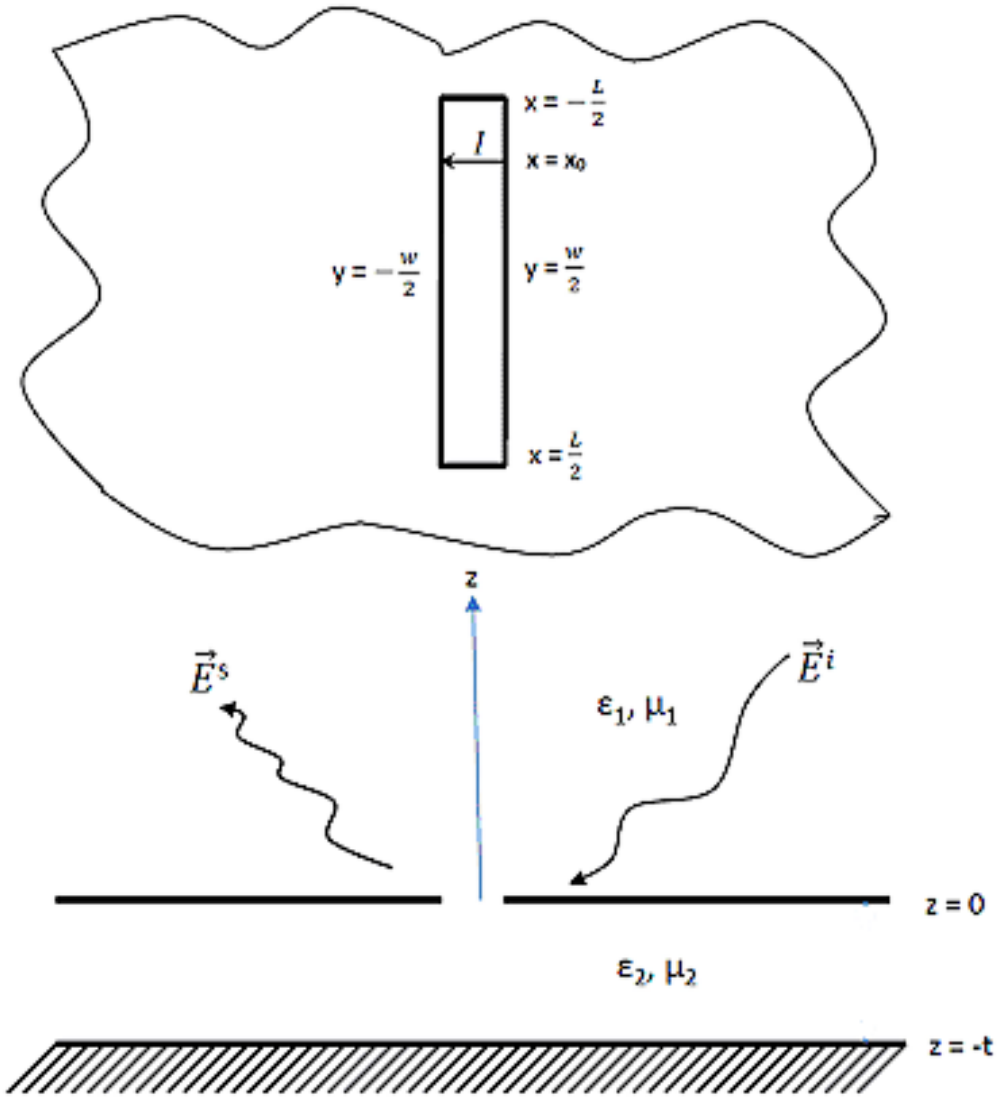

Figure A.1: Figure showing general problem geometry.

and

$$\nabla^2 \vec{\Pi}_m^h + k^2 \vec{\Pi}_m^h = 0 \tag{A.6}$$

respectively.

Dealing with (A.5) and (A.6) can be simplified by decomposing then into three separate scalar equations for each rectangular coordinate so that

$$\nabla^2 \Pi_{m_i}^p + k^2 \Pi_{m_i}^p = -\frac{J_{m_i}}{j\omega\mu}, \tag{A.7}$$

$$\nabla^2 \Pi_{m_i}^h + k^2 \Pi_{m_i}^h = 0 \tag{A.8}$$

where $i = x, y$ or z. Solutions to these equations can be found by using the Fourier transform method. Since the configuration is invariant along the x and y directions, a 2-dimensional Fourier transform is carried out using the Fourier transform pair

$$\tilde{f}(\vec{\lambda}, z) = \int_{-\infty}^{\infty} \int_{-\infty}^{\infty} f(\vec{r}) e^{-j\vec{\lambda}\cdot\vec{r}} dxdy \tag{A.9}$$

and

$$f(\vec{r}) = \frac{1}{(2\pi)^2} \int_{-\infty}^{\infty} \int_{-\infty}^{\infty} \tilde{f}(\vec{\lambda}, z) e^{j\vec{\lambda}\cdot\vec{r}} dk_x dk_y \tag{A.10}$$

where $\vec{r} = \hat{x}x + \hat{y}y + \hat{z}z$, and $\vec{\lambda} = \hat{x}k_x + \hat{y}k_y$. Taking advantage of the Fourier transform differentiation property, (A.7) and (A.8) become

$$\frac{\partial^2}{\partial z^2} \tilde{\Pi}_{m_i}^p \left(\vec{\lambda}, z\right) - p^2 \tilde{\Pi}_{m_i}^p \left(\vec{\lambda}, z\right) = -\frac{\tilde{J}_{m_i}\left(\vec{\lambda}, z\right)}{j\omega\mu} \tag{A.11}$$

and

$$\frac{\partial^2}{\partial z^2}\tilde{\Pi}^h_{m_i}\left(\vec{\lambda},z\right)-p^2\tilde{\Pi}^h_{m_i}\left(\vec{\lambda},z\right)=0 \tag{A.12}$$

where $p^2=\lambda^2-k^2$ and

$$\tilde{\Pi}^p_{m_i}(\vec{\lambda},z)=\int_{-\infty}^{\infty}\int_{-\infty}^{\infty}\Pi^p_{m_i}(\vec{r})e^{-j\vec{\lambda}\cdot\vec{r}}dxdy, \tag{A.13}$$

$$\tilde{\Pi}^h_{m_i}(\vec{\lambda},z)=\int_{-\infty}^{\infty}\int_{-\infty}^{\infty}\Pi^h_{m_i}(\vec{r})e^{-j\vec{\lambda}\cdot\vec{r}}dxdy \tag{A.14}$$

and

$$\tilde{J}_{m_i}(\vec{\lambda},z)=\int_{-\infty}^{\infty}\int_{-\infty}^{\infty}J^h_{m_i}(\vec{r})e^{-j\vec{\lambda}\cdot\vec{r}}dxdy. \tag{A.15}$$

Solutions to the second-order partial differential equations (A.11) and (A.12) are obtained in the next sections. In order to get a solution to (A.11) a Fourier transform is performed over z and using the Fourier tranform differentiation property as done earlier, $\tilde{\tilde{\Pi}}^p_{m_i}$ is found to be

$$\tilde{\tilde{\Pi}}^p_{m_i}\left(\vec{\lambda},k_z\right)=\frac{\tilde{\tilde{J}}_{m_i}(\vec{\lambda},k_z)}{j\omega\mu\left(k_z^2+p^2\right)}. \tag{A.16}$$

Using Cauchy's Integral Theorem, the inverse transform is taken and an expression for the Hertzian potential in the complex λ-plane is obtained as

$$\tilde{\Pi}^p_{m_i}\left(\vec{\lambda},z\right)=\int_{z'}\tilde{G}^p\left(\vec{\lambda};z|z'\right)\frac{\tilde{\tilde{J}}_{m_i}(\vec{\lambda},z)}{j\omega\mu}dz'. \tag{A.17}$$

The spectral domain Green's function in (A.17) is given by

$$\tilde{G}^p\left(\vec{\lambda}; z|z'\right) = \frac{e^{-p|z-z'|}}{2p} \tag{A.18}$$

where z and z' are the source and field points respectively and p is the spectral domain propagation factor.

The solution to (A.12) can expressed in the standard form

$$\tilde{\Pi}^h_{m_i}\left(\vec{\lambda}, z\right) = W_i^+\left(\vec{\lambda}\right)e^{-pz} + W_i^-\left(\vec{\lambda}\right)e^{pz} \tag{A.19}$$

where W_i^+ and W_i^- represent amplitude coefficients for upward traveling and downward traveling reflected waves respectively.

Putting (A.17) and (A.19) together, the complete spectral-domain Hertzian potential is

$$\tilde{\Pi}_{m_i}\left(\vec{\lambda}, z\right) = \int_{z'} \frac{e^{-p|z-z'|}}{2p}\frac{\tilde{\tilde{J}}_{m_i}(\vec{\lambda}, z)}{j\omega\mu}dz' + W_i^+\left(\vec{\lambda}\right)e^{-pz} + W_i^-\left(\vec{\lambda}\right)e^{pz}. \tag{A.20}$$

A more concise expression can be obtained by taking advantage of the fact that the distance in the exponential depends on the field location being less than or greater than the source location as given by the relationship

$$|z - z'| = \begin{cases} z - z', & z > z' \\ z' - z, & z < z'. \end{cases} \tag{A.21}$$

This makes it possible to rewrite (A.20) as

$$\Pi_{m_i} = \begin{cases} V_i^+e^{-pz} + W_i^+e^{-pz} + W_i^-e^{pz}, & z > z' \\ V_i^-e^{pz} + W_i^+e^{-pz} + W_i^-e^{pz}, & z < z' \end{cases} \tag{A.22}$$

where

$$V_i^{\pm}(\vec{\lambda}) = \int_{z'} \frac{e^{\pm pz'}}{2p} \frac{\tilde{J}_{m_i}\left(\vec{\lambda}, z'\right)}{j\omega\mu} dz' \tag{A.23}$$

correspond to upward and downward traveling waves launched by the source. The spectral coefficients are computed next.

Determination of the Spectral Coefficients

In order to determine the spectral coefficients W_i^+ and W_i^-, the boundary conditions at $z = 0$ and $z = -t$ are enforced on the spectral-domain Hertzian potential. E_x and E_y are expanded from (A.2) giving

$$E_x = -j\omega\mu \left[\frac{\partial \Pi_{m_z}}{\partial y} - \frac{\partial \Pi_{m_y}}{\partial z} \right] \tag{A.24}$$

and

$$E_y = -j\omega\mu \left[\frac{\partial \Pi_{m_x}}{\partial z} - \frac{\partial \Pi_{m_z}}{\partial x} \right]. \tag{A.25}$$

Since the tangential electric field vanishes on the surface of a PEC, the tangential boundary conditions on the spectral-domain Hertzian potential are found to be

$$\frac{\partial \Pi_{m_i}}{\partial z} = 0 \ \ ... \ \ i = x, y \tag{A.26}$$

and the normal boundary condition

$$\Pi_{m_z} = 0. \tag{A.27}$$

As will be shown in the sections that follow, implementation of these boundary conditions can be used to compute the spectral coefficients.

Tangential Boundary Conditions

Substituting (A.22) into (A.26), the tangential boundary condition at $z = 0$ can be applied leading to the expression

$$p\left(-V_i^+ - W_i^+ + W_i^-\right) = 0 \quad ... \quad i = x, y \tag{A.28}$$

which can be rearranged to give

$$W_i^- = V_i^+ + W_i^+ \quad ... \quad i = x, y. \tag{A.29}$$

Similarly enforcing the boundary condition at $z = -t$ by substituting (A.22) into (A.26), leads to the expression

$$p\left(V_i^- e^{-pt} - W_i^+ e^{pt} + W_i^- e^{-pt}\right) = 0 \quad ... \quad i = x, y \tag{A.30}$$

which can be rewritten in terms of W_i^+ as

$$W_i^+ = e^{-2pt}\left(V_i^- + W_i^-\right) \quad ... \quad i = x, y. \tag{A.31}$$

The expression for W_i^- can be found by substituting (A.31) into (A.29) and solving so that

$$W_i^- = \frac{V_i^- e^{-pt} + V_i^+ e^{pt}}{e^{pt} - e^{-pt}} \tag{A.32}$$

is obtained. Substituting (A.32) into (A.29) and solving for W_i^+ gives

$$W_i^+ = \frac{e^{-pt}(V_i^- + V_i^+)}{e^{pt} - e^{-pt}}. \tag{A.33}$$

Now that W_i^+ and W_i^- have been found they can be substituted into (A.20) with the resulting expression manipulated so that the tangential spectral-domain Hertz potential can

be obtained. A final form of

$$\tilde{\Pi}_{m_i}\left(\vec{\lambda},z\right)=\int_{z'}\tilde{G}^t\left(\vec{\lambda};z|z'\right)\frac{\tilde{J}_{m_i}\left(\vec{\lambda},z\right)}{j\omega\mu}dz' \tag{A.34}$$

is desired for the Hertz potential where $\tilde{G}^t$ is the tangential spectral-domain Green's function. This can be further expressed as a combination of a principal component and a scattered component thus

$$\tilde{G}^t\left(\vec{\lambda};z|z'\right)=\tilde{G}^{pt}\left(\vec{\lambda};z|z'\right)+\tilde{G}^{st}\left(\vec{\lambda};z|z'\right). \tag{A.35}$$

Substituting (A.32) and (A.33) into (A.20) gives

$$\begin{aligned}\tilde{\Pi}_{m_i}=\int_{z'}\frac{e^{-p|z-z'|}}{2p}\frac{\tilde{J}_{m_i}}{j\omega\mu}dz'+\frac{e^{-pt}\cdot e^{-pz}}{e^{pd}-e^{-pd}}\left[\int_{z'}\frac{e^{-pz'}}{2p}\frac{\tilde{J}_{m_i}}{j\omega\mu}dz'+\int_{z'}\frac{e^{pz'}}{2p}\frac{\tilde{J}_{m_i}}{j\omega\mu}dz'\right]\\+\frac{e^{pz}}{e^{pt}-e^{-pt}}\left[\int_{z'}\frac{e^{-pz'}}{2p}\frac{\tilde{J}_{m_i}}{j\omega\mu}dz'+\int_{z'}\frac{e^{pz'}}{2p}\frac{\tilde{J}_{m_i}}{j\omega\mu}dz'\right]\end{aligned} \tag{A.36}$$

from which $\tilde{G}^{pt}$ and $\tilde{G}^{st}$ are found to be

$$\tilde{G}^{pt}(\vec{\lambda};z|z')=\frac{e^{-p|z-z'|}}{2p} \tag{A.37}$$

and

$$\tilde{G}^{st}(\vec{\lambda};z|z')=\frac{e^{-p(z-z'+t)}+e^{-p(z+z'+t)}+e^{-p(-z+z'+t)}+e^{-p(-z-z'-t)}}{2p\left(e^{pt}-e^{-pt}\right)} \tag{A.38}$$

respectively.

Boundary Condition on the Normal Field

The normal boundary condition is enforced at $z = 0$ by substituting (A.22) into (A.27) and setting z to zero so that

$$W_z^- = -V_z^+ - W_z^+ \tag{A.39}$$

Substituting (A.22) in (A.27) and enforcing the boundary condition at $z = -t$ yeilds the expression

$$W_z^+ = -e^{-2pt}\left(V_z^- + W_z^-\right). \tag{A.40}$$

Following a procedure similar to that outlined in the previous section, W_z^+ and W_z^- are found to be

$$W_z^+ = \frac{e^{-pt}\left(-V_z^- + V_z^+\right)}{e^{pt} - e^{-pt}} \tag{A.41}$$

and

$$W_z^- = \frac{V_z^- e^{-pt} - V_z^+ e^{pt}}{e^{pt} - e^{-pt}} \tag{A.42}$$

The normal spectral-domain Hertz potential can be obtained by substituting (A.41) and (A.42) into (A.20) and comparing the resulting expression to the desired form

$$\tilde{\Pi}_{mz} = \int_{z'} \tilde{G}^n\left(\vec{\lambda}; z|z'\right) \frac{\tilde{J}_{mz}\left(\vec{\lambda}, z\right)}{j\omega\mu} dz'. \tag{A.43}$$

Again, following the same steps as in the previous section $\tilde{G}^n$ is obtained as

$$\tilde{G}^n\left(\vec{\lambda}, z|z'\right) = \tilde{G}^{pn}\left(\vec{\lambda}, z|z'\right) + \tilde{G}^{sn}\left(\vec{\lambda}, z|z'\right) \tag{A.44}$$

where

$$\tilde{G}^{pn}(\vec{\lambda}; z|z') = \frac{e^{-p|z-z'|}}{2p} \tag{A.45}$$

and

$$\tilde{G}^{sn}(\vec{\lambda}; z|z') = \frac{e^{-p(z-z'+t)} - e^{-p(z+z'+t)} + e^{-p(-z+z'+t)} - e^{-p(-z-z'-t)}}{2p\left(e^{pt} - e^{-pt}\right)}. \tag{A.46}$$

Dyadic Green's function

The spectral-domain Green's functions expressed in (A.35) and (A.44) can be manipulated to produce versions that are practical and that are employed in the MFIEs used in this work. Collecting terms in (A.37), (A.38), (A.45) and (A.46) and using the definitions of the hyperbolic functions the spectral domain Green's functions can be written as

$$\tilde{G}^{t}\left(\vec{\lambda}, z|z'\right) = \frac{\cosh p\left(t - |z-z'|\right) + \cosh p\left(t + z + z'\right)}{2p\sinh(pt)} \tag{A.47}$$

$$\tilde{G}^{n}\left(\vec{\lambda}, z|z'\right) = \frac{\cosh p\left(t - |z-z'|\right) - \cosh p\left(t + z + z'\right)}{2p\sinh(pt)}. \tag{A.48}$$

Considering only the tangential spectral-domain Green's function, for $z = z' = 0$, (A.47) becomes

$$\tilde{G}^{t}\left(\vec{\lambda}, z|z'\right) = \frac{2\cosh(pt)}{2p\sinh(pt)} \tag{A.49}$$

which can be rewritten as

$$\tilde{G}^{t}\left(\vec{\lambda}, z|z'\right) = \frac{\sinh(pt) + e^{-pt}}{p\sinh(pt)}. \tag{A.50}$$

Simplifying (A.50) yeilds

$$\tilde{G}^t\left(\vec{\lambda}, z|z'\right) = \frac{1}{p}\left[1 + \frac{e^{-pt}}{\sinh(pt)}\right] \tag{A.51}$$

Finally, the space-domain Green's function employed is obtained by taking an inverse Fourier transform as follows

$$\tilde{G}^t\left(\vec{r}|\vec{r}\,'\right) = \frac{1}{(2\pi)^2}\int_{-\infty}^{\infty}\int_{-\infty}^{\infty}\tilde{G}^t\left(\vec{\lambda}; z|z'\right)e^{j\lambda\cdot(\vec{r}-\vec{r}\,')}d\xi d\eta \tag{A.52}$$

APPENDIX B: STANDARD ERROR PROPAGATION METHOD

Let $S_1 = Ae^{j\phi 1}$ and $S_2 = Ae^{j\phi 2}$ represent measured quantities where $S = S_{11}$ or $S = S_{21}$ as is appropriate depending on the S-parameter being measured. It is desired that $\epsilon(S_1, S_2) = \epsilon_r'(S_1, S_2) + j\epsilon_r''(S_1, S_2)$ and $\mu(S_1, S_2) = \mu_r'(S_1, S_2) + j\mu_r''(S_1, S_2)$ be extracted. The propagated error can be computed using the standard formulas

$$\sigma_{\epsilon_r'} = \sqrt{\sigma_{A_1}^2 \left(\frac{\partial \epsilon_r'}{\partial A_1}\right)^2 + \sigma_{\phi_1}^2 \left(\frac{\partial \epsilon_r'}{\partial \phi_1}\right)^2 + \sigma_{A_2}^2 \left(\frac{\partial \epsilon_r'}{\partial A_2}\right)^2 + \sigma_{\phi_2}^2 \left(\frac{\partial \epsilon_r'}{\partial \phi_2}\right)^2} \tag{B.1}$$

and

$$\sigma_{\epsilon_r''} = \sqrt{\sigma_{A_1}^2 \left(\frac{\partial \epsilon_r''}{\partial A_1}\right)^2 + \sigma_{\phi_1}^2 \left(\frac{\partial \epsilon_r''}{\partial \phi_1}\right)^2 + \sigma_{A_2}^2 \left(\frac{\partial \epsilon_r''}{\partial A_2}\right)^2 + \sigma_{\phi_2}^2 \left(\frac{\partial \epsilon_r''}{\partial \phi_2}\right)^2} \tag{B.2}$$

for the real and imaginary parts of the constitutive parameters respectively. Similar expressions can be written out for μ. It should be noted that the following partial derivatives are called the "amplification factors": $\frac{\partial \epsilon_r'}{\partial A}$, $\frac{\partial \epsilon_r'}{\partial A}$, $\frac{\partial \epsilon_r'}{\partial A}$, $\frac{\partial \epsilon_r'}{\partial A}$.

If ϵ_r is differentiable then there are relationships between the amplification factors implied by the Cauchy-Riemann equations. These relationships are

$$\frac{\partial \epsilon_r'}{\partial A} = \frac{1}{A}\frac{\partial \epsilon_r''}{\partial \phi}, \tag{B.3}$$

$$\frac{1}{A}\frac{\partial \epsilon_r'}{\partial \phi} = -\frac{\partial \epsilon_r''}{\partial A}, \tag{B.4}$$

$$\frac{\partial \epsilon_r''}{\partial \phi} = A\frac{\partial \epsilon_r'}{\partial A}, \tag{B.5}$$

and

$$\frac{\partial \epsilon_r''}{\partial A} = -\frac{1}{A}\frac{\partial \epsilon_r'}{\partial \phi} \tag{B.6}$$

Computing the derivative of ϵ with respect to A gives

$$\frac{\partial \epsilon}{\partial A} = \frac{\partial \epsilon_r'}{\partial A} + j\frac{\partial \epsilon_r''}{\partial A}. \tag{B.7}$$

Considering (B.7), the real and imaginary parts can be split into

$$\mathrm{Re}\left\{\frac{\partial \epsilon}{\partial A}\right\} = \frac{\partial \epsilon_r'}{\partial A} \tag{B.8}$$

and

$$\mathrm{Im}\left\{\frac{\partial \epsilon}{\partial A}\right\} = \frac{\partial \epsilon_r''}{\partial A}, \tag{B.9}$$

respectively.

The expressions in (B.4) and (B.5) can be substituted into (B.1) and (B.2) to give

$$\phi_{\epsilon_r'} = \sqrt{\sigma_{A_1}^2\left(\frac{\partial \epsilon_r'}{\partial A_1}\right)^2 + \sigma_{\phi_1}^2\left(A_1\frac{\partial \epsilon_r''}{\partial A_1}\right)^2 + \sigma_{A_2}^2\left(\frac{\partial \epsilon_r'}{\partial A_2}\right)^2 + \sigma_{\phi_2}^2\left(A_2\frac{\partial \epsilon_r''}{\partial A_2}\right)^2} \tag{B.10}$$

and

$$\phi_{\epsilon_r''} = \sqrt{\sigma_{A_1}^2\left(\frac{\partial \epsilon_r''}{\partial A_1}\right)^2 + \sigma_{\phi_1}^2\left(A_1\frac{\partial \epsilon_r'}{\partial A_1}\right)^2 + \sigma_{A_2}^2\left(\frac{\partial \epsilon_r''}{\partial A_2}\right)^2 + \sigma_{\phi_2}^2\left(A_2\frac{\partial \epsilon_r'}{\partial A_2}\right)^2} \tag{B.11}$$

Similar expressions can be obtained for μ

It should be noted that A_1 and A_2 from (B.10) and (B.11) are expressed in terms of linear amplitudes. If A_1 and A_2 are given in decibels then the chain rule can be applied so

that

$$\frac{\partial \epsilon_r'}{\partial A_{dB}} = \frac{\partial \epsilon_r'}{\partial A} \frac{\partial A}{\partial A_{dB}}. \tag{B.12}$$

Here,

$$A_{dB} = 20 \log_{10} A \tag{B.13}$$

which can be rearranged to give

$$A = e^{A_{dB} \frac{\ln 10}{20}}. \tag{B.14}$$

Taking the derivative of (B.14) with respect to A_{dB} leads to

$$\frac{\partial A}{\partial A_{dB}} = \frac{\ln 10}{20} e^{A_{dB} \frac{\ln 10}{20}} \tag{B.15}$$

which is simply

$$\frac{\partial A}{\partial A_{dB}} = \frac{A \ln 10}{20}. \tag{B.16}$$

Therefore, (B.12) can be rewritten as

$$\frac{\partial \epsilon_r'}{\partial A_{dB}} = \frac{\partial \epsilon_r'}{\partial A} \left(\frac{ln10}{20} A \right). \tag{B.17}$$

And similarly for ϵ'',

$$\frac{\partial \epsilon_r''}{\partial A_{dB}} = \frac{\partial \epsilon_r''}{\partial A} \left(\frac{ln10}{20} A \right). \tag{B.18}$$

The expressions in (B.17) and (B.18) can be substituted in (B.10) and (B.11) so that the

propagated error terms become

$$\sigma_{\epsilon_r'} = \sqrt{\begin{bmatrix} \sigma^2_{A_{dB_1}} \left(\frac{\partial \epsilon_r'}{\partial A_1}\right)^2 \left(\frac{\ln 10}{20} A_1\right)^2 + \sigma^2_{\phi_1} \left(\frac{\partial \epsilon_r''}{\partial A_1}\right)^2 (A_1)^2 \\ + \sigma^2_{A_{dB_2}} \left(\frac{\partial \epsilon_r'}{\partial A_2}\right)^2 \left(\frac{\ln 10}{20} A_2\right)^2 + \sigma^2_{\phi_2} \left(\frac{\partial \epsilon_r''}{\partial A_2}\right)^2 (A_2)^2 \end{bmatrix}} \tag{B.19}$$

and

$$\sigma_{\epsilon_r''} = \sqrt{\begin{bmatrix} \sigma^2_{A_{dB_1}} \left(\frac{\partial \epsilon_r''}{\partial A_1}\right)^2 \left(\frac{\ln 10}{20} A_1\right)^2 + \sigma^2_{\phi_1} \left(\frac{\partial \epsilon_r'}{\partial A_1}\right)^2 (A_1)^2 \\ + \sigma^2_{A_{dB_2}} \left(\frac{\partial \epsilon_r''}{\partial A_2}\right)^2 \left(\frac{\ln 10}{20} A_2\right)^2 + \sigma^2_{\phi_2} \left(\frac{\partial \epsilon_r'}{\partial A_2}\right)^2 (A_2)^2 \end{bmatrix}}. \tag{B.20}$$

Expressing the error terms in the fashion shown in (B.19) and (B.20) provides the advantage that only four complex derivatives are needed for the computing the error $\left(\frac{\partial \epsilon}{\partial A_1}, \frac{\partial \epsilon}{\partial A_2}, \frac{\partial \mu}{\partial A_1}, \frac{\partial \mu}{\partial A_2}\right)$. Again, similar error expressions can be obtained for the permeability.